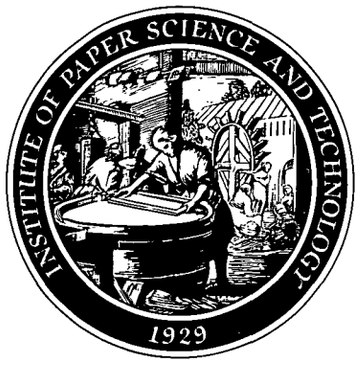

Institute of Paper Science and Technology

STATUS REPORTS

To The

PAPERMAKING

And

PROCESS SIMULATION AND CONTROL

PROJECT ADVISORY COMMITTEE

March 22, 1994

IPST

Atlanta, Georgia

INSTITUTE OF PAPER SCIENCE AND TECHNOLOGY
PURPOSE AND MISSION STATEMENT

The Institute of Paper Science and Technology is a unique organization whose charitable, educational, and scientific purpose evolves from the singular relationship between the Institute and the pulp and paper industry which has existed since 1929. The purpose of the Institute is fulfilled through three missions, which are:

- to provide high quality students with a multidisciplinary graduate educational experience which is of the highest standard of excellence recognized by the national academic community and which enables them to perform to their maximum potential in a society with a technological base; and
- to sustain an international position of leadership in dynamic scientific research which is participated in by both students and faculty and which is focused on areas of significance to the pulp and paper industry; and
- to contribute to the economic and technical well-being of the nation through innovative educational, informational, and technical services.

ACCREDITATION

The Institute of Paper Science and Technology is accredited by the Commission on Colleges of the Southern Association of Colleges and Schools to award the Master of Science and Doctor of Philosophy degrees.

NOTICE AND DISCLAIMER

The Institute of Paper Science and Technology (IPST) has provided a high standard of professional service and has put forth its best efforts within the time and funds available for this project. The information and conclusions are advisory and are intended only for internal use by any company who may receive this report. Each company must decide for itself the best approach to solving any problems it may have and how, or whether, this reported information should be considered in its approach.

IPST does not recommend particular products, procedures, materials, or service. These are included only in the interest of completeness within a laboratory context and budgetary constraint. Actual products, procedures, materials, and services used may differ and are peculiar to the operations of each company.

In no event shall IPST or its employees and agents have any obligation or liability for damages including, but not limited to, consequential damages arising out of or in connection with any company's use of or inability to use the reported information. IPST provides no warranty or guaranty of results.

INSTITUTE OF PAPER SCIENCE AND TECHNOLOGY

Atlanta, Georgia

ANNUAL RESEARCH REVIEW

PAPERMAKING
And
PROCESS SIMULATION AND CONTROL

March 22, 1994

February 16, 1994

TO: MEMBERS OF THE PAPERMAKING PROJECT ADVISORY COMMITTEE AND PROCESS SIMULATION AND CONTROL PROJECT ADVISORY COMMITTEE

Attached for your review are the Status Reports for the projects to be discussed at the Papermaking and the Process Simulation and Control Project Advisory Committee meeting. The program review is scheduled for Tuesday, March 22, 1994 at 8:00 a.m. to 12:30 p.m. The Papermaking PAC and the Process Simulation and Control PAC committee meetings will meet separately during the afternoon of Tuesday, March 22 from 1:30 p.m. to 5:00 p.m.

We look forward to seeing you. Best regards

Sincerely,

David I. Orloff, Ph.D.
Professor of Engineering & Director
Engineering and Paper Material Division

DIO/map

Attachments

Institute of Paper Science and Technology, Inc.

500 10th Street, N.W.
Atlanta, GA 30318-5794

Formerly The Institute of Paper Chemistry
Appleton, Wisconsin

Telephone 404-853-9500
FAX # 404-853-9510

PAPERMAKING
PROJECT ADVISORY COMMITTEE

IPST Liaison: David Orloff (404) 853-1872, FAX (404) 853-9510

Mr. David A. Blythe ***(1996)**
Technical Director
Appleton Papers, Inc.
P.O. Box 359
Appleton, WI 54912-0359

Mr. Jack F. Brown ***(1994)**
Manager, Paper and Coatings
Boise Cascade Corporation
Pulp and Paper Research
4435 North Channel Avenue
Portland, OR 97217-7652
(503) 286-7418
(503) 286-7467 FAX

Mr. Frank Cunnane ***(1996)**
Vice President - Marketing
Asten Press Fabrics, Inc.
P.O. Box 518
Clinton, SC 29325-0518
(803) 833-3800
(803) 833-6657 FAX

Mr. George Iverson ***(1996)**
Supervisor, Papermaking Technology
Eastman Kodak Company
Polymer Processing Division
1669 Lake Avenue
Rochester, NY 14652-3622
(716) 588-3870
(716) 588-2680 FAX

Mr. Jeffrey M. Jensen ***(1996)**
Paper Mill Superintendent
Westvaco Corporation
Bleached Board Division
104 East Riverside Street
Covington, VA 24426

Dr. Sam Lin ***(1996)**
Principal Engineer
Packaging Corporation of America
5401 Old Orchard Road
Skokie, IL 60077-1038
(708) 470-3350
(708) 470-3390 FAX

Mr. Joeseph P. MacDowell ***(1996)**
Research Project Supervisor
Coated and Uncoated
P. H. Glatfelter Company
228 S. Main Street
Spring Grove, PA 17362-1000
(717) 225-4711
(717) 225-6834 FAX

Mr. Richard Reese ***(1996)**
Sr. Paper Machine Engineer
Georgia-Pacific Corporation
P. O. Box 105605
133 Peachtree St., NE
Atlanta, GA 30348
(404) 521-4000
(404) 521-5093 FAX

Mr. Allen Rosen ***(1995)**
Section Leader Processes
Union Camp Corporation
Research and Development Division
P. O. Box 3301
Princeton, NJ 08543-3301
(609) 896-1200
(609) 844-7323 FAX

Dr. Jay A. Shands ***(1997)**
Manager, Forming Systems
Beloit Corporation
Rockton Research Center
1165 Prairie Hill Road
Rockton, IL 61072-1595
(608) 364-8501
(608) 364-8600

* The dates in ( ) indicate the final year of the appointment.

Papermaking (cont.)

Dr. Roger A. Somsen ***(1996)**
Director, Research and Development
Riverwood International
P. O. Box 35800
West Monroe, LA 71294-5800
(318) 362-2000
(318) 362-2133 FAX

Dr. Michael S. Steltenkamp ***(1996)**
Department Leader
Champion International Corporation
West Nyack Rd.
West Nyack, NY 10994-7228
(914) 578-7228
(914) 578-7175 FAX

Mr. James F. Stewart ***(1996)**
Division VP Mill Operations
Stone Container Corporation
1979 Lakeside Parkway
Suite 300
Tucker, GA 30084
(404) 621-6700
(404) 621-6747 FAX

Mr. Benjamin A. Thorp (Chairman)
***(1994)**
Senior Vice President
James River Corporation
P. O. Box 2218
Richmond, VA 23217-2218
(804) 649-4335
(804) 649-4369 FAX

Mr. James C. West ***(1995)**
Containerboard Manufacturing Manager
Weyerhaeuser Paper Company
5410 79th Avenue Court
Tacoma, WA 98467-3970
(206) 924-2345
(206) 924-2303 FAX

Mr. Lloyd O. Westling ***(1996)**
Superintendent
Longview Fibre Company
Post Office Box 639
Longview, WA 98632
(206) 425-1550
(206) 425-9877 FAX

* The dates in ( ) indicate the final year of the appointment.

PROCESS SIMULATION AND CONTROL
PROJECT ADVISORY COMMITTEE

IPST Liaison: Dave Orloff (404) 853-1872, FAX (404) 853-9510

Dr. G. R. (Ron) Brown (Chairman)
***(1995)**
Director of Laurel Research Laboratory
Westvaco Corporation
11101 Johns Hopkins Road
Laurel, MD 20723-6006
(301)497-1301
(301)497-1309 FAX

Mr. Karel K. Cerny ***(1995)**
Senior Control Systems Engineer
Georgia-Pacific Corporation
P.O. Box 105605
133 Peachtree Street, NE
Atlanta, GA 30348-5605
(404)521-4603
(404)521-5093 FAX

Mr. Jack M. Kleinfeld ***(1996)**
Senior Scientist
Champion International Corporation
West Nyack Road
West Nyack, NY 10994-0608
(914)578-7292
(914)578-7175 FAX

Dr. Sanford G. Levy (Vice Chairman)
***(1996)**
R&D Group Leader -
Process Control Applications
Union Camp Corporation
3401 Princeton Pike
Lawrenceville, NJ 08648
(609) 844-7361
(609) 844-7366 FAX

Mr. Robert E. McIntyre ***(1996)**
Technical Resource Coordinator
Asten Group, Inc.
209 Brereton Drive
Raleigh, NC 27615
(919) 847-0506

Mr. Willard M. Reed, Jr. ***(1995)**
Process Analysis Supervisor
MacMillan Bloedel, Inc.
P. O. Box 336
Pine Hill, AL 36769-0336
(205)963-4391
(205)963-4513 FAX

Mr. Glen C. Smith ***(1995)**
Technical Manager
Mead Corporation
Central Research Labs
8th and Hickory Streets
Chillicothe, OH 45601
(614)772-3513
(614)772-3595 FAX

Mr. John Swafford ***(1996)**
Packaging Corporation of America
5401 Old Orchard Road
Skokie, IL 60077-1073
(708) 470-2312
(708) 470-3390 FAX

* The dates in ( ) indicate the final year of the appointment.

PAPERMAKING/PROCESS SIMULATION AND CONTROL PROJECT ADVISORY COMMITTEE MEETING

March 22, 1993
Institute of Paper Science and Technology
Atlanta, Georgia

AGENDA

Papermaking/Process Simulation and Control Program Review (APR)

8:00 a.m. - 8:15 a.m.	Opening Remarks and Anti Trust Statement	Ben Thorp
8:15 a.m. - 9:00 a.m.	Project 3470/3595 Advances in Impulse Drying Research	David Orloff
9:00 a.m. - 9:45 a.m.	Project 3674 Advances in High Speed Coating Systems	Cyrus Aidun
9:45 a.m. - 10:15 a.m.	Project 3730 Dynamics of Air-Sheet Interactions in Web Transport	Cyrus Aidun P. Neitzel (GT)
10:15 a.m. - 10:30 a.m.	Break	
10:30 a.m. - 11:45 a.m.	Project 3480 Improving Press Performance	Jeff Lindsay
11:45 a.m. - 12:30 p.m.	Project 3470/3595 Controlled Crown Press Lubrication and Heat Transfer	Barry Hojjatie Fred Bloom (NIU)
12:30 p.m. - 1:30 p.m.	Lunch	
1:30 p.m. - 5:00 p.m.	Papermaking Committee Discussions	David Orloff

TABLE OF CONTENTS

AIR/SHEET INTERACTIONS

STATUS REPORT

FOR

PROJECT 3730

March 22, 1994

Institute of Paper Science and Technology
Atlanta, Georgia

Technical Program Review Report

Date: January 1994
Project Title: Air/Sheet Interactions
Project Leader: Cyrus K. Aidun
Budget (FY 93-94): $155,000
Reporting Period: Spring '93 to Winter '94
Project No.: 3730

PROGRAM OBJECTIVES:

The objectives of this project are: a) better understanding of the fluid dynamics and the structural mechanics of sheet flutter; b) correlating the onset of break or sheet damage ("pain threshold") with the sheet flutter characteristics (e.g., frequency, speed, ...) and the sheet's structural properties; and c) extension of the results to analysis of blade deformation and vibration in coating processes.

The interactions between fluid flow and flexible solid boundaries will be examined with applications to processes in paper manufacturing. The primary application is in sheet vibration induced by interactions between the sheet and the adjacent air stream which results in operational difficulties and web breaks.

SUMMARY OF PROGRESS FOR THE PAST PERIOD:

This is the second year of this project and many of the initial tasks involving development of the techniques required for computational and experimental studies of the air/sheet interactions have been completed.

We are developing a computational program to evaluate the three-dimensional surface deformation of the substrate under load and transform of coordinates from global to the local surface deformation system. The initial computational experiments demonstrated the potential of this approach in terms of air/sheet interactions, as well as, optimization of moisture removal from the dryer section. Based on the initial two-dimensional low-speed computations, the PAC members (Ben Thorp, Chairman) suggested that we file an invention disclosure form for a more effective ventilation in the dryer section. The Invention Disclosure is attached to this report.

The two-dimensional program for the solution of the full equations governing the fluid flow with rigid boundaries have been completed. Several sample problems have been solved to confirm the correctness and accuracy of the formulation and the solution methodology. The complete formulation for this part of the program is outlined below.

In the last report, we outlined the results from a series of wind tunnel experiments to evaluate the system for an in-depth study of sheet fluttering and mechanisms of reducing the vibration and consequent sheet breaks. Problems with these experiments were identified and resolved. The samples used in the wind-tunnel experiments were Bond #4 printing paper, Letter Print (IPST Letterhead) paper, unbleached paperboard (Corrugating Medium), and light-weighted "trace" paper. Once the computational methods are fully developed, the experimental data can be used to evaluate the solution.

BACKGROUND

The fluttering of a moving web is often analyzed by using the "threadline" model, one that assumes the entire width of the web deflects together, and neglects cross-directional variation of web motion. This model was studied by Pramila [1], who combined separate theories of the dynamics of axially moving material and hydrodynamics to include aerodynamic terms in the model. By simply adding the mass of surrounding air to the mass of the web, an "added mass" model was obtained. Pramila also assumed that the web is in an infinite air space and all the surrounding air move at the same speed as the web. In later studies, it has been demonstrated that the interaction between web and surrounding air is an important contributor to web instability and should therefore be taken into account.

In a later article, Pramila [2] assumes the air to be stationary, moving only in planes perpendicular to the x-axis. This consideration was taken into account by summing the added mass to the first term of the equation of motion only, rather than to all inertia terms, as was done in Pramila [1]. Although analytical results showed that the rate of decrease of natural frequency fare slightly better on this assumption, no definite conclusion could be drawn.

The "threadline model" was used again by Chang and Moretti [3] to study the out-of-plane flutter of a moving web. They showed that each of the dynamic terms in the governing equation - namely the transverse acceleration, Coriolis, and centrifugal forces - are affected differently by the

air, depending on the air flow and the surrounding enclosure. They also determined the influence of parallel air flow and detected two different instabilities - steady deflection and flutter.

In the article by Race and company [4], an investigation into the air movement induced by felts and fabrics was undertaken. The object was to determine the cause of sheet flutters experienced in first dryer sections of newsprint- making machines, with special attention placed on the surface roughness and permeability of the felt or fabric. The study also tested the claim that, by using felts and fabrics of high permeability of the dryer sections of paper machines, an induced ventilation effect will be obtained, resulting in an increase of the drying rate. What the study found was that the volume of air "pumped" through a fabric is depended only on the fabric permeability itself and not on the surface roughness as was presupposed. It also found that the ventilating effect resulting from the use of a fabric is governed not only by the felt permeability but by the machine speed, too. These findings helped paper makers to eliminate the possibility of surface roughness as a contributor to the problems of sheet flutter and provide them with a better idea of where to use felt or fabric at different parts of the paper making machine.

In studying the physics of paper machine sheet flutter, Soininen [5] suggested that air flows do not generally create the edge flutter as often assumed, but instead, the edge flutter produces such air flows that the transversal wave energy component is dissipated to the air. He, then, concluded that the main reason for sheet flutter is a variation of basis weight of the sheet.

The idea of visualizing air flows by colored smoke documented by Sieverding [6] was also used in these preliminary experiment with a limited degree of success.

PHYSICALLY BASED COMPUTATIONAL ANALYSIS

Shin-Jye Liang, G. Paul Neitzel, Cyrus K. Aidun

Computational analysis based upon physical principles represents a promising technique in investigation of many paper making processes. The dynamics of a deformable object in response to some applying force can be analyzed by including the relevant physical properties of the solid and the liquid phases. The deformable model is governed by the mechanical laws of continuous bodies whose shapes can change over time. These principles, expresses in the form of dynamic differential equations, unify the description of shape and motion. By solving the equations numerically, a realistic analysis of the problem

involving the interaction of the deformable object with the surrounding fluid becomes possible. By varying input parameters, the dependency of the systems behavior on physical parameters or boundary conditions may be examined. The two cases that we shall consider are the elastohydrodynamics of blade coating and the air/sheet interactions in this project. The basic principles and approach in analyzing both cases are the virtually the same.

In this project, however, we focus on air/sheet interactions. This problem consists of a deformable sheet under tension and exposed to varying air interactions. These variations include the sheet velocity and the air/sheet *angle of attack*. Taking the many possible complex configurations of wave patterns forming by the sheet, the case under investigation poses a very complex continuum mechanics problem. Therefore, it is appropriate to start with a rather simplified version of the problem and gradually introduce physical complications until the full complex and realistic system is considered. The overall approach can be summarized in the form of a block diagram presented below.

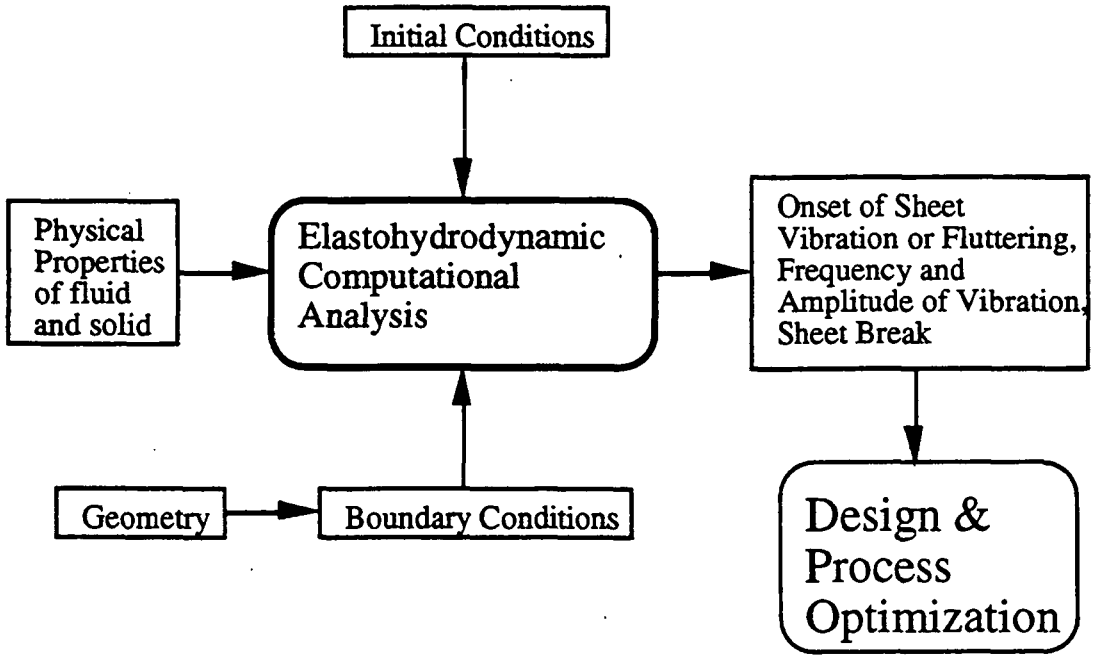

Figure 5. Block diagram of the computational approach.

The mathematical formulation for the coordinate deformation and mapping of the boundary to a local coordinate was presented in the last report. In this report, we outline the

computational method for the more challenging part of the project, that is the fluid flow and interactions with the boundary.

The mathematical formulation and the solution procedure for the air flow with a rigid boundary are outlined below. The computational procedure, as outlined here, are formulated and implemented in general terms. Therefore, this method can be applied to any section of the paper machine. Tensor notation is used for designation of the spatial coordinates. Accordingly, repeated indices imply summation over the three spatial directions. An index following a comma indicates partial derivative of the variable with respect to the corresponding spatial coordinates. The variables are defined in the text following each equation.

The Navier-Stokes equations which describe the flow of a steady, viscous, incompressible Newtonian fluid with constant properties, written in terms of primitive variables are

$$\rho u_\beta u_{\alpha,\beta} = \tau_{\alpha\beta,\beta} \tag{1}$$

and

$$u_{\beta,\beta} = 0 \tag{2}$$

where

$$\tau_{\alpha,\beta} = -p\delta_{\alpha\beta} + \mu(u_{\alpha,\beta} + u_{\beta,\alpha}) \tag{3}$$

x_α is the position in Cartesian coordinates, u_α is the velocity component in α-direction, p is the pressure derivation from hydrostatic, ρ is the fluid density, μ is the fluid viscosity, and $\delta_{\alpha\beta}$ is the Kronecker delta.

On each segment of the boundary, $\partial\Omega$, of the computational domain, Ω, it is necessary to prescribe appropriate boundary conditions. A precise statement of mathematically legitimate boundary conditions (in the sense of well posedness) for the Navier-Stokes equations often does not exist. A couple examples are open, or outflow, boundary conditions and free/moving boundary conditions (Gresho 1992; Christoudoulou and Scriven 1989; Sackinger et al. 1989; Kistler and Scriven 1984). Hence, there is understandable ambiguity, and even confusion, when boundary conditions are selected for numerical simulations. The boundary conditions relating to the momentum equations commonly employed are either the specification of the velocity components

$$u_\alpha = \bar{u}_\alpha(s) \tag{4}$$

or specification of the surface stresses

$$n_\beta \tau_{\alpha\beta} = \tilde{\tau}_\alpha \tag{5}$$

where s is a parameter measuring position along the relevant boundary segment, and $\underline{n}(s)$ is the outward normal to the boundary.

Finite-Element Formulation

Only for limited cases do analytic solutions of the Navier-Stokes equations exist. For most problems of engineering interest, the Navier-Stokes equations are solved numerically. Difficulties in obtaining the numerical solution are related to the following: (1) the irregular geometries of the considered domain; (2) the equations are strongly coupled; (3) the equations are inherently nonlinear in the convection terms; (4) for convection-dominated flows, i.e. Re >> O(1), if the employed grid resolution is not fine enough, non-physical oscillations are prone to occur (Gresho and Lee 1981); (5) the continuity equation which regulates the pressure solution does not explicitly include the pressure variable (Sani et al. 1981a, b; Patankar 1980).

There are other versions of the Navier-Stokes equations derived from the "primitive" equations, such as the pressure Poisson equation and vorticity transport equation. Gresho (1991) has shown that the use of a primitive-variable form has some distinct advantages. In the following, the formal derivation of the Galerkin equations of the Navier-Stokes equations based on the primitive variables is presented (Gunzburg 1989; Curvelier 1986; Thomasset 1981).

Weak Form

The finite-element spatial discretization is performed using the Galerkin method. Within each element, the velocity and pressure fields are approximated by piecewise polynomial basis sets

$$u_\alpha^h(x_\beta) = \phi^T(x_\beta) U_\alpha \tag{6}$$

$$p^h(x_\beta) = \varphi^T(x_\beta) P \tag{7}$$

where U_α and P are column vectors of element nodal point, $\phi(x_\beta)$ and $\varphi(x_\beta)$ are column vectors of the interpolation functions, and the superscript T represents the transpose. Herein the same basis functions are employed for all components of the velocity. Substitution of these approximations into the governing equations and the boundary conditions yields a set of equations:

$$\text{Momentum: } f_1(\phi,\varphi,U_i,P) = R_1 \tag{8}$$

$$\text{Continuity: } f_2(\varphi,U_i) = R_2 \tag{9}$$

where R_1 and R_2 are the residuals (errors) resulting from the use of the approximations (6) and (7).

The Galerkin form of the Method of Weighted Residuals seeks to reduce these errors to zero, in a weighted sense, by making the residuals orthogonal to the test functions of each element (i.e., ϕ *and* φ). These orthogonality conditions are expressed by

$$\text{Momentum: } (f_1,\phi) = (R_1,\phi) = 0 \tag{10}$$

$$\text{Continuity: } (f_2,\varphi) = (R_2,\varphi) = 0 \tag{11}$$

where (a,b) denotes the inner product, defined as

$$(a,b) = \int_\Omega a \cdot b \, d\Omega \tag{12}$$

A detailed derivation of the weak form of the Navier-Stokes equations, (1) - (3), and associated boundary conditions, (4) and (5), is given in Appendix A. The final forms are

$$\left(U_\beta^k \int_\Omega \rho\phi_i\phi_k\phi_{j,\beta}\right)U_\alpha^j + \left(\int_\Omega \mu\phi_{i,\beta}\phi_{j,\beta}\right)U_\alpha^j - \left(\int_\Omega \phi_{i,\alpha}\varphi_j\right)P_j = \int_{\partial\Omega} \phi_i \bar{\tau}_\alpha \; ; \; i = 1, 2, ..., L \tag{13}$$

$$\left(\int_\Omega \varphi_j\phi_{i,\alpha}\right)U_\alpha^i = \underline{0} \; ; \quad j = 1, 2, ..., M \tag{14}$$

where L and M are the number of velocity and pressure nodes, respectively, in the discrete domain.

Matrix Form

The component equations (13) and (14) can be combined into a single matrix equation

$$\text{Momentum}: \quad \left[\underline{\underline{N}}(\underline{U}) + \underline{\underline{K}}\right]\underline{U} + \underline{\underline{C}}\,\underline{P} = \underline{f} \tag{15}$$

and

$$\text{Continuity}: \quad \underline{\underline{C}}^T\,\underline{U} = \underline{0} \tag{16}$$

or in a more general format as

$$\underline{\underline{A}}(\underline{w})\,\underline{w} = \underline{b}(\underline{w}) \tag{17}$$

where

$$\underline{w}^T = \left\{\underline{U}^T, \underline{P}^T\right\} \tag{18}$$

The definitions of the matrices $\underline{\underline{N}}(\underline{U})$, $\underline{\underline{K}}$, $\underline{\underline{C}}$, and $\underline{f}$ are given in Appendix A.

Pressure Modes and Requirement for Mixed Interpolation

The process of "element selection" and "underlying finite-dimensional approximation space" for both velocity and pressure is presented in this section. Early published finite-element solutions of the Navier-Stokes equations employed a so called "equal interpolation"; i.e. $\varphi = \phi$ (Hood and Taylor 1973). The authors noticed that an accurate solution for the velocity was usually accompanied by a very poor (or meaningless) pressure solution. When "mixed interpolation" (or "unequal interpolation") was employed, in which φ is one order lower (in polynomial degree) than ϕ, both velocity and pressure results appeared to be more reasonable (Hood and Taylor 1974).

Sani et al. (1981a, b) and Olson and Tuann (1978) made significant progress toward providing an explanation for the occurrence of the spurious pressure solutions. They concluded that equal interpolation generally results in a singular matrix with associated zero eigenvalues. These spurious pressure solutions (pressure modes) are simply an artifact of the discretization method employed - "basis functions" in finite element method (FEM) and "grid selection and variable locations" in finite difference method (FDM) of the Navier-Stokes equations, which also display spurious pressure modes (Patankar 1982).

The significant difficulties associated with the singular limit can be easily appreciated and the spurious pressure mode better understood by considering the following simple example with only two equations:

$$\begin{bmatrix} 1 & 0 \\ 0 & 0 \end{bmatrix} \begin{Bmatrix} \lambda_1 \\ \lambda_2 \end{Bmatrix} = \begin{Bmatrix} 1 \\ 0 \end{Bmatrix} \tag{19}$$

The matrix has eigenvalues $\lambda_1 = 1$, $\lambda_2 = 0$ and the linear system has the solution $\{1, \quad c\}^T$, where c is arbitrary. A small perturbation in the off-diagonal elements gives

$$\begin{bmatrix} 1 & \varepsilon \\ \varepsilon & 0 \end{bmatrix} \begin{Bmatrix} \hat{\lambda}_1 \\ \hat{\lambda}_2 \end{Bmatrix} = \begin{Bmatrix} 1 \\ 0 \end{Bmatrix} \tag{20}$$

The matrix now has eigenvalues $\hat{\lambda}_1 = (1+\sqrt{1+4\varepsilon^2})/2 \cong 1+\varepsilon^2$ and $\hat{\lambda}_2 = (1-\sqrt{1+4\varepsilon^2})/2 \cong -\varepsilon^2$, and the algebraic system has the solution $\{0, \quad \varepsilon^{-1}\}^T$. The first component is changed by O(1) and the second by $O(\varepsilon^{-1})$; furthermore, the unperturbed solution cannot be recovered by letting ε approach zero. Fortunately, the useful pressure information can be recovered from the spurious pressure solution using smoothing techniques (Hughes et al. 1979, Lee et al. 1979, Hinton and Campbell 1974).

Because of the choice of pressure discretization, the resulting discrete system of equations may involve ill-conditioning and round-off error in practice. Pelletier et al. (1989) have invented several inexpensive techniques to minimize the effect of round-off error based on the measurement of incompressibility for the discrete divergence of the velocity field and recommended the use of discontinuous, C^{-1}, pressure approximations, particularly for strongly coupled flow problems. The element employing discontinuous $\left(C^{-1}\right)$ can guarantee element level mass balances, $\int_{\Omega^e} \nabla \cdot \underline{u}^h = 0$, which must be judged as an additional advantage. Continuous $\left(C^0\right)$ pressure approximation, on the other hand, can only be shown to yield a global mass balance (Gresho et al. 1980). Bercovier and Engelman (1979) have also demonstrated the superiority of the nine-node isoparametric quadrilateral element over the eight-node (serendipity) element in many computational experiments. Therefore we use 9-node Lagrange element for velocity interpolation and 4-node discontinuous bilinear interpolation for the pressure in our study. The pressure degrees of freedom are located at the four points of 2×2 Gaussian integration points.

Solution Procedure

The discrete system resulting from a finite-element discretization of the Navier-Stokes equations consists of a nonlinear system of algebraic equations. In order to improve the performance of the solution algorithms, all equations in the problem are solved in a fully coupled manner. Both the solution method for a system of equations and the solution algorithm for the nonlinear system of equations are major factors influencing the efficiency of the finite-element program.

The major computational effort in any finite element procedure is expended in the solution of the assembled matrix equations that describe the discretized problem. The solver adopted to determine this solution has a significant bearing on the computer storage requirements and execution time. Of the many techniques available, the direct elimination frontal equation solution technique originated by Iron (1970) has earned the reputation of being easy and inexpensive to use. The main idea of the frontal solver is to assemble the equations and eliminate the variables at the same time. As soon as the coefficients of an equation are completely assembled from the contribution of all relevant elements, the corresponding variable can be eliminated. Therefore, the complete global matrix is never actually formed, since all reduced equations can be eliminated from core storage and stored on disc. Following the completion of equation assembly and reduction element-by-element, the stored information is used during the back substitution process to obtain the solution.

For highly coupled, nonlinear equations such as the Navier-Stokes equations, questions arise regarding the ability of the numerical algorithm to achieve a solution in addition to the computational efficiency. The choice of a solution algorithm is therefore a critical element in the overall utility, robustness and efficiency of a computer code. The most common methods employed, (a) successive-substitution method and (b) Newton's method, are summarized as follow:

(a) Successive-Substitution Method

A particularly simple iterative method with a large radius of convergence is the successive substitution (Picard, functional iteration) method. Application of the method for (17) is described by

$$\underline{\underline{A}}\left(\underline{w}^{n}\right)\underline{w}^{n+1} = \underline{b}\left(\underline{w}^{n}\right) \tag{21}$$

where the superscripts indicate the iteration levels. For strongly nonlinear problems the rate of convergence of (21) is fairly slow since it is a first-order method. An improvement in the convergence rate can sometimes be realized by use of a relaxation formula where

$$\underline{\underline{A}}(\underline{w}^n)\underline{w}^* = \underline{b}(\underline{w}^n) \tag{22}$$

and

$$\underline{w}^{n+1} = \alpha\underline{w}^n + (1-\alpha)\underline{w}^*, \quad 0 \le \alpha \le 1 \tag{23}$$

where α is the relaxation factor.

(b) Newton Method

In order to improve significantly on the rate of convergence, a second-order method, such as Newton's method, can be considered. Rewriting (17) as

$$\underline{R}(\underline{w}) = \underline{\underline{A}}(\underline{w})\underline{w} - \underline{b}(\underline{w}) \tag{24}$$

Then Newton's method can be expressed as

$$\underline{R}(\underline{w}^n) = -\frac{\partial \underline{R}}{\partial \underline{w}}\Big|_{\underline{w}^n} (\underline{w}^{n+1} - \underline{w}^n) = -\underline{\underline{J}}(\underline{w}^n)(\underline{w}^{n+1} - \underline{w}^n) \tag{25}$$

which can be solved for $\underline{w}^{n+1}$ as

$$\underline{w}^{n+1} = \underline{w}^n - \underline{\underline{J}}^{-1}(\underline{w}^n)\underline{R}(\underline{w}^n) \tag{26}$$

where $\underline{\underline{J}}(\underline{x})$ is the Jacobian matrix. The Newton scheme has a superior rate of convergence compared to the simple algorithm in (21). However, Newton's method also has a somewhat smaller radius of convergence (i.e., is more sensitive to the initial guess of $\underline{w}^0$). The Newton method can at times be improved by the use of a relaxation procedure similar to the one shown in (22) and (23). In some cases a sequential application of (21) and (26) provides the best method of solution.

Appendix A:

The weak form of momentum equation, (1), and associated boundary conditions, (4) and (5), is obtained by first multiplying the equation by any of the velocity basis function (i.e., by a test function), ϕ_i , i = 1, 2, ..., L where there are L velocity nodes in the discretized domain, and integrating over the domain, Ω

$$\int_{\Omega} \phi_i \rho u_\beta u_{\alpha,\beta} = \int_{\Omega} \phi_i \tau_{\alpha\beta,\beta} \tag{A-1}$$

Then, since $\phi_i \tau_{\alpha\beta,\beta} = \left(\phi_i \tau_{\alpha\beta}\right)_{,\beta} - \phi_{i,\beta} \tau_{\alpha\beta}$, and from the divergence theorem

$$\int_{\Omega} \left(\phi_i \tau_{\alpha\beta}\right)_{,\beta} = \int_{\partial\Omega} \phi_i n_\beta \tau_{\alpha\beta} \tag{A-2}$$

where $\partial\Omega$ is the boundary of Ω and n_α is the α −component of the outward unit normal vector on $\partial\Omega$. To incorporate the boundary condition, (5), $n_\beta \tau_{\alpha\beta} = \tilde{\tau}_\alpha$, (A-1) becomes

$$\int_{\Omega} \phi_i \rho u_\beta u_{\alpha,\beta} = \int_{\partial\Omega} \phi_i n_\beta \tau_{\alpha\beta} - \int_{\Omega} \phi_{i,\beta} \tau_{\alpha\beta} = \int_{\partial\Omega} \phi_i \tilde{\tau}_\alpha - \int_{\Omega} \phi_{i,\beta} \tau_{\alpha\beta} \tag{A-3}$$

Similarly, the appropriate weak form of continuity equation, (2), is obtained by multiplying it by any one of the pressure basis functions (as a test function), say φ_j , j = 1, 2, ..., M where there are M pressure "nodes" - they are located at the 2×2 Gaussian integration points in each element - in the discretized domain. Thus (2) becomes, in the weak form

$$\int_{\Omega} \varphi_j u_{\alpha,\alpha} = 0 \;\; ; \;\; j = 1,2,...,M \tag{A-4}$$

Using the definition of the Galerkin procedure, (8) and (9), and the finite element approximations, (6) and (7), (A-3) and (A-4) can be written as

$$\left(U_\beta^k \int_{\Omega} \rho \phi_i \phi_k \phi_{j,\beta}\right) U_\alpha^j + \left(\int_{\Omega} \mu \phi_{i,\beta} \phi_{j,\beta}\right) U_\alpha^j - \left(\int_{\Omega} \phi_{i,\alpha} \varphi_j\right) P_j = \int_{\partial\Omega} \phi_i \tilde{\tau}_\alpha \; ; \; \text{i} = 1, 2, ..., \text{L} \tag{A-5}$$

and $$\left(\int_{\Omega} \varphi_j \phi_{i,\alpha}\right) U_\alpha^i = \underline{0} \; ; \; j = 1, 2, ..., M \tag{A-6}$$

The corresponding matrix equations (ODE's) can be written in the condensed form

$$[\underline{\underline{N}}(\underline{U}) + \underline{\underline{K}}]\underline{U} + \underline{\underline{C}}\underline{P} = \underline{f} \tag{A-7}$$

$$\underline{\underline{C}}^T \underline{U} = \underline{0} \tag{A-8}$$

Where now $\underline{U}$ is a global vector of length d*L, where d is the number of dimensions, and $\underline{P}$ is a global M-vector of pressures. The associated matrices for the two-dimensional situation can be explicitly expressed as

$$\underline{\underline{N}}(\underline{U}) = \begin{bmatrix} U_k \int_{\Omega} \rho \phi_i \phi_k \phi_{j,x} + V_k \int \rho \phi_i \phi_k \phi_{j,y} & \underline{0} \\ \underline{0} & U_k \int_{\Omega} \rho \phi_i \phi_k \phi_{j,x} + V_k \int_{\Omega} \rho \phi_i \phi_k \phi_{j,y} \end{bmatrix} \tag{A-9}$$

$$\underline{\underline{K}} = \begin{bmatrix} \int_{\Omega} \mu\left(\phi_{i,x}\phi_{j,x} + \phi_{i,y}\phi_{j,y}\right) & \underline{0} \\ \underline{0} & \int_{\Omega} \mu\left(\phi_{i,x}\phi_{j,x} + \phi_{i,y}\phi_{j,y}\right) \end{bmatrix} \tag{A-10}$$

$$\underline{\underline{C}} = -\begin{bmatrix} \int_{\Omega} \varphi_j \phi_{i,x} \\ \int_{\Omega} \varphi_j \phi_{i,y} \end{bmatrix} \tag{A-11}$$

$$\underline{f} = \left\{ \int_{\partial\Omega} \phi_i \tilde{\tau}_\alpha \right\} \tag{A-12}$$

where U and V are the velocity components on the x- and y- coordinates, respectively.

The various matrices expressed in (A-9) - (A-11) are spatial integrals of the various interpolation functions and their derivatives. The evaluation of these integrals can be carried out by the use of numerical quadrature procedure.

FUTURE COMPUTATIONAL TASKS

Each step involves mathematical formulation, numerical implementation, computer code, debugging, and post processing phases.

1. Computational Analysis of the Solid Phase

a. Implementation of a thin shell code (steady state, 3-dimensional, linear, isotropic material behavior) with sheet under tension on bottom and/or top edges and subject to gravity.

b. Local to global coordinate transformation

c. Analysis of the effects of time-dependent boundary conditions.

2. Fluid/Solid Interaction: Computational Analysis

Steady State:

d) Complete the linear (excluding the convective terms) two-dimensional formulation for nondeforming boundary and laminar flow

e) Complete the nonlinear (include all terms in the N.S. equations) two-dimensional numerical formulation for nondeforming boundary and laminar flow.

f) Add a sub-grid scale turbulent model with the law of the wall for resolution of the sub-layer viscous boundary including an unstructured grid formation.

g) Add porous media equations for analyzing a moving permeable layer (paper).

h) Include the appropriate interface equations for the air/sheet boundary or interface conditions

i) Develop a technique for a moving sub-domain boundary (paper) problem

Unsteady Flow

j) Extend all of the above formulations for unsteady flow and/or unsteady boundary conditions

k) Add terms for deformable boundary problems. These include the equations for isotropic deformable porous solid layers

Three-Dimensional Flow:

l) Extend the formulations for three-dimensional equations for laminar flow

m) Extend the boundary conditions for three-dimensional boundaries

n) Include the anisotropic characteristics of the porous layer (paper).

TIMETABLE

DELIVERABLES	'94		'95		'96		'97	
BY TASKS	Sp	Fall	Sp	Fall	Sp	Fall	Sp	Fall
SOLID PHASE								
a Complete								
b Complete								
c Complete								
CFD STEADY STATE								
d ----------| Complete								
e ----------| Complete								
f ----------|							
g ------|							
h ---------|							
UNSTEADY FLOW								
i ------|							
j ----------|							
k --------|							
THREE-DIMENSIONAL UNSTEADY FLOW								
l ----------|							
m ----------|							
n ----------|							

MORE EFFECTIVE METHOD OF MOISTURE REMOVAL IN THE DRYER

Our computational analyses have shown that eddies form above the dryer rolls in the dryer section. A ventilation device is outlined below which replaces the eddies with a more efficient air stream for moisture removal.

A schematic of the air stream in the dryer unit is presented below in Figure 1. The actual results from the computational analysis are given below in color coded plots of streamlines and velocity vector plots. The colors indicate the magnitude of the dependent variables. The computational results show that recirculating eddies with closed streamlines develop near the dryer roll. This is a potential area for accumulation of moisture which in turn reduces the efficiency of the dryer. With this invention, the eddies are completely removed from the system. This results in less accumulation of moisture and, therefore, a more efficient drying process.

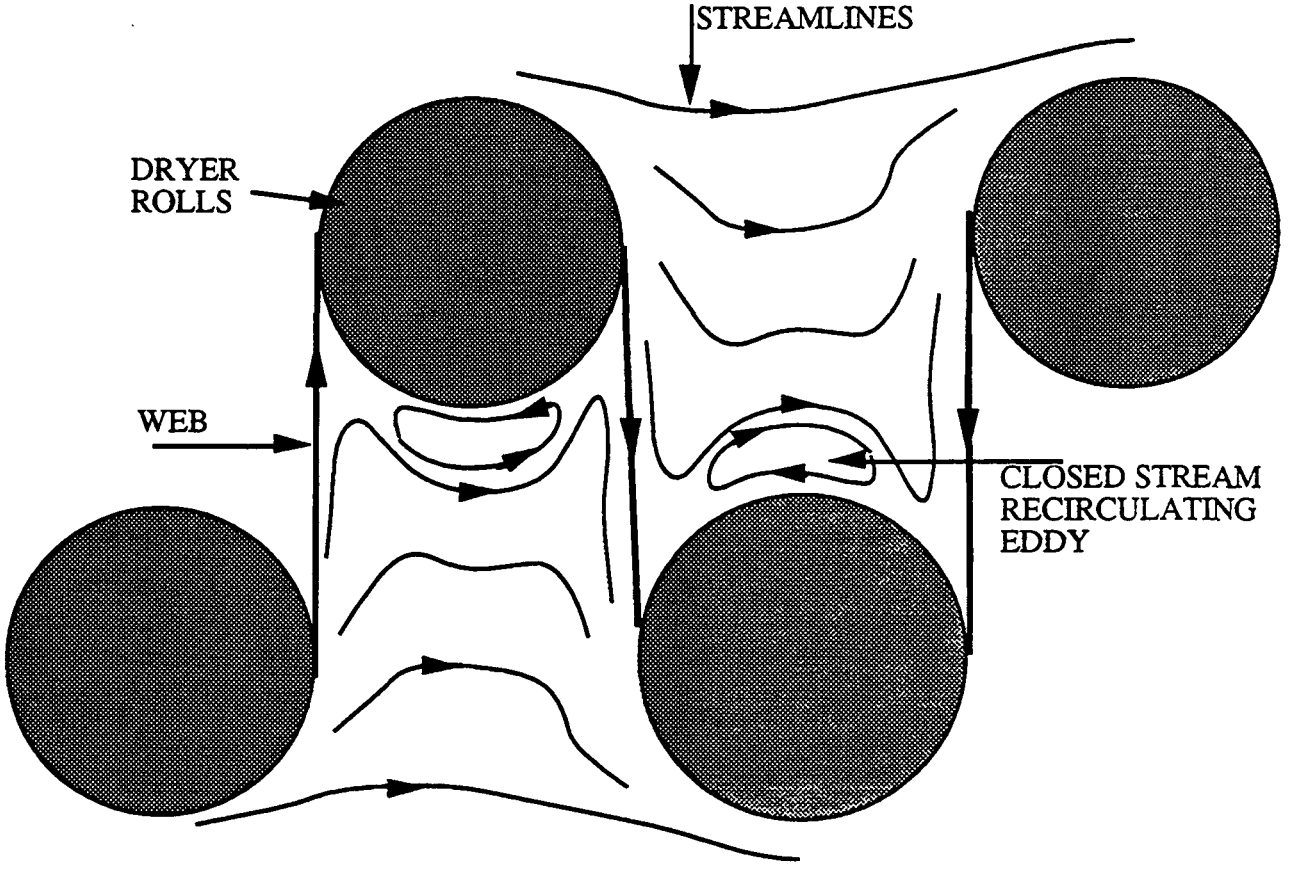

Figure 1. Schematic of the air stream at low speed in the dryer section of a paper machine.

The invention consists of ventilation tubes that are placed at the center of the eddies near the rolls to modify the streamlines and prevent formation of the recirculating eddies, as shown in Figure 2. The ventilation tubes have suction capability at the top portion and air delivery feature at the designated section of the tubes, as shown in Figure 3.

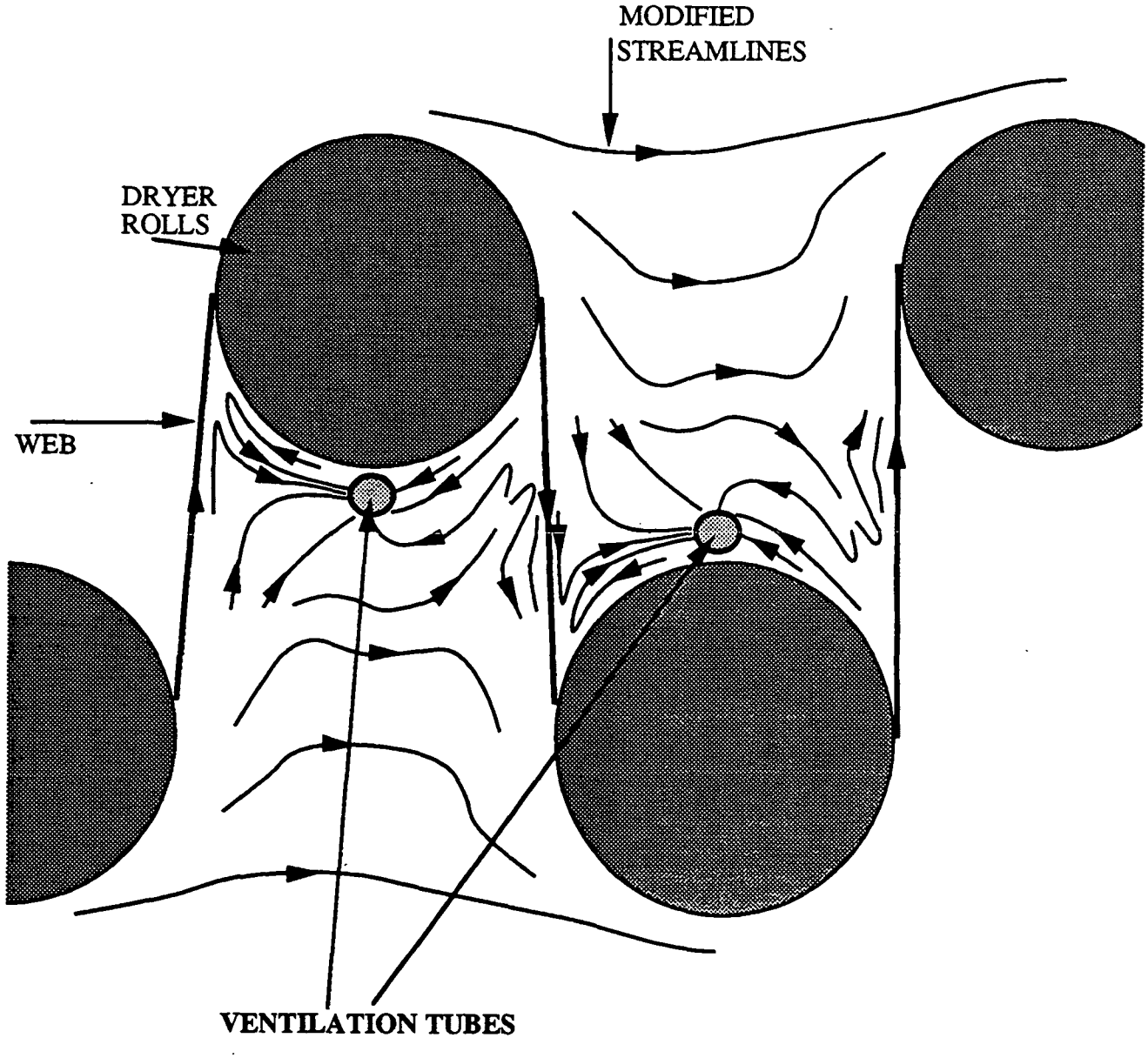

Figure 2. The schematic of the dryer section with ventilation tubes showing the modified streamlines and the destruction of the eddies.

The ventilation tubes can be of different shapes with two primary sections. Depending on the position of the tubes, the top (bottom) portion of the tubes extract (inject) air from (into) the dryer section when the tubes are located above (below) the dryer roll. The drawings in Fig. 3 show three different shapes that can be used effectively to reduce moisture accumulation and to ventilate the system effectively for higher efficiency drying. The shape of the designs depend on the machine speed and the need to streamline the surface of the tube in order to prevent flow separation.

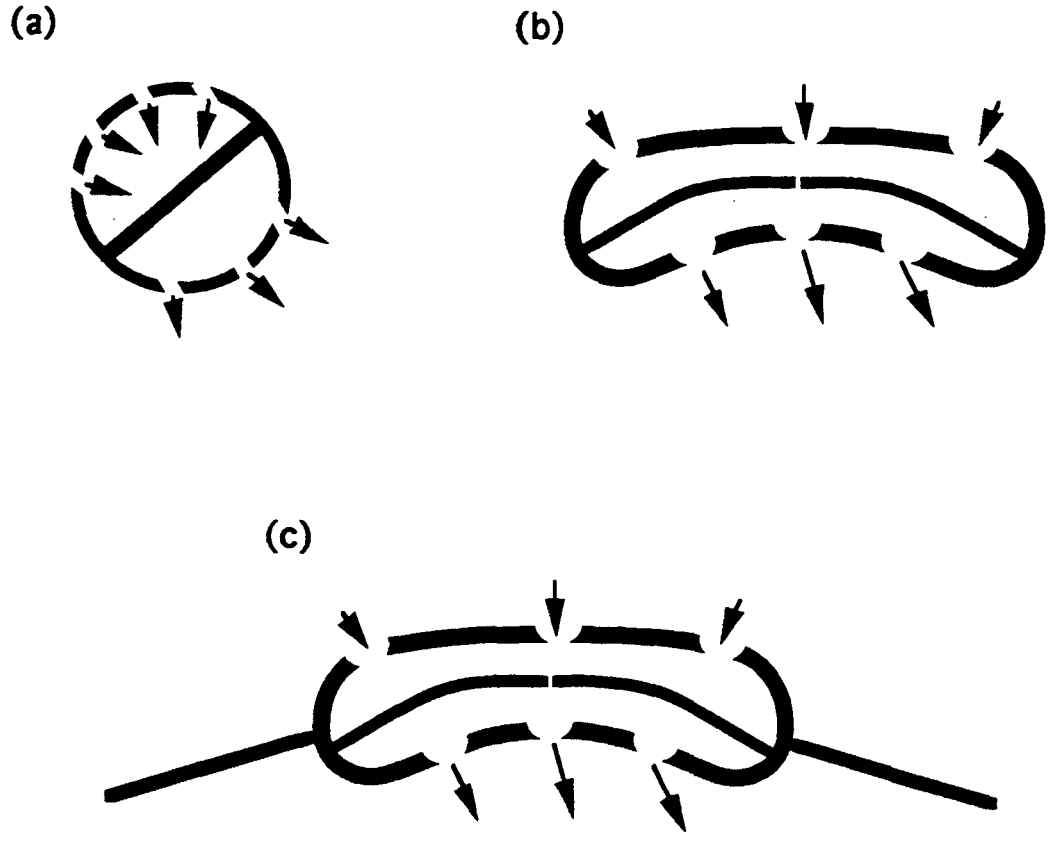

Figure 3. Three different ventilation tubes for removing moisture from the steam rolls in the dryer section. Versions (b) and (c) are aerodynamically designed to prevent further flow separation near the roller for high speed machines. Version (a) is a simple circular tube for low speed machines.

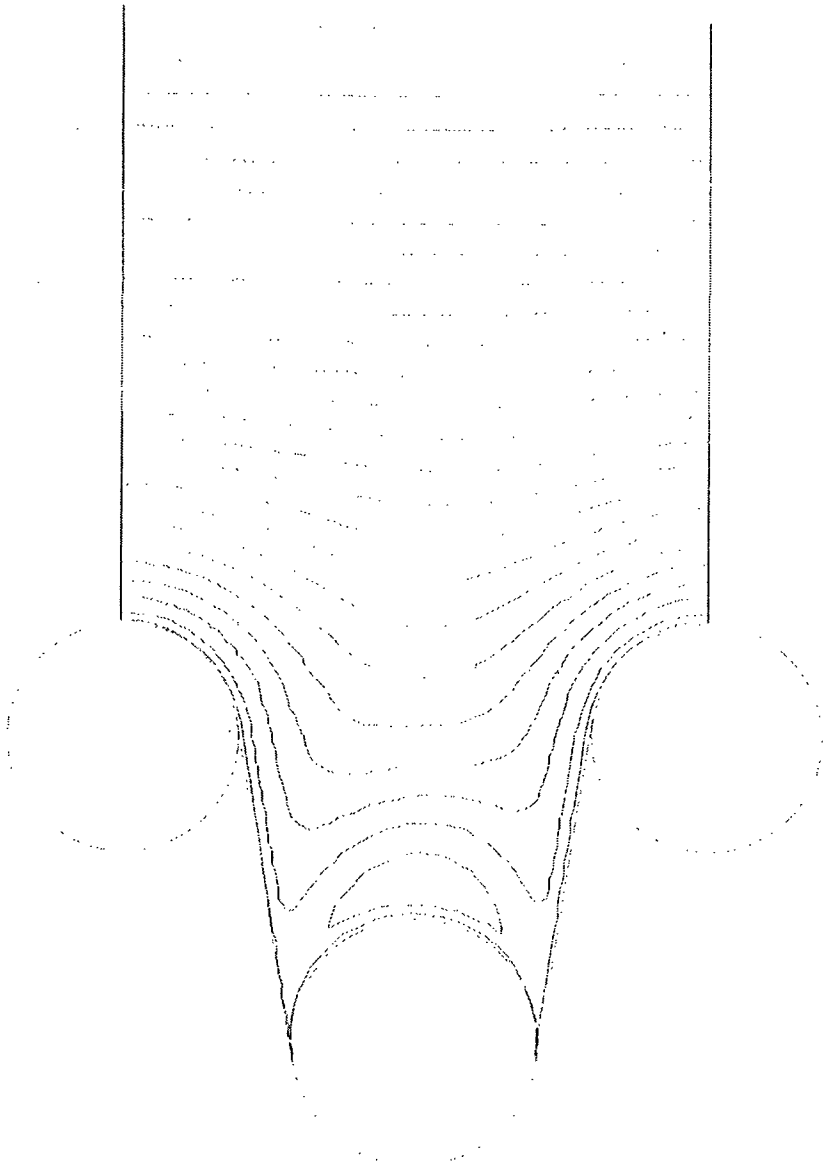

LEGEND

.3233E-01
.2105E+00
.3293E+00
.5075E+00
.6263E+00
.8045E+00
.9233E+00
.1101E+01
.1220E+01
.1398E+01
.2400E+01
.2586E+01
.2705E+01
.2883E+01

Y

X

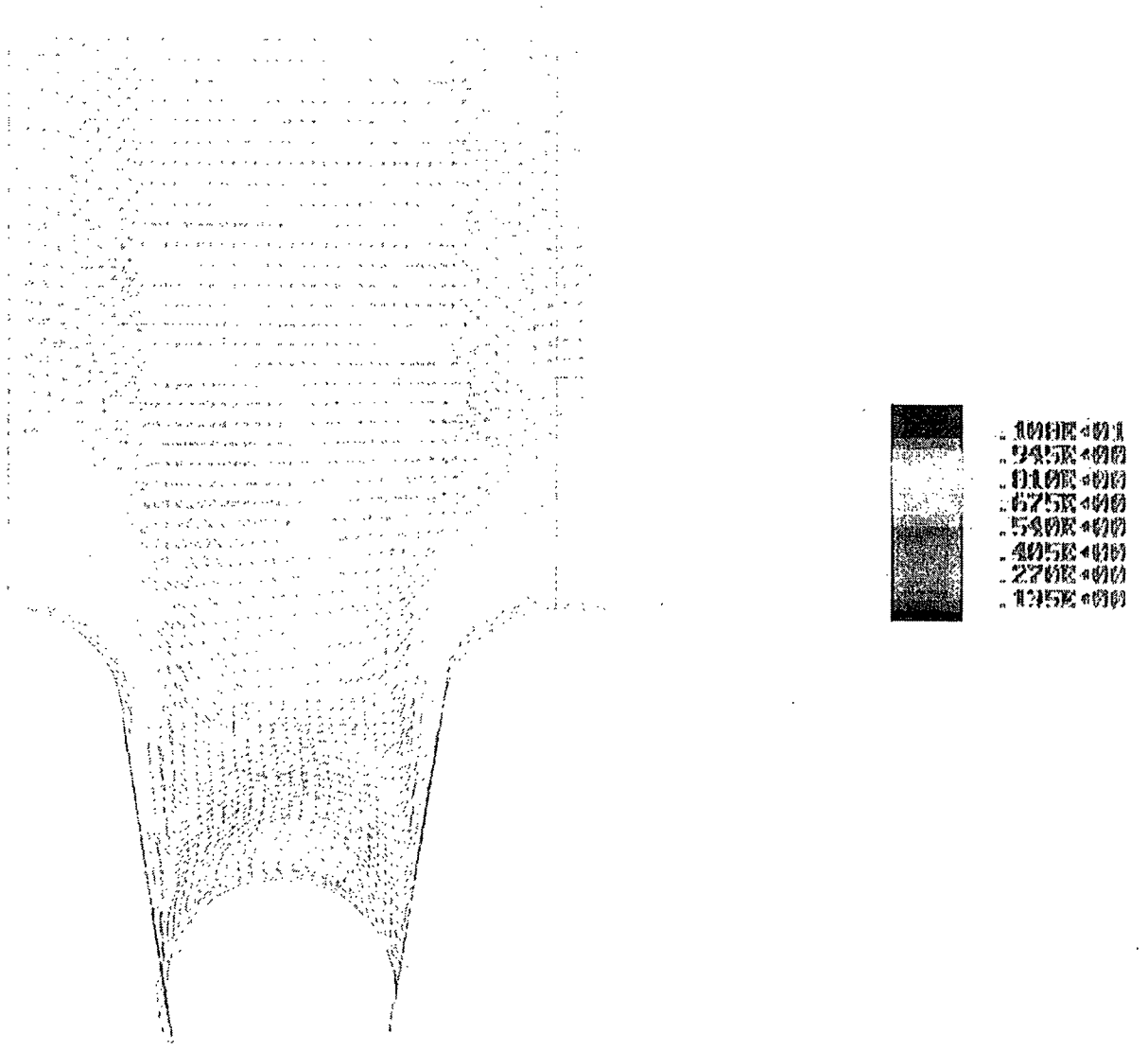
.1091E+01
.9457E+00
.8104E+00
.6751E+00
.5398E+00
.4045E+00
.2692E+00
.1339E+00

References:

1. Pramila, A. "Sheet Flutter and the Interaction between Sheet and Air", *TAPPI J.*, July 1986, pp. 70 - 74.

2. Pramila, A. "Natural Frequencies of Submerged Axially Moving Band", *Sound and Vibration,* Vol. 113, No. 1, 1987, pp. 198 - 203.

3. Chang, Y., Moretti, P., "Interaction of Fluttering Webs with Surrounding Air ", *TAPPI,* Engineering Conference 1990, pp.175 - 182.

4. Race, E, Wheeldon, J. B., and Fraser-Clark, D., "Air Movement Induced by Felts and Fabrics and its Ventilation Effect on Dryer Pockets",*TAPPI*, Vol. 51, No. 7, July 1968, pp. 51A - 56A.

5. Soininen, M. "The Physics of Paper Machine Sheet Flutter", *International Water Removal Symposium,* 1982, pp. 85 - 86.

6. Sieverding, C. H., Bosche, P. V. "The Use of Coloured Smoke to Visualize Secondary Flows in a Turbine-Blade Cascade", *Journal of Fluid Mechanics*, Vol. 134, 1983 (Revised Form), pp. 85 - 89.

7. Bercovier, M. and M. Engelman, "A Finite Element for the Numerical Solution of Viscous Incompressible Flows", Journal of Computational Physics, Vol. 30, 181-201 (1979).

8. Christoudoulou, K.N. and L.E. Scriven, "The Fluid Mechanics of Slide Coating", Journal of Fluid Mechanics, Vol. 208, 321-354 (1989).

9. Curvelier, C., A. Segal and A.A. v Steenhoven, Finite Element Methods and Navier-Stokes Equations, Reidel, Dordrecht (1986).

10. Gresho, P.M., "Some Interesting Issues in Incompressible Fluid Dynamics, Both in the Continuum and in Numerical Simulation", Advances in Applied Mechanics, Vol. 28, 45-140 (1992).

11. Gresho, P.M., "Incompressible Fluid Dynamics: Some Fundamental Formulation Issues", Annual Review of Fluid Mechanics, Vol. 23, 413-453 (1991).

12. Gresho, P.M. and R.L. Lee, "Don't Suppress the Wiggles - They're Telling You Something!", Computers & Fluids, Vol. 9, 223-253 (1981).

13. Gresho, P.M., R.L. Lee, R.L. Sani and T. Stullich, "On the Time-Dependent FEM Solution of the Incompressible Navier-Stokes Equations in Two- and Three-Dimensions", Recent Advances in Numerical Methods in Fluids, Vol. 1, 27-81, Pineridge Press, Ltd., Swansea, UK (1980).

14. Gunzburg, M.D., Finite Element Methods for Viscous Incompressible Flows. A Guide to Theory, Practice, and Algorithms, Boston, Academic Press (1989).

15. Hinton, E. and J.S. Campbell, "Local and Global Smoothing of Discontinuous Finite Element Functions Using a Least Square Method", International Journal for Numerical Methods in Engineering, Vol. 8, 461-480 (1974).

16. Hood, P. and C. Taylor, "Navier-Stokes Equation using Mixed-Interpolation", in Finite Element Methods in Flow Problems, UAH Press, Huntsville, 57-66 (1974).

17. Hood, P. and C. Taylor, "A Numerical Solution of the Navier-Stokes using FEM Technique", Computers & Fluids, Vol. 1, 73-100, 1973.

18. Hughes, T.J.R., W.K. Liu and A. Brook, "Finite Element Analysis of Incompressible Viscous Flows by the Penalty Function Formulation", Journal of Computational Physics, Vol. 30, 1-60 (1979).

19. Iron, B.M., "A Frontal Solution Program", International Journal for Numerical Methods in Fluids, Vol. 2, 5-32 (1970).

20. Kistler, S.F. and L.E. Scriven, "Coating Flow Theory by Finite Element and Asymptotic Analysis of the Navier-Stokes System", International Journal for Numerical Methods in Fluids, Vol. 4, 207-229 (1984).

21. Lee, R.L., P.M. Gresho and R.L. Sani, "Smoothing Techniques for Certain Primitive Variable Solutions of the Navier-Stokes Equations", International Journal for Numerical Methods in Fluids, Vol. 14, 1785-1804 (1979).

22. Olson, M. and S. Tuann, "Primitive Variables versus Stream Function Finite Element Solutions of the Navier-Stokes Equations", in Finite Element in Fluids, Vol. 3, 73-89, Wiley, Chichester (1978).

23. Patankar, S.V., Numerical Heat Transfer and Fluid Flow, Hemisphere, Washington DC (1980).

24. Pelletier, D.H., A. Fortin and R. Camarero, "Are Solutions of Incompressible Flows Really Incompressible? (Or How Simple Flows Can Cause Headaches!)", International Journal for Numerical Methods in Fluids, Vol. 9, 99-112 (1989).

25. Sackinger, P.A., R.A., Brown and J.J. Derby, "A Finite Element Method for Analysis of Fluid Flow, Heat Transfer, and Free Surfaces in Czochralski Crystal Growth", International Journal for Numerical Methods in Fluids, Vol. 9, 453-492 (1989).

26. Sani, R.L., P.M. Gresho, R.L. Lee and D.F. Griffiths, "The Cause and Cure (?) of the Spurious Pressures Generated by Certain FEM Solutions of the Incompressible Navier-Stokes Equations: Part 1", International Journal for Numerical Methods in Fluids, Vol. 1, 17-43 (1981).

27. Sani, R.L., P.M. Gresho, R.L. Lee, D.F. Griffiths and M. Engelman, "The Cause and Cure (?) of the Spurious Pressures Generated by Certain FEM Solutions of the Incompressible Navier-Stokes Equations: Part 2", International Journal for Numerical Methods in Fluids, Vol. 1, 171-204 (1981).

28. Thomasset, F., Implementation of Finite Element Methods for Navier-Stokes Equations, New York, Springer-Verlag (1981).

ACKNOWLEDGMENT

This member funded project is a joint effort between the Institute of Paper Science and Technology and the School of Mechanical Engineering At Georgia Institute of technology. The windtunnel facilities of the School of Mechanical Engineering have been used for part of these studies. The efforts at Georgia Tech. are under the direction of Professor Paul Neitzel. Postdoctoral Associate, Shin-Jye Liang is working on the numerical aspects of this project. Maxim Poliashenko is working on the computational stability methods.

FUNDAMENTALS OF COATING SYSTEMS

STATUS REPORT

FOR

PROJECT 3674

March 22, 1994
Institute of Paper Science and Technology
Atlanta, Georgia

Project Title: Fundamentals of Coating Systems
Project Staff: Cyrus K. Aidun
Budget (FY 93-94): $125,000
Reporting Period: Spring '93 to Fall '93
Project No.: 3674

OBJECTIVES:

(1) To investigate the cause and origin of coat weight nonuniformities reported in high-speed blade coating of paper and board, (2) to explore novel coating systems for application of a more uniform coat weight profile at higher machine speeds.

TASKS COMPLETED DURING THE LAST PERIOD:

An objective of this project is the development of new and novel coating systems. In this section, we refer to a novel coating system as the *vortex-free* coater. The *single layer* and *double layer* coaters imply coater heads that apply a single layer of coating or two layers of wet-on-wet coatings, respectively. A list of only the major tasks and an estimated timetable are provided below.

1. Flow visualization studies of air entrainment with Beloit's short-dwell coater head installed on IPST's current coating flow visualization facilities (maximum speed = 3300 fpm).

2. Design an initial version of the single layer vortex-free coater head to be constructed as an experimental prototype. Install and Perform Flow visualization studies/evaluation of

the prototype single layer vortex-free coater head on the IPST experimental coater.

3. This task involves a long-term program on rheological characterization of coating colors. After installing the Fluid Spectrometer (RFS II) in our Coating Rheology Laboratory in March of this year, we will evaluate the rheological characteristics of three standard coating formulations that are being used by Beloit. We will continue to evaluate various coating formulations in terms of rheological characteristics and runnability as requested by member companies.

4. One of the two patent applications for the vortex-free coater, SN 137,957 has been approved and will be granted to IPST shortly. The second patent applications, SN 849,530, is pending. We are in the process of filing for foreign patents of both of the new coating systems.

FUTURE TASKS:

1. Design and construct a transparent roll for high speed flow visualization.

2. Perform flow visualization studies of the short-dwell coater head at up to 6600 fpm.

3. Perform flow visualization studies of the vortex-free coater head at up to 6600 fpm.

4. Continue the computational studies and optimization of the single- and double-layer vortex-free coater by including the rheological properties of the coating color and the deformation of the blade and the substrate.

5. Start the design and construction of a pilot scale single layer vortex-free coater. We anticipate that the pilot scale trials will be performed at Beloit.

The time requirements for each task are estimated as:

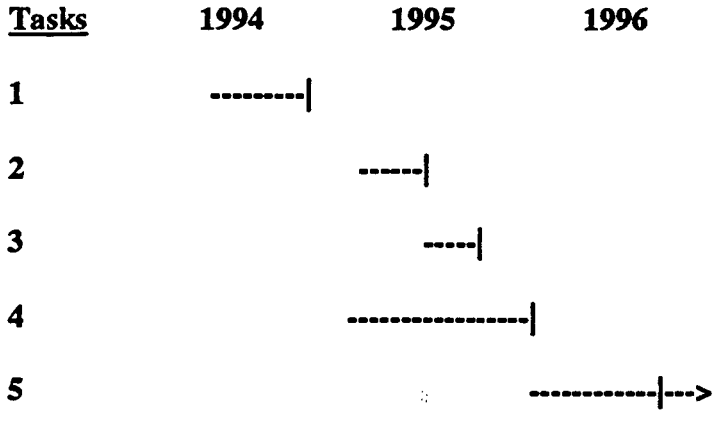

SUMMARY OF RESULTS:

In the last report, we outlined various physical mechanisms that we have found to result in macroscopic coating defects in blade coating. In summary, there are three dominant mechanisms by which coating film thickness can be adversely affected. These are:

(1) pressure fluctuations upstream of the blade,

(2) flow instability upstream of the blade, and

(3) air entrainment at the wetting line.

The interrelation between these effects are summarized in the last report. Below, we will summarize the results from recent computational flow visualization experiments with a vortex-free coater.

COMPUTATIONAL EXPERIMENTS

The basic configuration of the vortex-free coater (Aidun, SN 881,512, and SN 849,530) is shown in Figure 1. This coater has stationary walls with the exception of the substrate which moves with the machine speed. The coating fluid is pumped into a channel that leads the flow to the moving web. Near the web the liquid accelerates through viscous drag while near the stationary wall it decelerates with a commensurate amount. The flow entering the blade gap has a nearly Poiseuille-Couette flow distribution. The operating parameters and consequently, the velocity distribution determine the coating thickness. In the wedge like region formed by the blade and the substrate, the pressure sharply increases and has a maximum value near the stagnation point located right under the tip of the blade. The rest of the flow, which could not exit at the gap,

is forced to change direction and accelerated by a favorable pressure gradient as it leaves the system via another channel along the blade face. Far downstream from the blade the free surface coating fluid moves with uniform velocity together with the substrate. Near the blade tip the shape of the free surface is determined by the ambient pressure and the surface tension effects. The deformation of the blade, neglected in the present study, will be considered as soon as the elastohydrodynamic computational code is fully developed (Cody and Aidun, 1993).

1. Applicator with stationary walls

Tables 1 to 3 show the input parameters for the cases considered in this section. Table 1 presents the computational experiments carried out assuming Newtonian fluid, while Tables 2 and 3 consider the non-Newtonian behavior of the coating liquid. In the second column, U_p, the maximum inflow velocity, is used as the characteristic velocity, i.e. U. It is assumed that the inflow velocity has a parabolic distribution (Poiseuille flow). The characteristic length, L_{in}, the width of the inlet channel, can be found in the third column. Furthermore, L_{gap} denotes the width of the gap between the blade and the substrate and q is the flowrate per unit width entering the coater.

In the first numerical experiments, shown in Table 1, the web velocity (U_w) is gradually increased from 1 m/s to 40 m/s. At the same time the fluid discharge (q) is also increased. A weak eddy appears at the second curve of the applicator wall in case of B2. This eddy gets stronger for cases B3 to B7. In conjunction with the formation of this eddy, a second elongated eddy appears while the separation point moves closer to the first curve of the applicator wall (see Figure 2). In cases of B6 and B7 a third small eddy is also noticeable located close to the blade, right under the first strong eddy. Figure 2 shows the flow pattern corresponding to the runs B1 to B7. The pressure distribution along the substrate is shown in Figure 3 for these cases. A strong eddy reduces the hydrodynamic pressure on the substrate.

Under the blade the pressure distribution reaches a maximum then drops to a minimum before the ambient pressure becomes dominant for the free surface coated layer. Figure 4 illustrates

the pressure distribution along the blade. Right under the sharp edge of the blade (the toe) the pressure reaches its maximum then it sharply decreases followed by a more gradual decrease. The pressure increases approximately 40 times from case B1 to B7. Note that these Figures show the differences between the local pressure and the ambient pressure.

The numerical experiments denoted by C1 , C2 , and C3 in Table 2 have the same geometry as experiments B1 to B7. However, in these cases, the shear thinning effect of the coating fluid is considered using a Carreau model, given by

$$\mu = \mu_\infty + (\mu_\circ - \mu_\infty)(1 + K^2 \varepsilon_{ij}\varepsilon_{ij})^{(n-1)/2} \tag{1}$$

In the above equation μ_0 and μ_∞ are the zero and infinite shear rate viscosities, respectively, and K is the time constant. In the case of n=1 the Carreau model gives the Newtonian viscosity, i.e. $\mu = \mu_0$.

The stress tensor can be written as

$$\sigma_{ij} = -p\delta_{ij} + \tau_{ij} \tag{2}$$

where p is the pressure, τ_i is the deviatoric stress tensor and δ_i is the Kronecker delta. In the present study, the constitutive relation has the following form

$$\tau_{ij} = 2\mu\varepsilon_{ij} \tag{3}$$

In this equation, μ denotes the dynamic viscosity and ε_{ij} stands for the strain tensor defined by

$$\varepsilon_{ij} = \frac{1}{2}\left(\frac{\partial u_i}{\partial x_j} + \frac{\partial u_j}{\partial x_i}\right) \tag{4}$$

The viscosity, μ, is constant for a Newtonian fluid where for the more typical coating fluids, the viscosity decreses with shear, more or less as described by the Carreau model in Eq. (1).

It is observed that the three eddies described above for the Newtonian case appear even stronger for the non-Newtonian case. This is the result of the reduction in viscosity due to large velocity gradients (see the form of the Carreau model). To see when the eddies disappear for the case of U_w =20 m/s, the discharge q is gradually increased in the runs C11 to C15. Figure 5 illustrates the change in the streamline pattern for these cases. In the case C13, there is only one week eddy attached to the second curve of the applicator wall. Therefore, the discharge has to be increased from 5 l/s/m to approximately 20 l/s/m in order to suppress the eddies.

It is also interesting to see how the pressure distribution along the substrate and the blade are modified by increasing the discharge rate as it is shown in Figures 6 and 7, respectively. For C11, the pressure gradually increases downstream along the substrate and reaches a local maximum. This local maximum is followed by a local minimum where the pressure increases to a maximum right under the sharp edge of the blade. Near the static contact line near the meniscus, the pressure decreases to a minimum where it gradually asymptotes to the ambient pressure. With increasing fluid discharge in the cases of C11 to C15, there are no more local minima and maxima in pressure. The maximum pressure level increases approximately 60% from C11 to C13.

In order to suppress the eddies in the present coating system, the experiments denoted by N1 to N4 in Table 3 employ a new geometry. In this new configuration the width of the channel under the substrate is reduced to about 2/3 of the width in the previously described experiments. The streamlines of the flow field for these cases are shown in Figure 8. It is seen that at U_w= 10 m/s there is only one weak eddy near the second curve of the applicator wall. At U_w = 20 m/s the second elongated weak eddy appears and at U_w = 30 m/s all the three familiar eddies are observable in the system. The new geometry has an effect on the pressure distribution along the substrate, as presented in Figure 9. For example, in case of N4, there are two local minimums with a local maximum in front of the blade. On the blade, as shown in Figure 10, there is also a local minimum in pressure which is the effect of the formation of the third eddy located close to that point. It is important to note that the new geometry alone does not succeed at completely removing the eddies from the system.

2. Dynamic Vortex-Free Coater

For cases N3 and N4 a further modification of the coating system is investigated. One of the applicator walls is designed to be a floting/moving surface. This application system has a moving inner surface which could be a roll or a contoured surface that slides over a supporting surface (Aidun, SN 137,957). Cases N3 and N4 cover the compuattional visualization of flow patterns and pressure in this system.

Table 4 shows the cases as the speed of the lower wall, U_b, is gradually increased from 1 m/s to 5 m/s, while the discharge is kept constant at q=5 l/s/m. In the following cases, U_b is chosen

to be the characteristic velocity, U. The effect of the moving surface is that the second elongated eddy gets shorter and the separation point on the applicator wall moves downstream. Figure 11 illustrates the flow pattern for these cases. In case of NB34 and NB35 a fourth eddy becomes more distinguishable, as shown in Figure 11 . Figure 12 and 13 present the pressure distribution for theses cases along the substrate and the blade, respectively.

Table 5 gives the parameters for the numerical runs where the fluid discharge is allowed to increase while the moving surface carries most of the liquid into the channel primarily by shear. Two cases are investigated with respect to the web velocity. Column 5 in Table 5 shows how much liquid is pumped into the system while column 6 gives the total flow rate entering the applicator. As a result of the combined effects from pumping and the motion of the applicator wall, the eddies vanish as shown in Figure 14 for machine speed, U_w=30m/s, and in Figure 17, for machine speed as high as U_w = 40 m/s. Figure 15 and 16 illustrate the pressure distribution along the substrate and the blade, respectfully, for U_w = 30m/s. Figure 18 and 19 present the pressure distributions for U_w = 40m/s. In both cases the pressure increases approximately 10-20% while the eddies completely disappear from the system. A more complete manuscript detailing the computational results is in preparation (Kovacs and Aidun, 1994).

4. Conclusion

At high speed and low flow rates, eddies cannot be completely avoided with the stationary vortex-free coating system. Three ways to suppress these eddies have been investigated.

The first one corresponds to the gradual increase of the fluid discharge per unit width entering

the applicator. This procedure, although very effective in removing the eddies, is not economical due to large pumping needs.

The second method employs a modified geometry which results in the downstream motion of the separation point.

The third method is based on designing a moving applicator wall. In this case the combined effects from pumping, converging geometry, and the shear induced by the moving surface combine to completely remove the eddies from the coating system. This is a true 'vortex-free' coater.

REFERENCES

1. Aidun, C.K., "Coating Device for Traveling Webs," patent applications SN 881,512, appn SN 849,530 (pending).

2. Aidun, C.K., "Flotation Coating Device for Traveling Webs," patent application SN 137,957, (approved/will be granted shortly).

3. Cody, C., and Aidun, C.K., "Elastohydrodyramic analysis of vortex-free coating systems", code under development, 1994.

4. Kovacs, A., and Aidun, C.K., "Computaitonal Analysis of a New Coating System," under preparation, 1994.

List of Figures:

List of Symbols:

$\mathbf{u}$ and u_i	fluid velocity
u,v,w	fluid velocity components
t	time
x_i	Cartesian coordinate
ρ	fluid density
f_i	component of the gravitational acceleration
p	pressure
p_a	ambient pressure
σ_{ij}	stress tensor
σ_n	normal component of the stress vector
σ_t	tangential component of the stress vector
τ_{ij}	deviatoric stress tensor
δ_{ij}	Kronecker delta
ε_{ij}	shear rate tensor
μ	dynamic viscosity
μ_∞	infinite shear rate viscosity (Carreau model)
μ_0	zero shear rate viscosity (Carreau model)
n	power in the Carreau model
K	time constant (Carreau model)
*	superscript denoting non-dimensional quantity
U	characteristic velocity scale
U_p	maximum velocity at the inlet if the inflow has a parabolic velocity distribution
L	characteristic length
L_{in}	width of the inflow channel
L_{gap}	width of the gap between the blade and the substrate
$Re=\mu/(\rho UL)$	Reynolds number
$Ca=\mu U/\gamma$	capillary number
$\mathbf{U}_{in}$	inflow velocity distribution
$\mathbf{U}_w$	substrate velocity
$\mathbf{U}_b$	applicator wall velocity
Γ	boundary of the domain of computation
η	height of the free surface
γ	surface tension coefficient
H	Gaussian mean curvature of the free surface
q	flowrate per unit width entering the applicator

	U_p	L_{in}	L_{gap}	$q = 2U_pL_{in}/3$	U_w	γ surf.tens	μ viscosity	ρ density	$Re = U_pL_{in}\rho/\mu$	$Ca = \mu U_p/\gamma$	COM-MENT ON THE RESULT
Run	m/s	m	m	l/s/m	m/s	kg/s^2	kg/(m s)	kg/m^3	-	-	
B1	1.00	0.0025	$50\ 10^{-6}$	1.667	1.0	0.05	1.00	1200	3.0	20.0	A
B2	1.50			2.500	2.5				4.5	30.0	A
B3	2.00			3.333	5.0				6.0	40.0	S
B4	2.50			4.166	10.0				7.5	50.0	S
B5	3.00			5.000	20.0				9.0	60.0	S
B6	3.00			5.000	30.0				9.0	60.0	S
B7	3.00			5.000	40.0				9.0	60.0	S

INPUT PARAMETERS FOR THE SIMULATION OF NEWTONIAN FLOW
(S = Flow separation, A = Attached flow)

TABLE 1.

	U_p	L_{in}	L_{gap}	$q = 2U_pL_{in}/3$	U_w	γ surf.tens	μ_∞ viscosity	μ_o viscosity	K	ρ density	n	COM-MENT on the result
Run	m/s	m	m	l/s/m	m/s	kg/s^2	kg/(m s)	kg/(m s)		kg/m^3		
C1	3.0	0.0025	$50\ 10^{-6}$	5.00	20.0	0.05	0.05	1.00	0.01	1200	0.65	S
C2					30.0							S
C3					40.0							S
C11	5.0	0.0025	$50\ 10^{-6}$	8.33	20.0	0.05	0.05	1.00	0.01	1200	0.65	S
C12	8.0			13.33								S
C13	12.0			20.0								S
C14	16.0			26.67								A
C15	20.0			33.33								A

INPUT PARAMETERS FOR THE SIMULATION OF NON-NEWTONIAN FLOW (Carreau model)
(S = Flow separation, A =Attached flow)

TABLE 2.

	U_p	L_{in}	L_{gap}	$q = 2U_pL_{in}/3$	U_w	γ surf.tens	μ_∞ viscosity	μ_0 viscosity	K	ρ density	n	COM-MENT ON THE RESULT
Run	m/s	m	m	l/s/m	m/s	kg/s^2	kg/(m s)	kg/(m s)		kg/m^3		
N1	3.0	0.0025	$50\ 10^{-6}$	5.0	10.0	0.05	0.05	1.00	0.01	1200	0.65	A
N2					20.0							S
N3					30.0							S
N4					40.0							S

INPUT PARAMETERS FOR THE SIMULATION OF NON-NEWTONIAN FLOW (Carreau model)
(S = Flow separation, A = Attached flow)

TABLE 3.

	U_b	L_{in}	L_{gap}	q	U_w	γ surf.tens	μ_∞ viscosity	μ_o viscosity	K	ρ density	n	COM-MENT ON THE RESULT
Run	m/s	m	m	l/s/m	m/s	kg/s^2	kg/(m s)	kg/(m s)		kg/m^3		
NB31	1.0	0.0025	$50\ 10^{-6}$	5.00	30.0	0.05	0.05	1.00	0.01	1200	0.65	S
NB32	2.0											S
NB33	3.0											S
NB34	4.0											S
NB35	5.0											S
NB41	1.0	0.0025	$50\ 10^{-6}$	5.00	40.0	0.05	0.05	1.00	0.01	1200	0.65	S
NB42	3.0											S
NB43	5.0											S

INPUT PARAMETERS FOR THE SIMULATION OF NON-NEWTONIAN FLOW (Carreau model)
(S = Flow separation)

TABLE 4.

	U_b	L_{in}	L_{gap}	q pumped	Σq	U_w	γ surf.tens	μ_∞ viscosity	μ_0 viscosity	K	ρ density	n	COM-MENT ON THE RESULT
Run	m/s	m	m	l/s/m	l/s/m	m/s	kg/s^2	kg/(m s)	kg/(m s)		kg/m^3		
NB51	5.0	0.0025	$50\ 10^{-6}$	0.0	6.25	30.0	0.05	0.05	1.00	0.01	1200	0.65	S
NB52	5.0			2.5	8.75								S
NB53	5.0			5.0	11.25								S
NB54	10.0			0.0	12.50								S
NB55	10.0			5.0	17.50								A
NB61	5.0	0.0025	$50\ 10^{-6}$	5.0	11.25	40.0	0.05	0.05	1.00	0.01	1200	0.65	S
NB62	10.0			5.0	17.50								A
NB63	15.0			5.0	23.75								A

INPUT PARAMETERS FOR THE SIMULATION OF NON-NEWTONIAN FLOW (Carreau model)
(S = Flow separation, A = Attached flow)

TABLE 5.

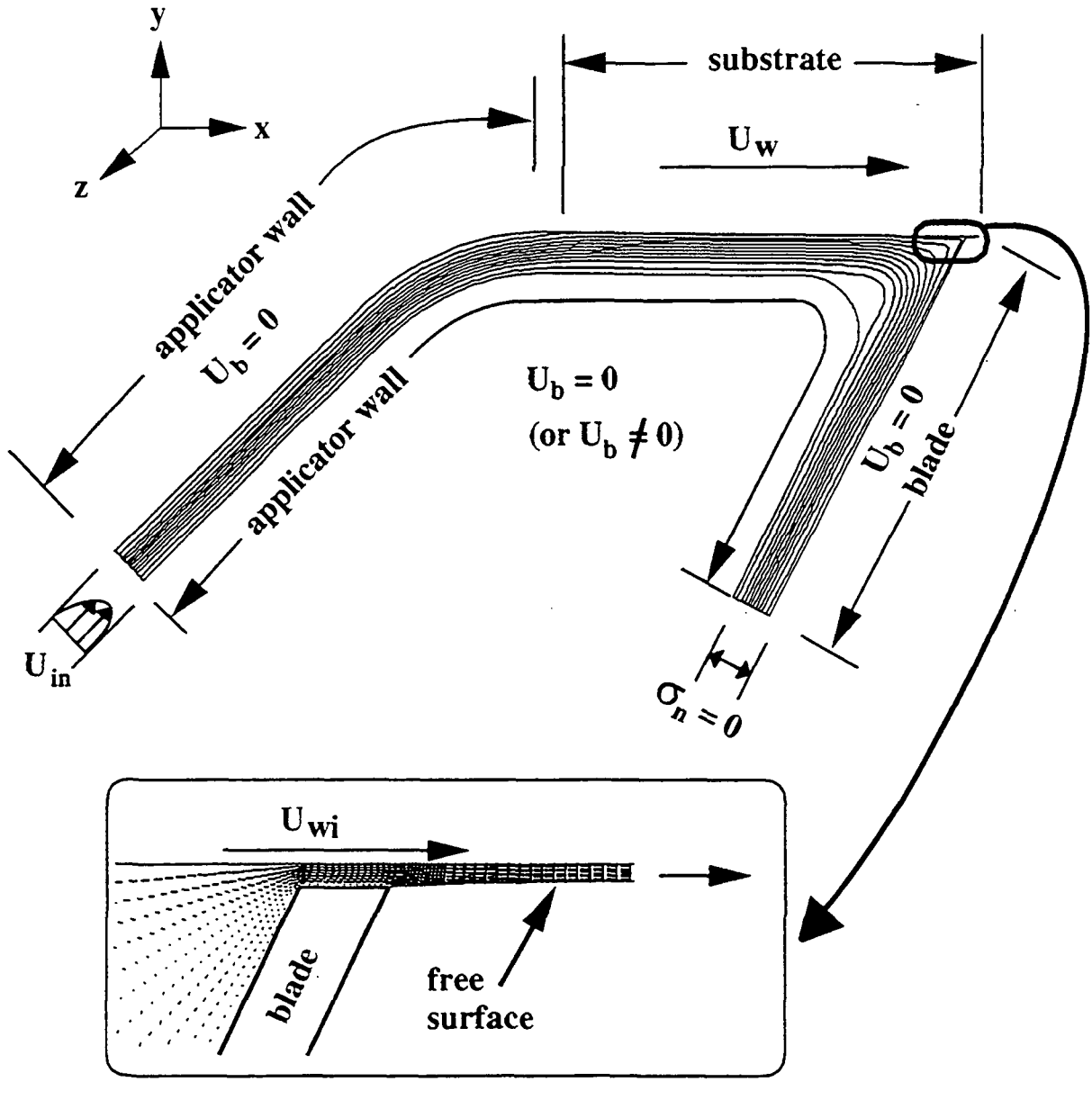
y
x
z
substrate
U_w
applicator wall
$U_b = 0$
applicator wall
$U_b = 0$
(or $U_b \neq 0$)
$U_b = 0$
blade
U_{in}
$\sigma_n = 0$
U_{wi}
blade
free
surface

Figure 1

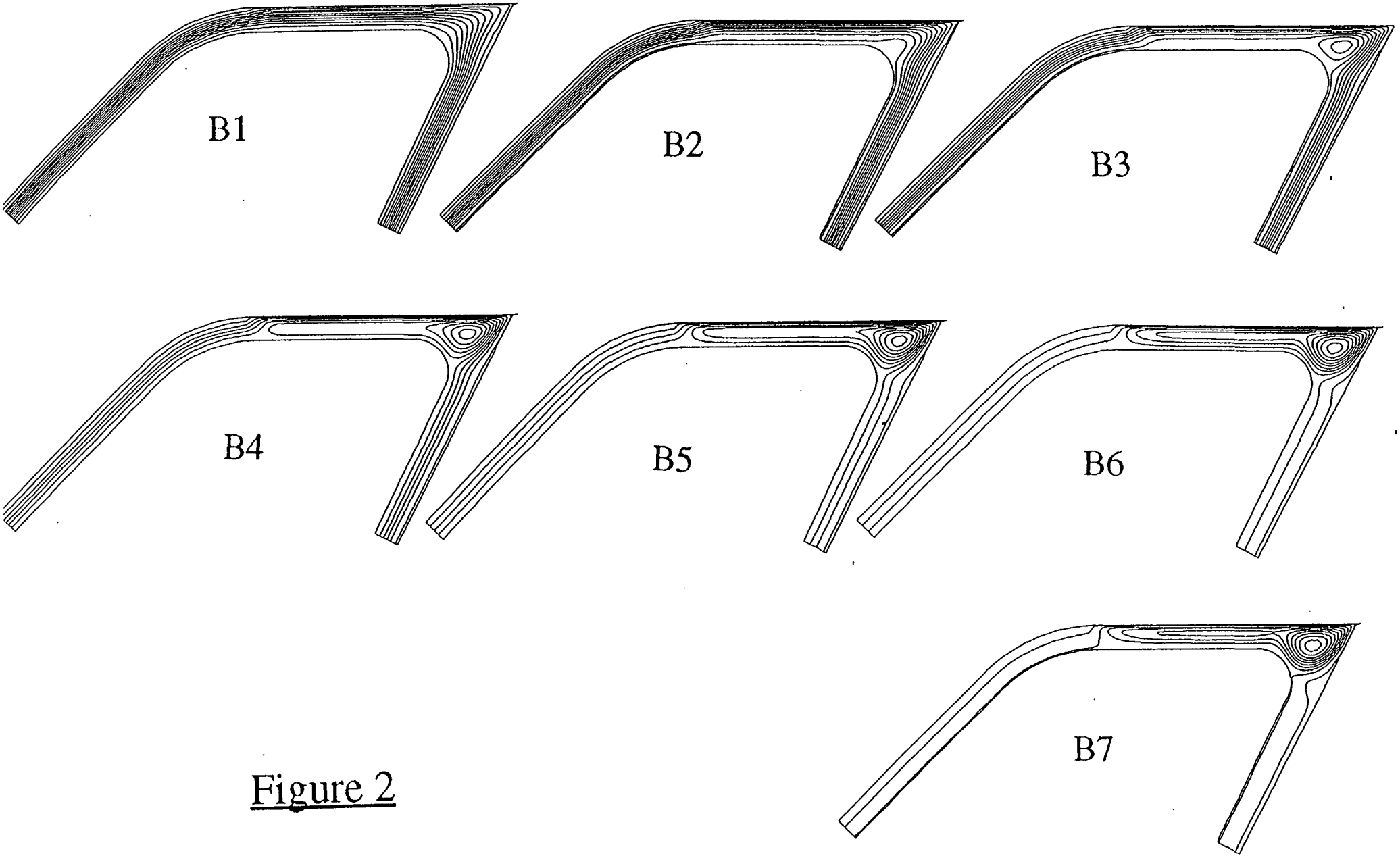

Figure 2

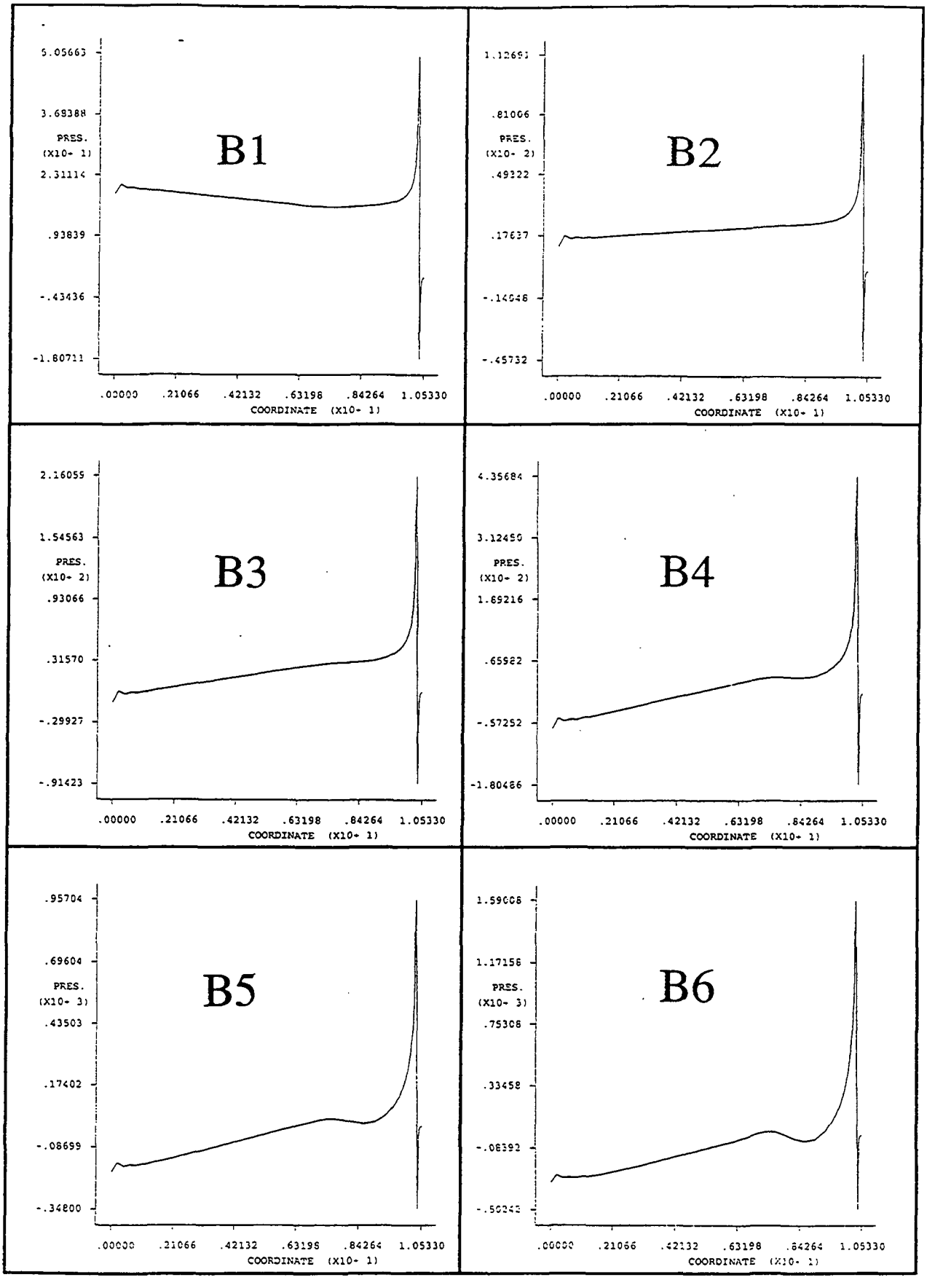
B1
5.05663
3.69388
PRES.
(X10- 1)
2.31114
.93839
-.43436
-1.80711
.00000 .21066 .42132 .63198 .84264 1.05330
COORDINATE (X10- 1)
B2
1.12693
.81006
PRES.
(X10- 2)
.49322
.17637
-.14048
-.45732
.00000 .21066 .42132 .63198 .84264 1.05330
COORDINATE (X10- 1)
B3
2.16059
1.54563
PRES.
(X10- 2)
.93066
.31570
-.29927
-.91423
.00000 .21066 .42132 .63198 .84264 1.05330
COORDINATE (X10- 1)
B4
4.35684
3.12450
PRES.
(X10- 2)
1.89216
.65982
-.57252
-1.80486
.00000 .21066 .42132 .63198 .84264 1.05330
COORDINATE (X10- 1)
B5
.95704
.69604
PRES.
(X10- 3)
.43503
.17402
-.08699
-.34800
.00000 .21066 .42132 .63198 .84264 1.05330
COORDINATE (X10- 1)
B6
1.59008
1.17156
PRES.
(X10- 3)
.75306
.33458
-.08392
.00000 .21066 .42132 .63198 .84264 1.05330
COORDINATE (X10- 1)

Figure 3

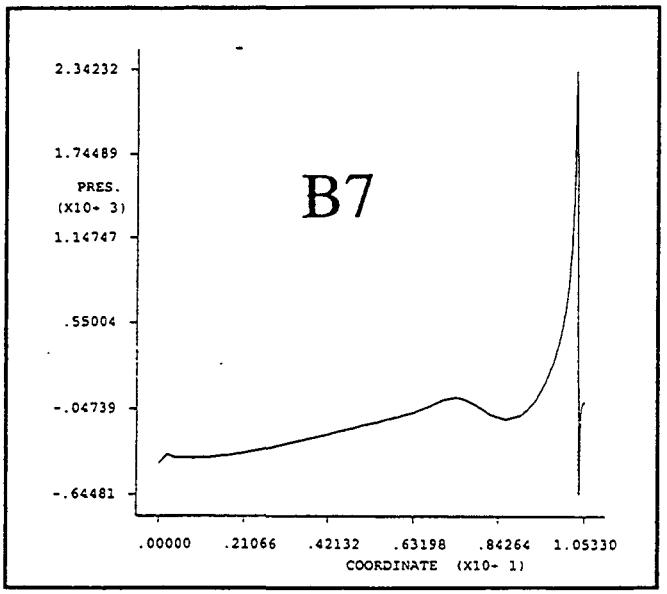
B7
2.34232
1.74489
PRES.
(X10- 3)
1.14747
.55004
-.04739
-.64481
.00000
.21066
.42132
.63198
.84264
1.05330
COORDINATE (X10- 1)

Figure 3

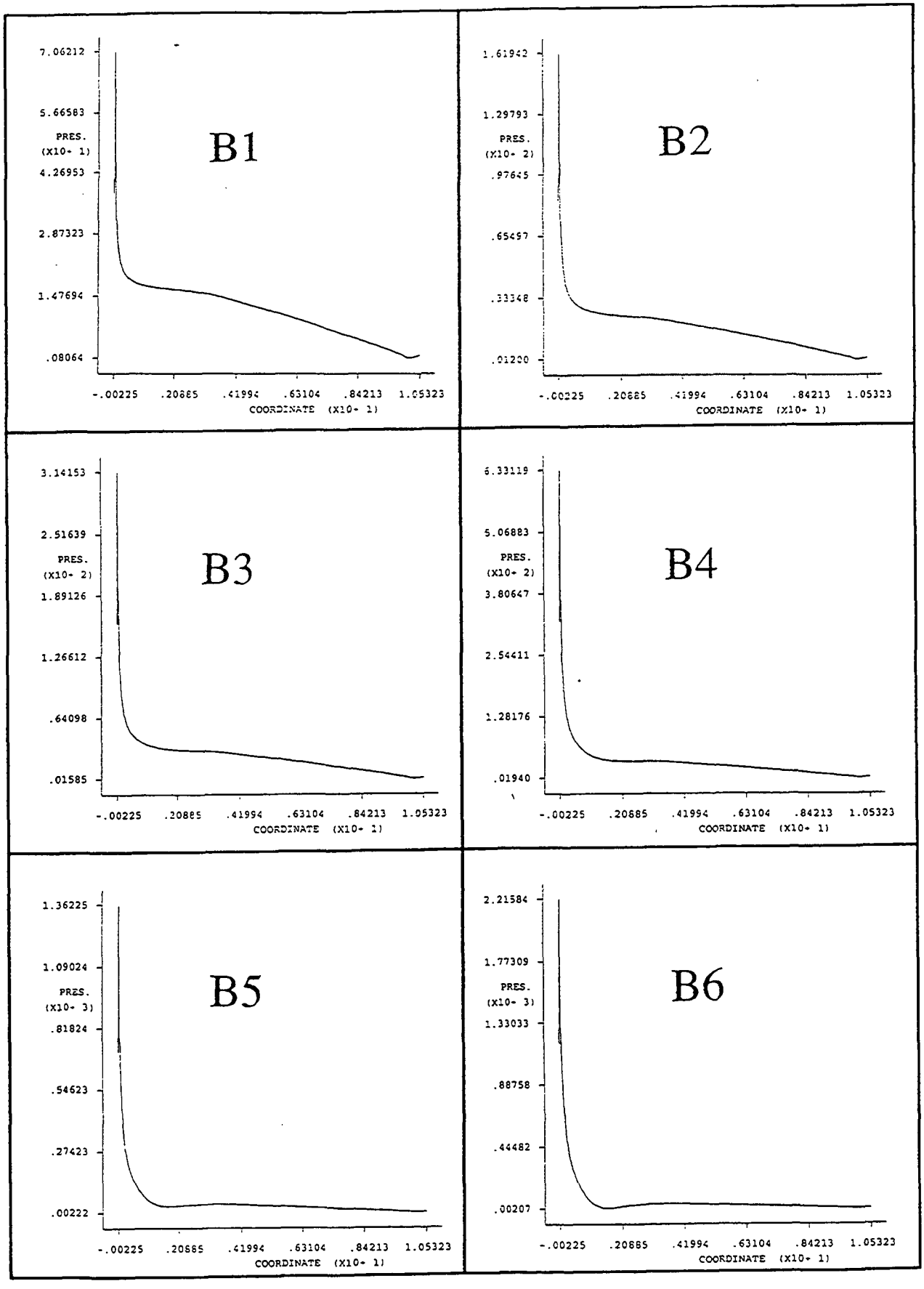
B1
7.06212
5.66583
PRES.
(X10- 1)
4.26953
2.87323
1.47694
.08064
-.00225
.20885
.41994
.63104
.84213
1.05323
COORDINATE (X10- 1)
B2
1.61942
1.29793
PRES.
(X10- 2)
.97645
.65497
.33348
.01200
-.00225
.20885
.41994
.63104
.84213
1.05323
COORDINATE (X10- 1)
B3
3.14153
2.51639
PRES.
(X10- 2)
1.89126
1.26612
.64098
.01585
-.00225
.20885
.41994
.63104
.84213
1.05323
COORDINATE (X10- 1)
B4
6.33119
5.06883
PRES.
(X10- 2)
3.80647
2.54411
1.28176
.01940
-.00225
.20885
.41994
.63104
.84213
1.05323
COORDINATE (X10- 1)
B5
1.36225
1.09024
PRES.
(X10- 3)
.81824
.54623
.27423
.00222
-.00225
.20885
.41994
.63104
.84213
1.05323
COORDINATE (X10- 1)
B6
2.21584
1.77309
PRES.
(X10- 3)
1.33033
.88758
.44482
.00207
-.00225
.20885
.41994
.63104
.84213
1.05323
COORDINATE (X10- 1)

Figure 4

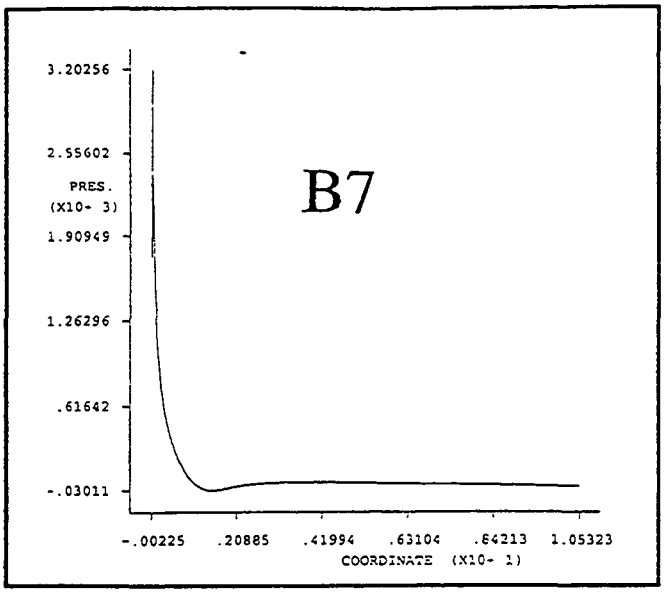
B7
3.20256
2.55602
PRES.
(X10- 3)
1.90949
1.26296
.61642
-.03011
-.00225
.20885
.41994
.63104
.64213
1.05323
COORDINATE (X10- 1)

Figure 4

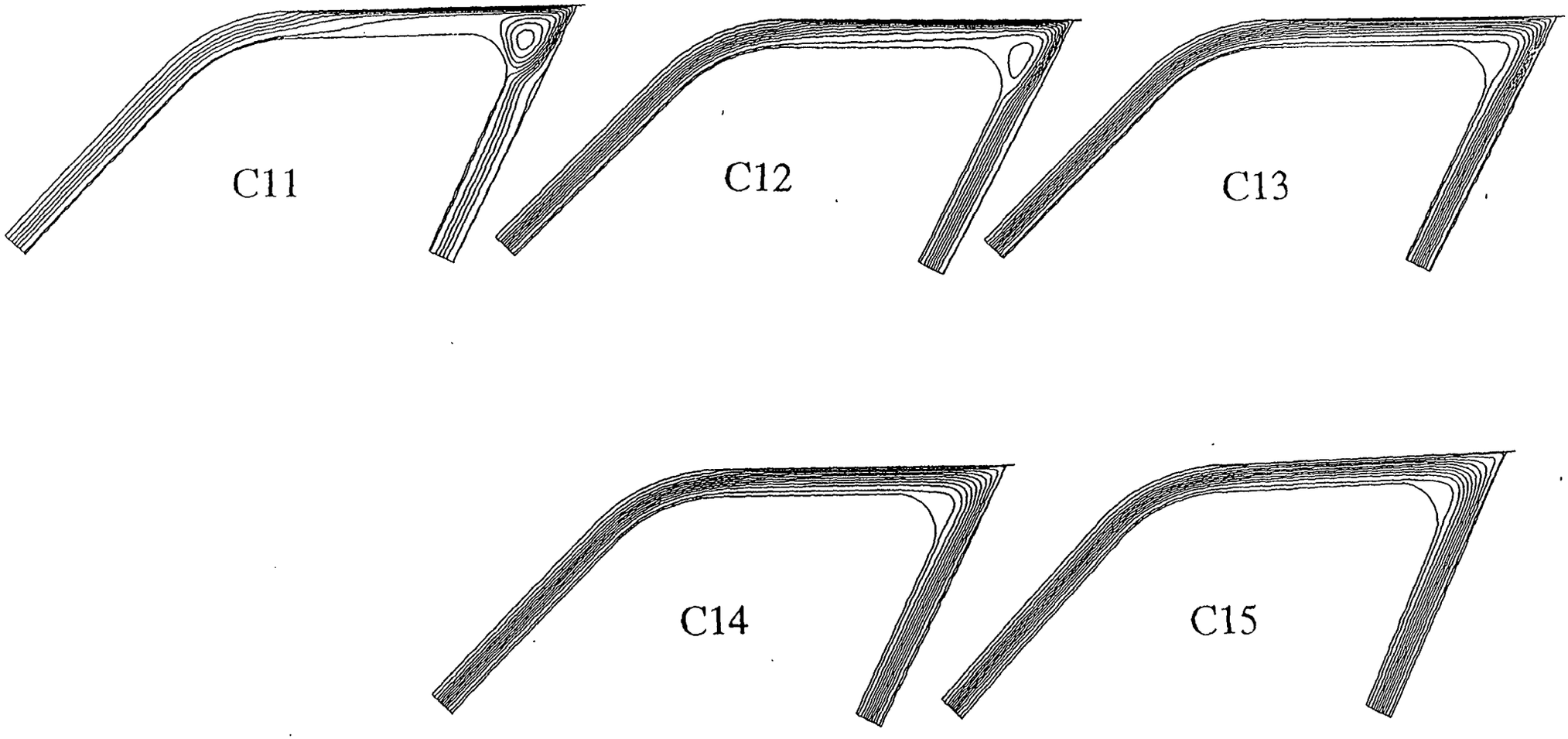

Figure 5

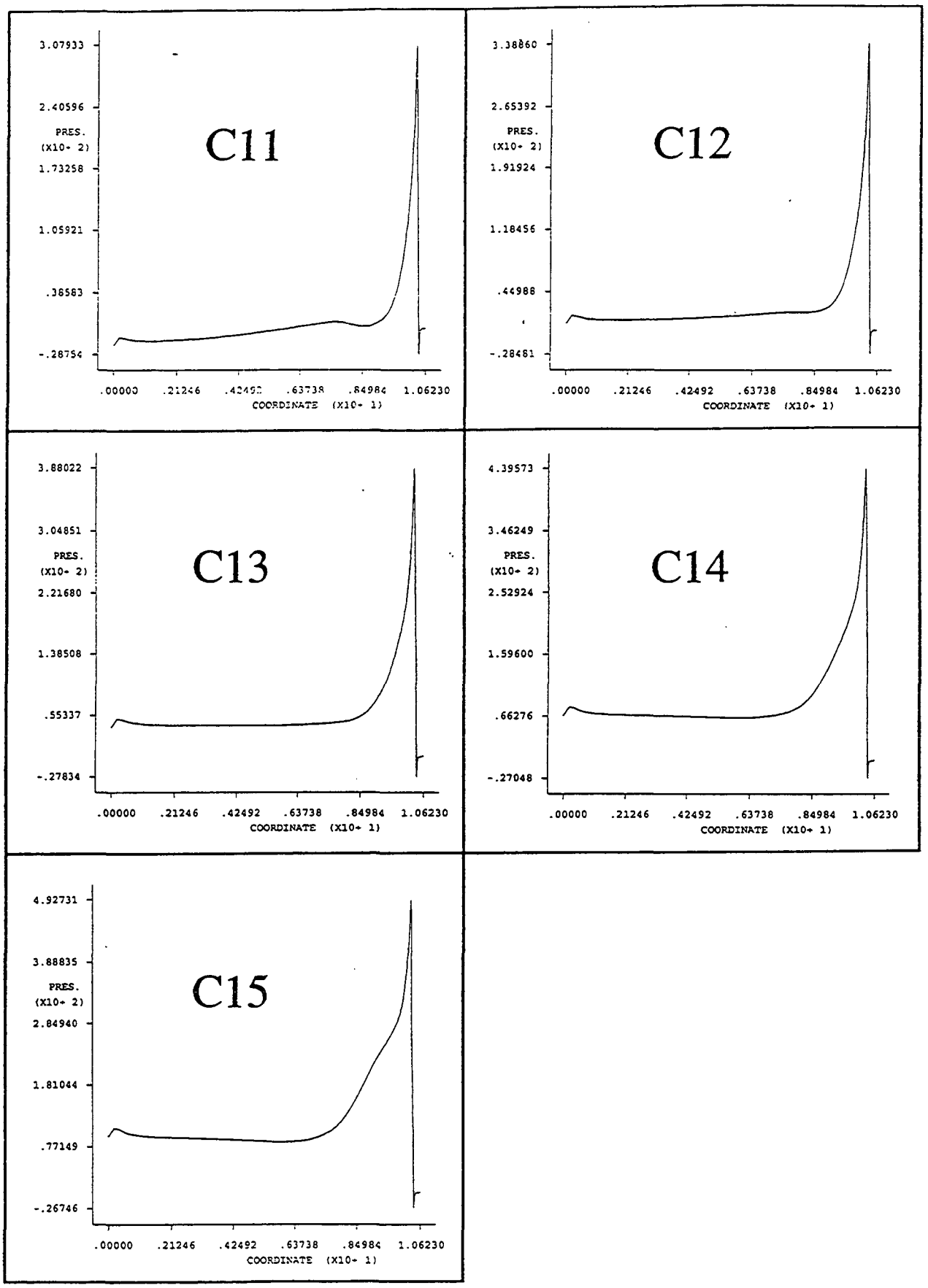
C11
3.07933
2.40596
PRES.
(X10+ 2)
1.73258
1.05921
.38583
-.28754
.00000 .21246 .42492 .63738 .84984 1.06230
COORDINATE (X10+ 1)
C12
3.38860
2.65392
PRES.
(X10+ 2)
1.91924
1.18456
.44988
-.28481
.00000 .21246 .42492 .63738 .84984 1.06230
COORDINATE (X10+ 1)
C13
3.88022
3.04851
PRES.
(X10+ 2)
2.21680
1.38508
.55337
-.27834
.00000 .21246 .42492 .63738 .84984 1.06230
COORDINATE (X10+ 1)
C14
4.39573
3.46249
PRES.
(X10+ 2)
2.52924
1.59600
.66276
-.27048
.00000 .21246 .42492 .63738 .84984 1.06230
COORDINATE (X10+ 1)
C15
4.92731
3.88835
PRES.
(X10+ 2)
2.84940
1.81044
.77149
-.26746
.00000 .21246 .42492 .63738 .84984 1.06230
COORDINATE (X10+ 1)

Figure 6

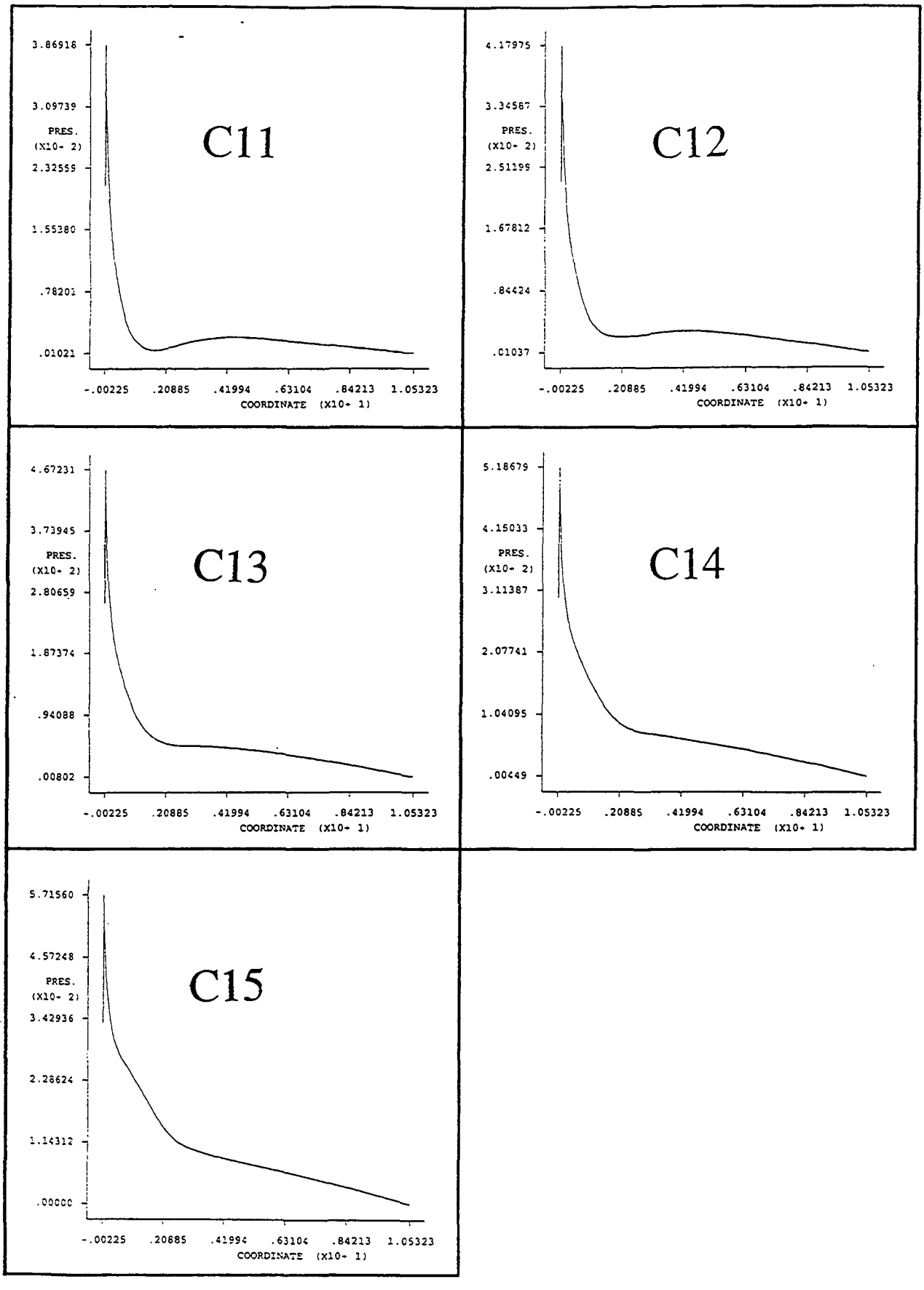
C11
3.86916
3.09739
PRES.
(X10- 2)
2.32555
1.55380
.78201
.01021
-.00225
.20885
.41994
.63104
.84213
1.05323
COORDINATE (X10- 1)
C12
4.17975
3.34567
PRES.
(X10- 2)
2.51199
1.67812
.84424
.01037
-.00225
.20885
.41994
.63104
.84213
1.05323
COORDINATE (X10- 1)
C13
4.67231
3.73945
PRES.
(X10- 2)
2.80659
1.87374
.94088
.00802
-.00225
.20885
.41994
.63104
.84213
1.05323
COORDINATE (X10- 1)
C14
5.18679
4.15033
PRES.
(X10- 2)
3.11387
2.07741
1.04095
.00449
-.00225
.20885
.41994
.63104
.84213
1.05323
COORDINATE (X10- 1)
C15
5.71560
4.57248
PRES.
(X10- 2)
3.42936
2.28624
1.14312
.00000
-.00225
.20885
.41994
.63104
.84213
1.05323
COORDINATE (X10- 1)

Figure 7

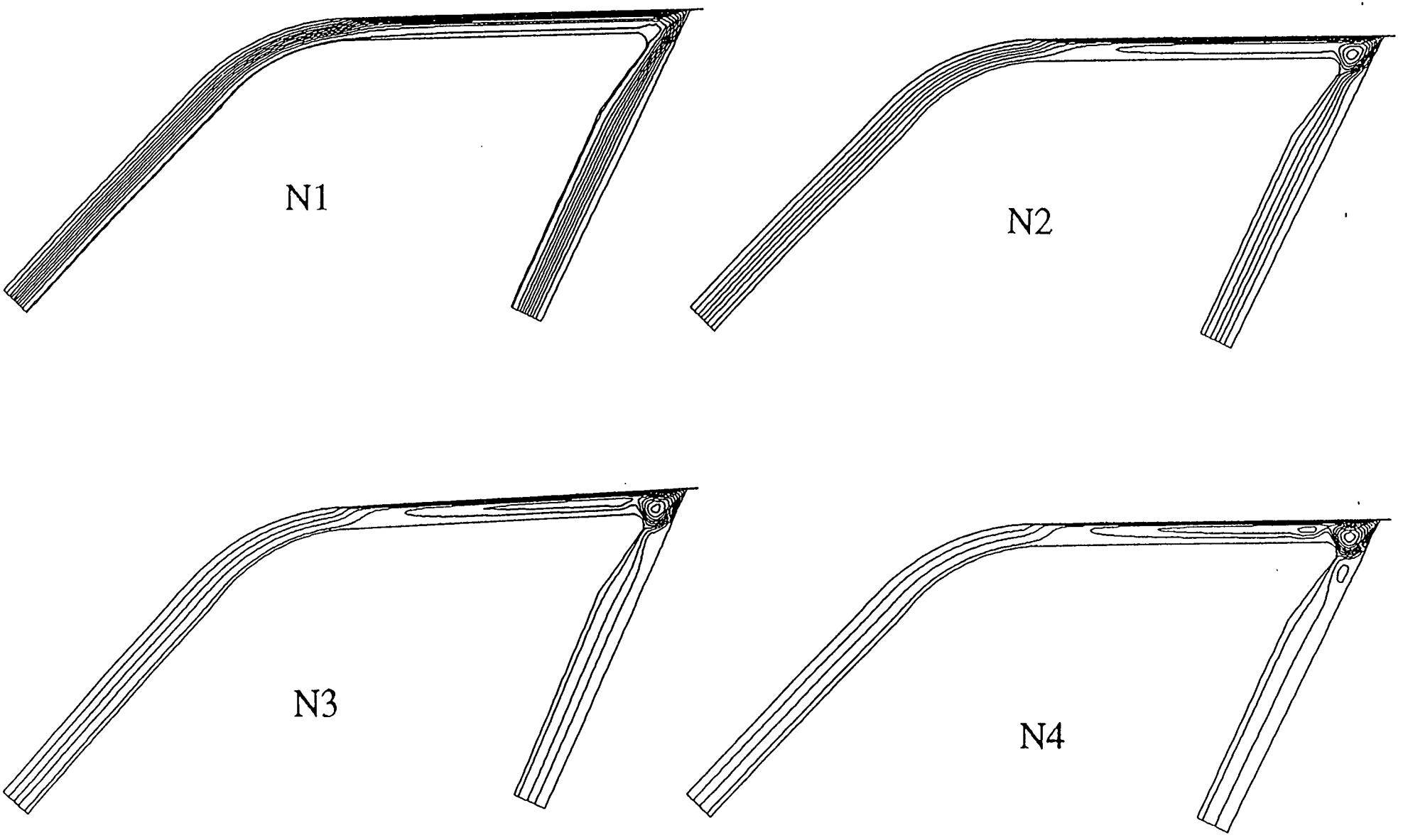

Figure 8

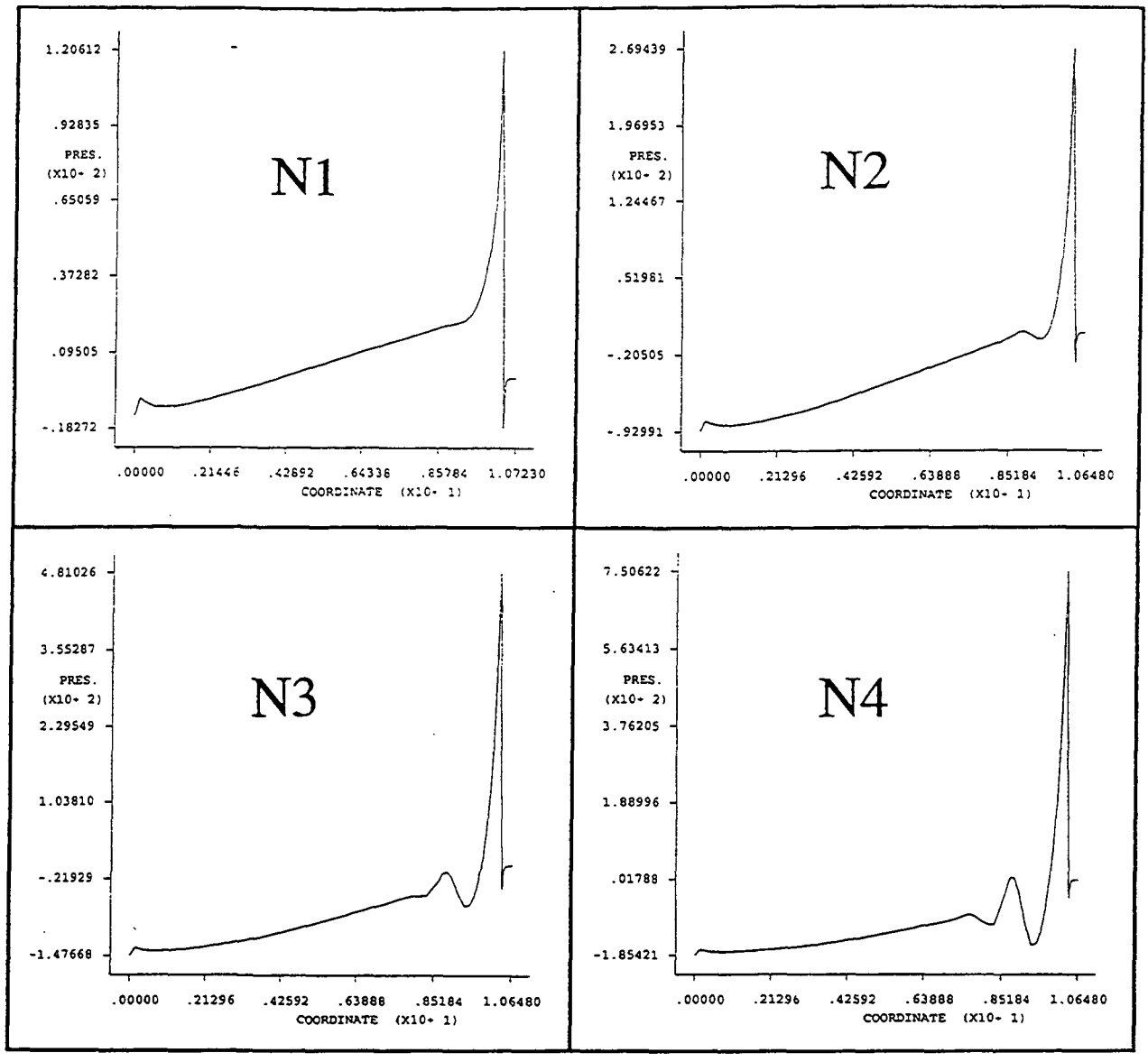
N1
1.20612
.92835
PRES.
(X10- 2)
.65059
.37282
.09505
-.18272
.00000
.21446
.42892
.64338
.85784
1.07230
COORDINATE (X10- 1)
N2
2.69439
1.96953
PRES.
(X10- 2)
1.24467
.51981
-.20505
-.92991
.00000
.21296
.42592
.63888
.85184
1.06480
COORDINATE (X10- 1)
N3
4.81026
3.55287
PRES.
(X10- 2)
2.29549
1.03810
-.21929
-1.47668
.00000
.21296
.42592
.63888
.85184
1.06480
COORDINATE (X10- 1)
N4
7.50622
5.63413
PRES.
(X10- 2)
3.76205
1.88996
.01788
-1.85421
.00000
.21296
.42592
.63888
.85184
1.06480
COORDINATE (X10- 1)

Figure 9

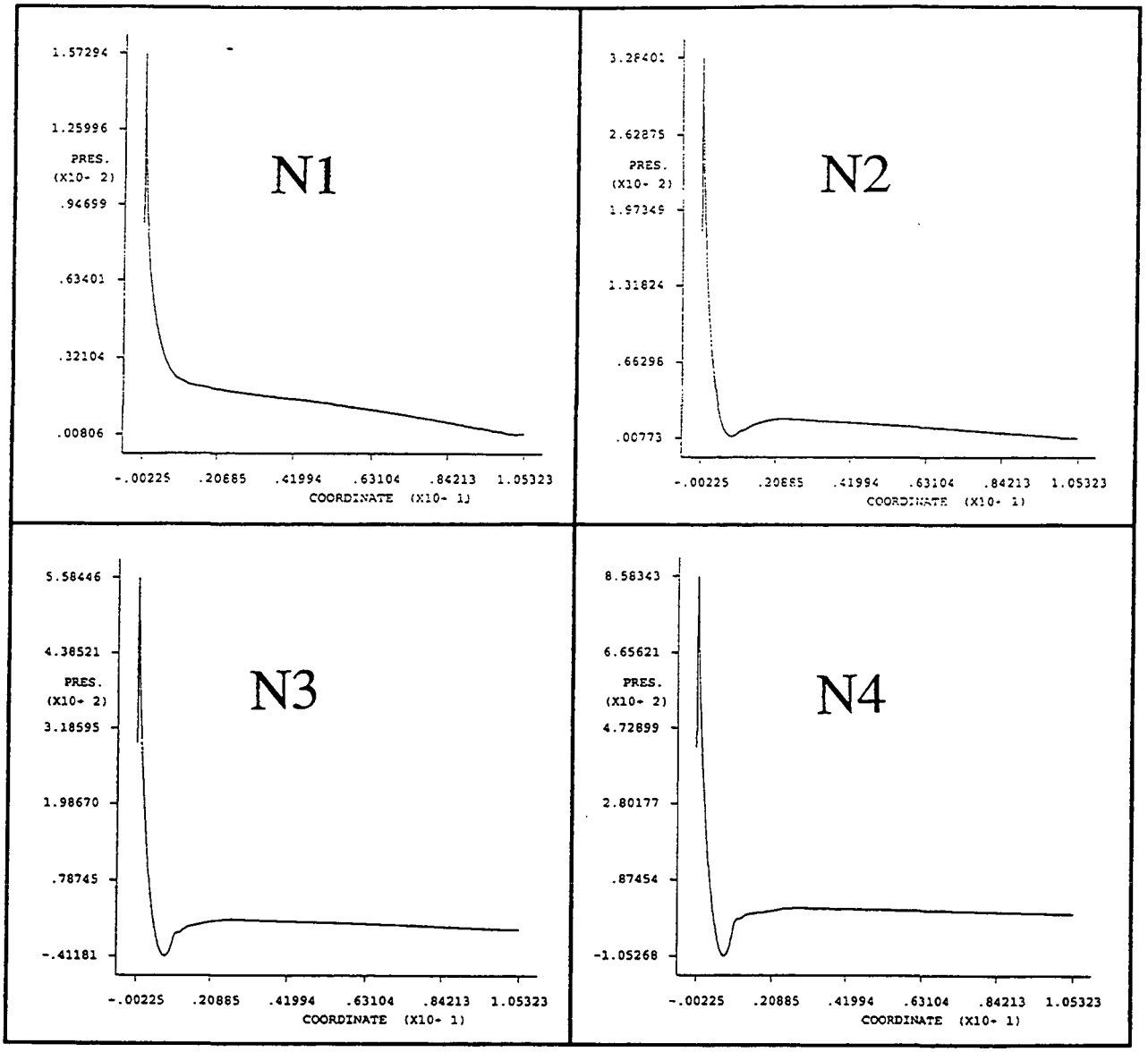
N1
1.57294
1.25996
PRES.
(X10- 2)
.94699
.63401
.32104
.00806
-.00225
.20885
.41994
.63104
.84213
1.05323
COORDINATE (X10- 1)
N2
3.28401
2.62875
PRES.
(X10- 2)
1.97349
1.31824
.66296
.00773
-.00225
.20885
.41994
.63104
.84213
1.05323
COORDINATE (X10- 1)
N3
5.58446
4.38521
PRES.
(X10- 2)
3.18595
1.98670
.78745
-.41181
-.00225
.20885
.41994
.63104
.84213
1.05323
COORDINATE (X10- 1)
N4
8.58343
6.65621
PRES.
(X10- 2)
4.72899
2.80177
.87454
-1.05268
-.00225
.20885
.41994
.63104
.84213
1.05323
COORDINATE (X10- 1)

Figure 10

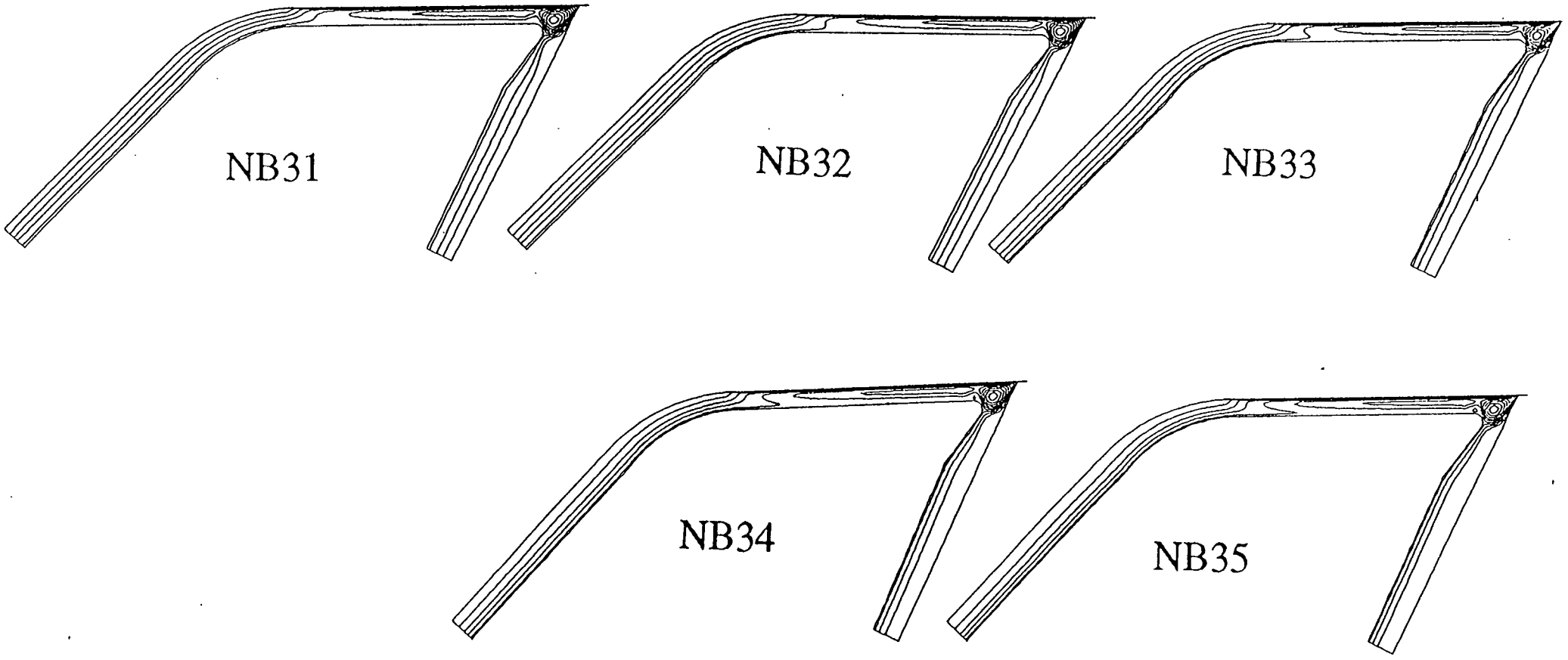

Figure 11

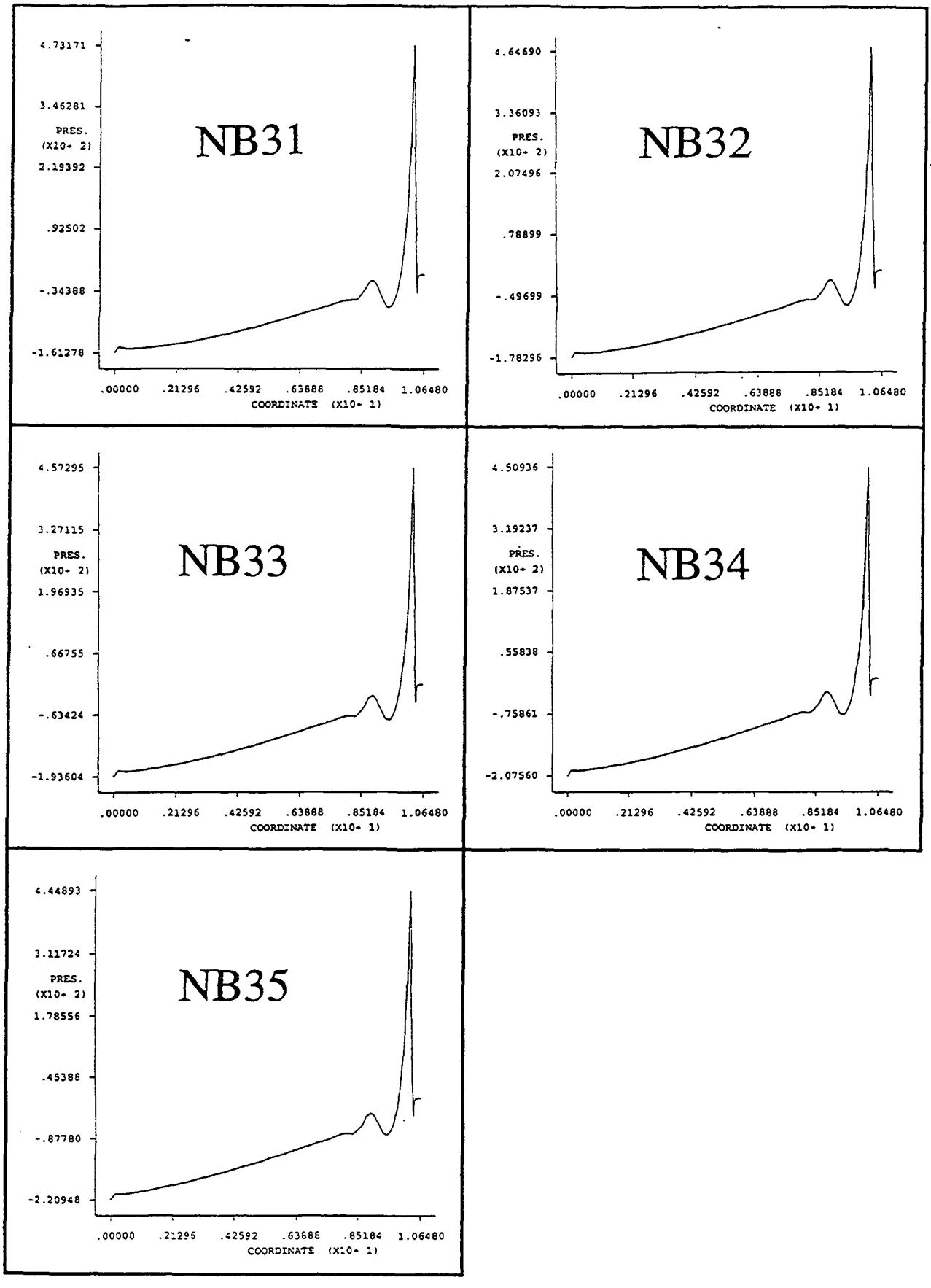
NB31
4.73171
3.46281
PRES.
(X10+ 2)
2.19392
.92502
-.34388
-1.61278
.00000 .21296 .42592 .63888 .85184 1.06480
COORDINATE (X10+ 1)
NB32
4.64690
3.36093
PRES.
(X10+ 2)
2.07496
.78899
-.49699
-1.78296
.00000 .21296 .42592 .63888 .85184 1.06480
COORDINATE (X10+ 1)
NB33
4.57295
3.27115
PRES.
(X10+ 2)
1.96935
.66755
-.63424
-1.93604
.00000 .21296 .42592 .63888 .85184 1.06480
COORDINATE (X10+ 1)
NB34
4.50936
3.19237
PRES.
(X10+ 2)
1.87537
.55838
-.75861
-2.07560
.00000 .21296 .42592 .63888 .85184 1.06480
COORDINATE (X10+ 1)
NB35
4.44893
3.11724
PRES.
(X10+ 2)
1.78556
.45388
-.87780
-2.20948
.00000 .21296 .42592 .63888 .85184 1.06480
COORDINATE (X10+ 1)

Figure 12

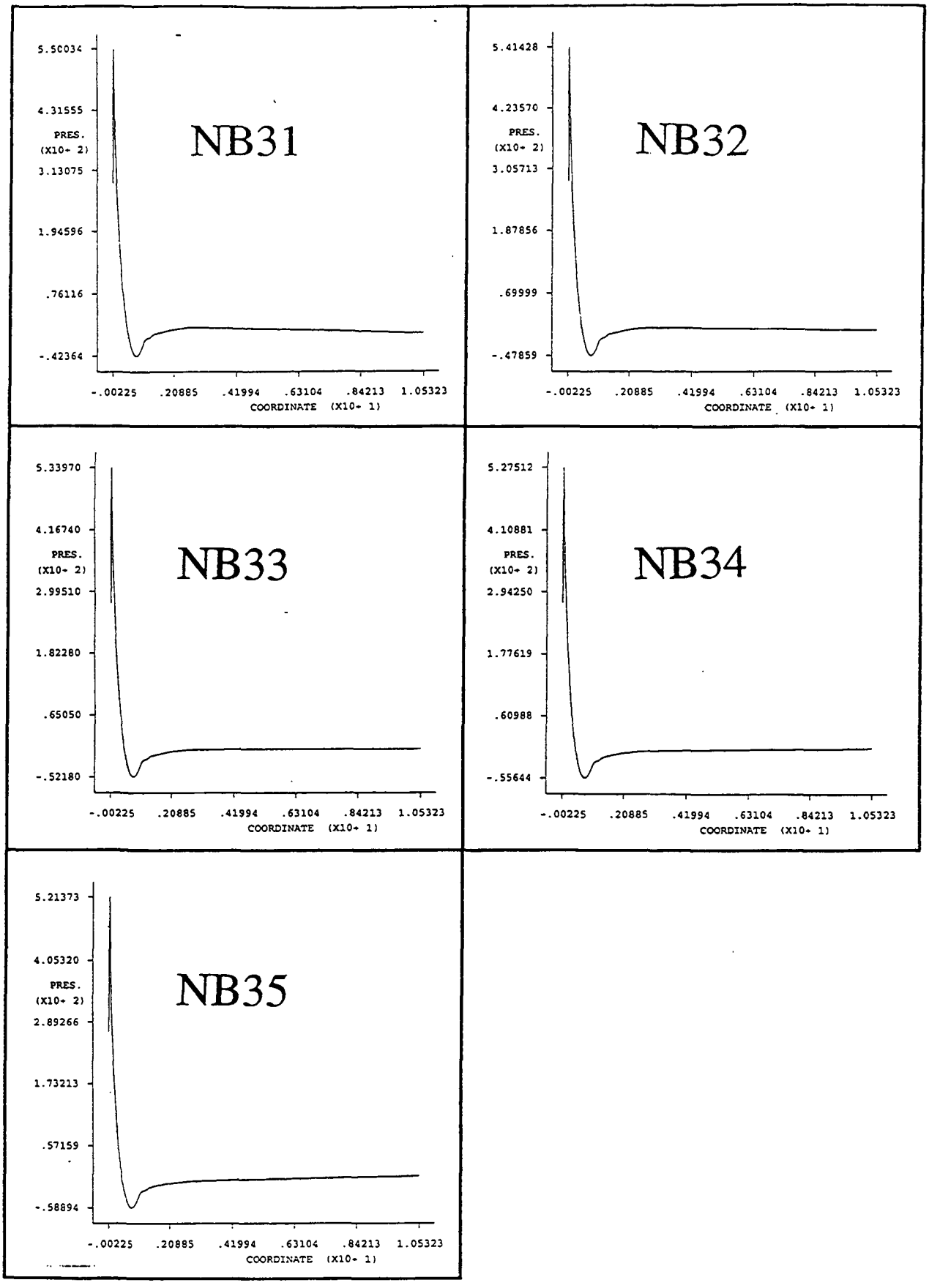
NB31
5.50034
4.31555
PRES.
(X10+ 2)
3.13075
1.94596
.76116
-.42364
-.00225
.20885
.41994
.63104
.84213
1.05323
COORDINATE (X10+ 1)
NB32
5.41428
4.23570
PRES.
(X10+ 2)
3.05713
1.87856
.69999
-.47859
-.00225
.20885
.41994
.63104
.84213
1.05323
COORDINATE (X10+ 1)
NB33
5.33970
4.16740
PRES.
(X10+ 2)
2.99510
1.82280
.65050
-.52180
-.00225
.20885
.41994
.63104
.84213
1.05323
COORDINATE (X10+ 1)
NB34
5.27512
4.10881
PRES.
(X10+ 2)
2.94250
1.77619
.60988
-.55644
-.00225
.20885
.41994
.63104
.84213
1.05323
COORDINATE (X10+ 1)
NB35
5.21373
4.05320
PRES.
(X10+ 2)
2.89266
1.73213
.57159
-.58894
-.00225
.20885
.41994
.63104
.84213
1.05323
COORDINATE (X10+ 1)

Figure 13

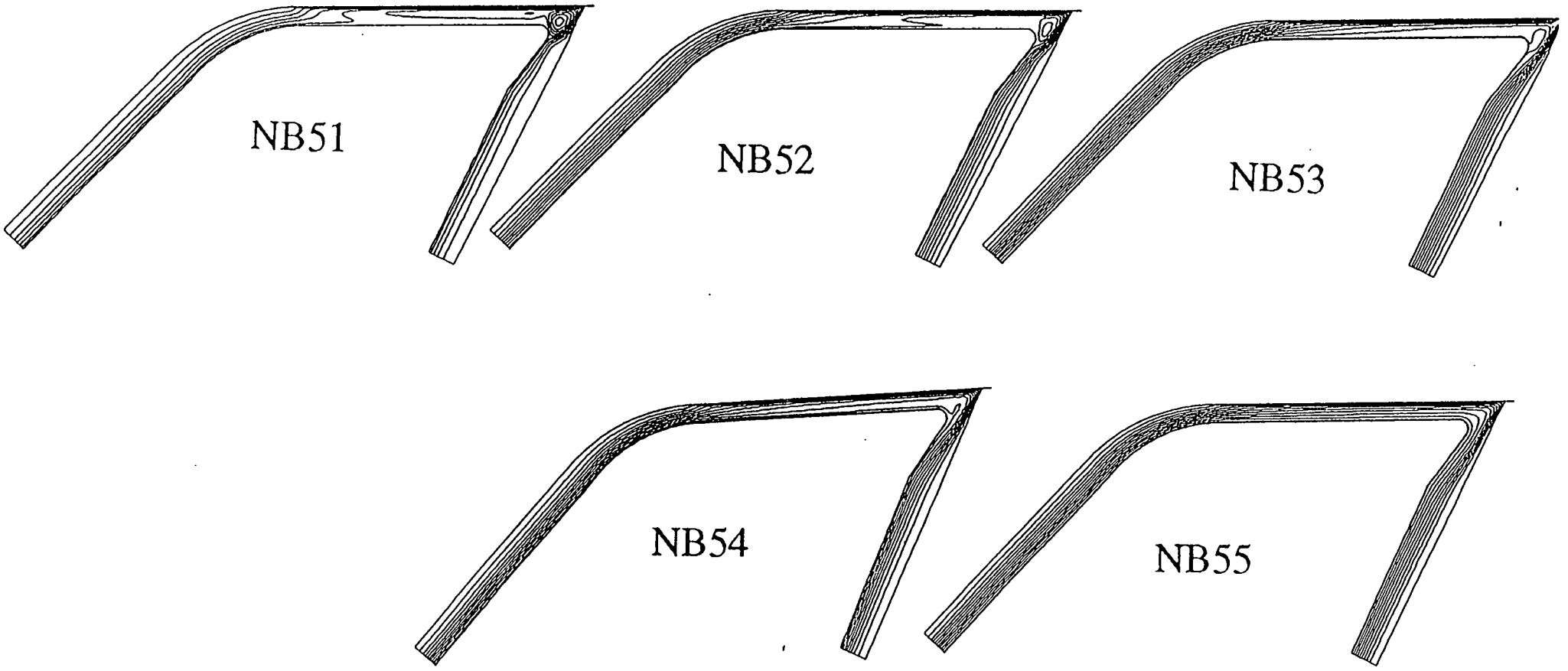

Figure 14

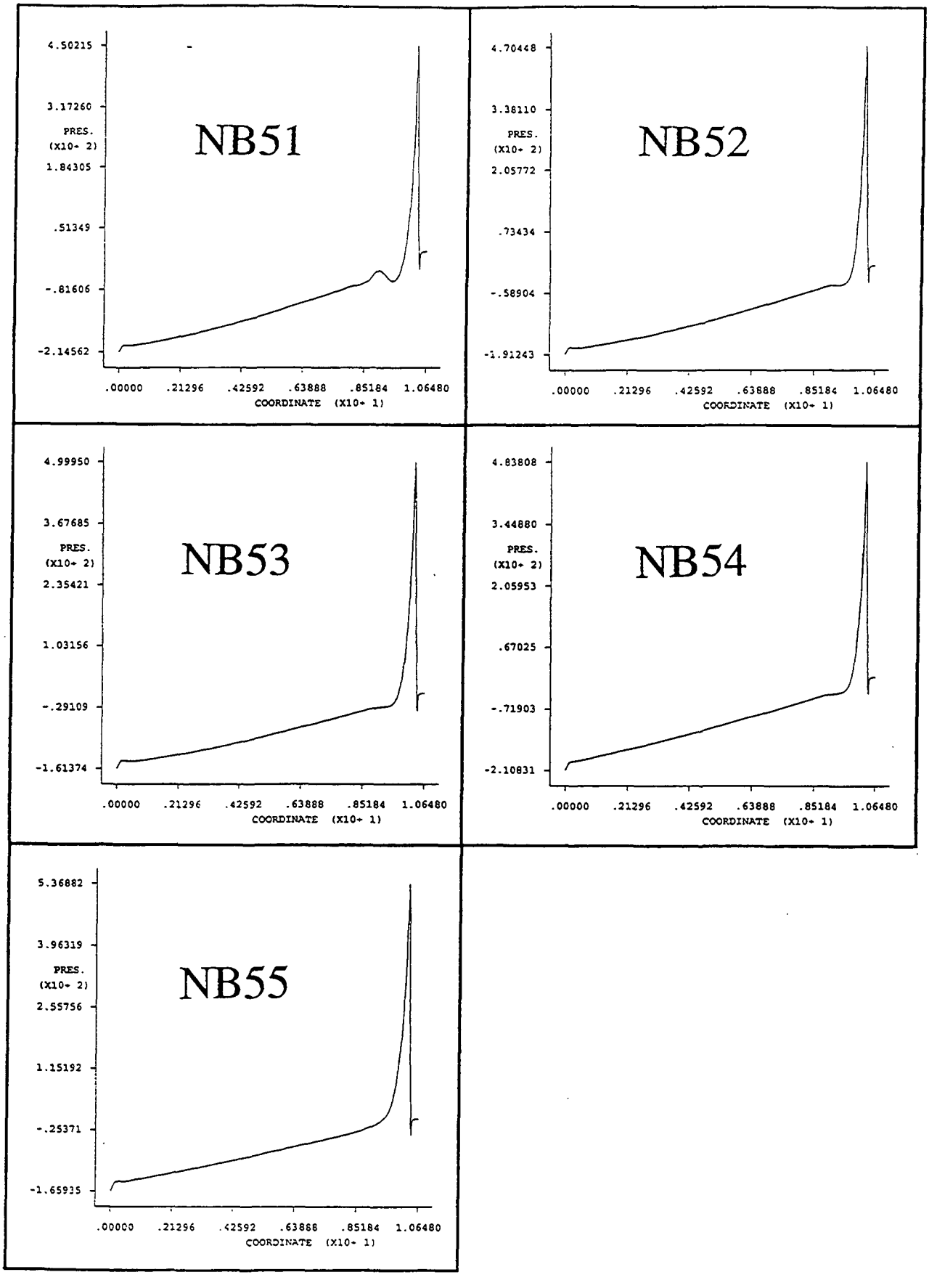
NB51
4.50215
3.17260
PRES.
(X10+ 2)
1.84305
.51349
-.81606
-2.14562
.00000 .21296 .42592 .63888 .85184 1.06480
COORDINATE (X10+ 1)
NB52
4.70448
3.38110
PRES.
(X10+ 2)
2.05772
.73434
-.58904
-1.91243
.00000 .21296 .42592 .63888 .85184 1.06480
COORDINATE (X10+ 1)
NB53
4.99950
3.67685
PRES.
(X10+ 2)
2.35421
1.03156
-.29109
-1.61374
.00000 .21296 .42592 .63888 .85184 1.06480
COORDINATE (X10+ 1)
NB54
4.83808
3.44880
PRES.
(X10+ 2)
2.05953
.67025
-.71903
-2.10831
.00000 .21296 .42592 .63888 .85184 1.06480
COORDINATE (X10+ 1)
NB55
5.36882
3.96319
PRES.
(X10+ 2)
2.55756
1.15192
-.25371
-1.65935
.00000 .21296 .42592 .63888 .85184 1.06480
COORDINATE (X10+ 1)

Figure 15

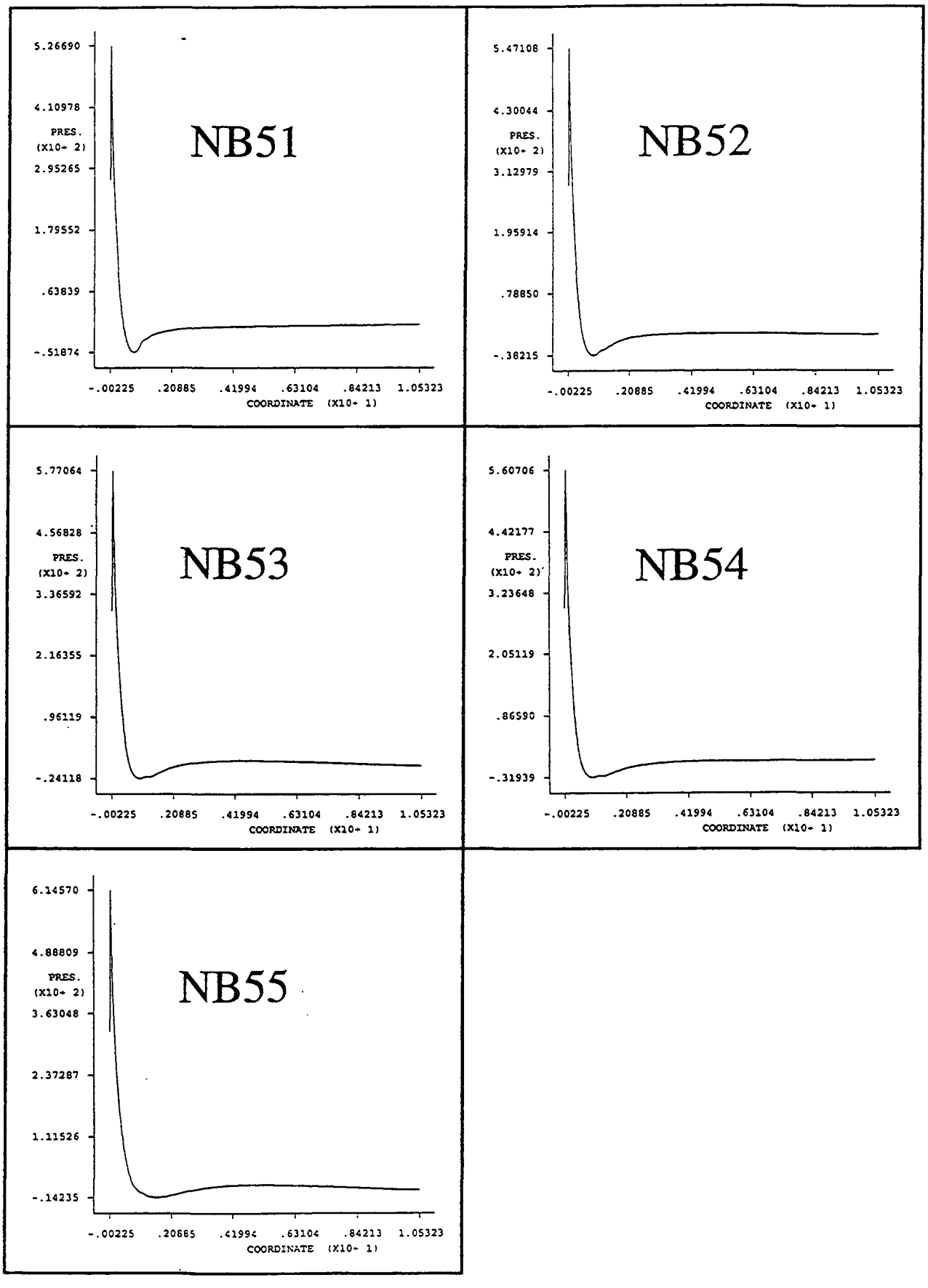
NB51
5.26690
4.10978
PRES.
(X10- 2)
2.95265
1.79552
.63839
-.51874
-.00225
.20885
.41994
.63104
.84213
1.05323
COORDINATE (X10- 1)
NB52
5.47108
4.30044
PRES.
(X10- 2)
3.12979
1.95914
.78850
-.38215
-.00225
.20885
.41994
.63104
.84213
1.05323
COORDINATE (X10- 1)
NB53
5.77064
4.56828
PRES.
(X10- 2)
3.36592
2.16355
.96119
-.24118
-.00225
.20885
.41994
.63104
.84213
1.05323
COORDINATE (X10- 1)
NB54
5.60706
4.42177
PRES.
(X10- 2)
3.23648
2.05119
.86590
-.31939
-.00225
.20885
.41994
.63104
.84213
1.05323
COORDINATE (X10- 1)
NB55
6.14570
4.88809
PRES.
(X10- 2)
3.63048
2.37287
1.11526
-.14235
-.00225
.20885
.41994
.63104
.84213
1.05323
COORDINATE (X10- 1)

Figure 16

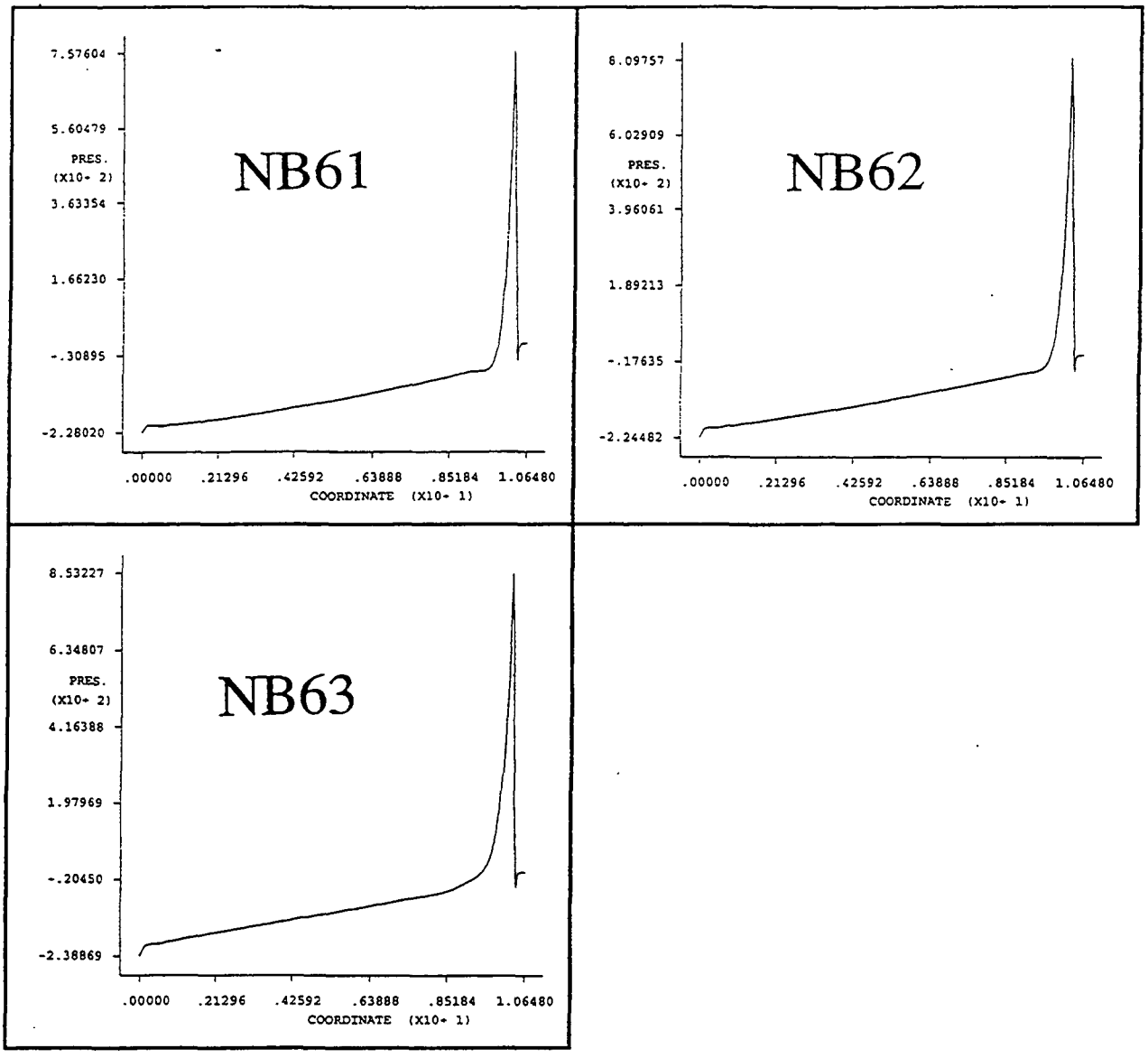
NB61
7.57604
5.60479
PRES.
(X10+ 2)
3.63354
1.66230
-.30895
-2.28020
.00000
.21296
.42592
.63888
.85184
1.06480
COORDINATE (X10+ 1)
NB62
6.09757
6.02909
PRES.
(X10+ 2)
3.96061
1.89213
-.17635
-2.24482
.00000
.21296
.42592
.63888
.85184
1.06480
COORDINATE (X10+ 1)
NB63
8.53227
6.34807
PRES.
(X10+ 2)
4.16388
1.97969
-.20450
-2.38869
.00000
.21296
.42592
.63888
.85184
1.06480
COORDINATE (X10+ 1)

Figure 18

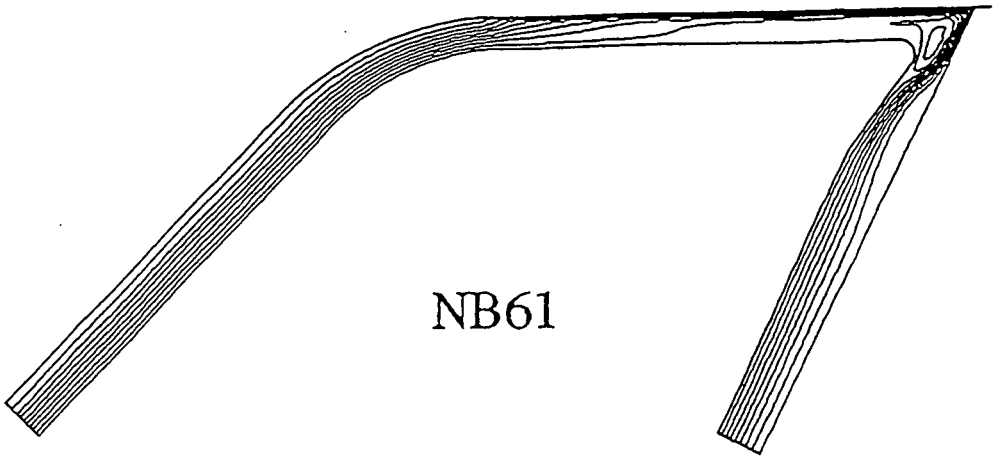

NB61

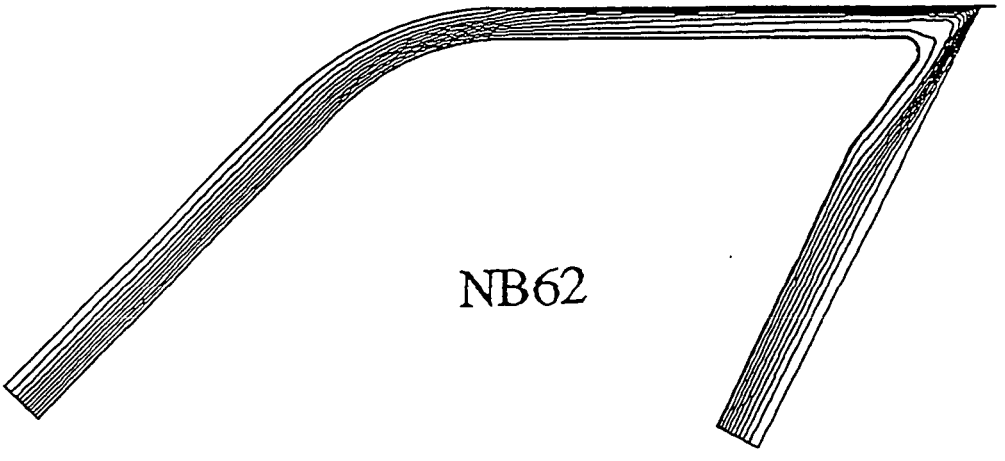

NB62

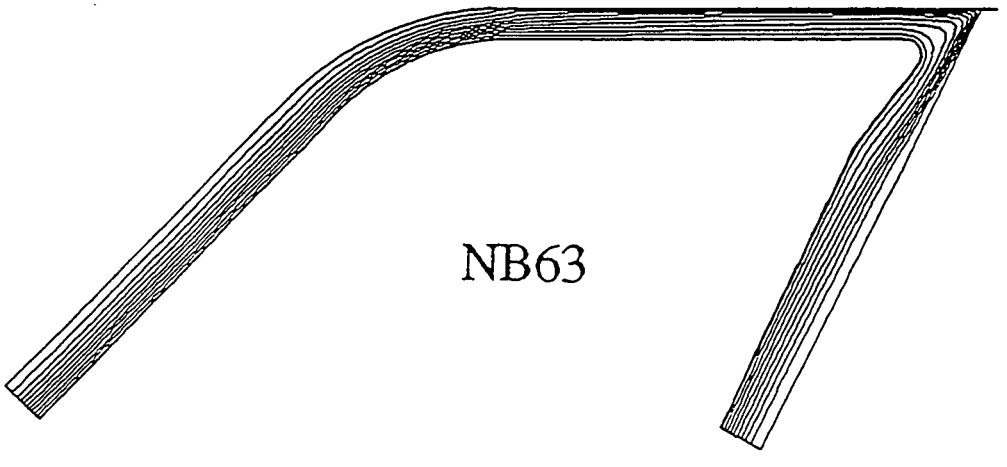

NB63

Figure 17

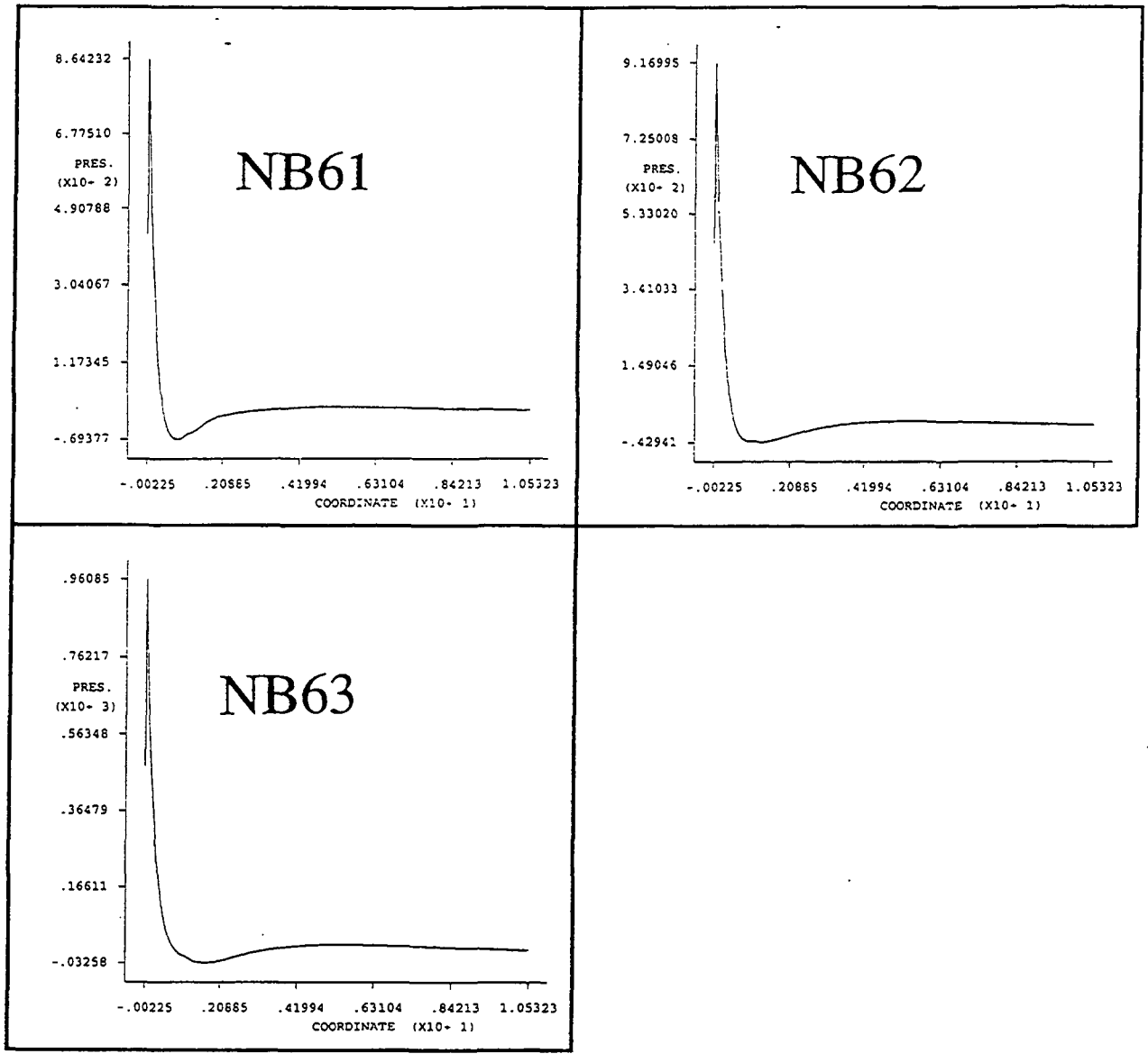
NB61
8.64232
6.77510
PRES.
(X10- 2)
4.90788
3.04067
1.17345
-.69377
-.00225
.20885
.41994
.63104
.84213
1.05323
COORDINATE (X10- 1)
NB62
9.16995
7.25008
PRES.
(X10- 2)
5.33020
3.41033
1.49046
-.42941
-.00225
.20885
.41994
.63104
.84213
1.05323
COORDINATE (X10- 1)
NB63
.96085
.76217
PRES.
(X10- 3)
.56348
.36479
.16611
-.03258
-.00225
.20885
.41994
.63104
.84213
1.05323
COORDINATE (X10- 1)

Figure 19

FUNDAMENTALS OF WATER REMOVAL PROCESSES

STATUS REPORT

FOR

PROJECT 3480

March 22, 1994

Institute of Paper Science and Technology
Atlanta, Georgia

Project Title:	FUNDAMENTALS OF WATER REMOVAL
Project Staff:	Jeff Lindsay
Budget (FY 92-93):	$60,000
Reporting Period:	FY 92-93
Division:	Engineering and Paper Materials
Project No.:	3480

SUMMARY

In the last period, we have worked on gaining a better understanding of fluid transport in paper pores. Measurement methods for relative porosity (the fraction of the pore space open to fluid flow) have been extended to account for the effects of dispersion and diffusion during the dye injection procedure. We have also developed some fundamental insights into the nature of inertial effects during high velocity fluid flow through fibrous media. Although laminar or Darcian flow probably dominates in many pressing operations, inertial effects can still play a role and can be especially important in other processes such as through drying.

I. RELATIVE POROSITY IN PAPER

INTRODUCTION

In the Project 3480 PAC Report for Spring of 1993, the concept of relative porosity was presented with theoretical and experimental analysis. Relative porosity is defined as the fraction of the pore space in a medium that is open to flow. For example, a relative porosity value of 30% indicates that 70% of the water in a saturated sheet of paper is trapped in dead-end pores or micropores or physically or chemically bound to fibers. In the presence of a hydraulic pressure gradient, only about 30% of the pore volume would participate in fluid flow.

Relative porosity is relevant to problems of infiltration or penetration, as in sizing, coating, and printing. Relative porosity is especially important when two phases are involved, as when gas displaces liquid, for it governs the speed of the phase boundary. In other words, the penetrating phase can only move through the open, interconnected pores. An example is displacement dewatering, in which a gas is used to displace liquid water from a web. The amount of water removal possible will be affected by the amount of water in pores open to flow. If the effective porosity of this pore space is small, the penetrating fluid boundary may advance rapidly, yet the amount of penetrating fluid will be small. In two-phase flows, however, capillary effects can cause one phase to obstruct the flow of the other phase, further reducing the effective flow porosity open to each phase.

Past Experimental Work

In the Spring 1993 PAC Report, we examined a variety of methods for estimating how much water is associated with the fibers (e.g., immobilized as water of swelling) and discussed the implications of these methods for the concept of relative porosity. Specific volume from permeability measurements was offered as a useful method for estimating the extrafiber pore space in a fibrous mat. The extrafiber pore space was hypothesized to be the greatest possible volume open for flow in a consolidated paper mat.

We further reported a new experimental method for determining relative porosity. This technique employs the radial injection of a dyed fluid into a saturated disk. The paper is restrained between two smooth, uniformly pressed platens, which seal the surfaces of the sheet and allow flow to occur only in the radial direction. As the dye spreads into the sheet, it flows through pores open to flow. By comparing the volume occupied by the injected dye in the sheet with the volume of dye actually injected, we can determine the relative porosity (details of the calculation are given below). This can be done for both saturated sheets and initially dry sheets, although dry sheets

pose the risk of air bubbles hindering fluid penetration and decreasing the measured relative porosity.

Our apparatus is a modification of the IPST lateral permeability device, which has been previously described (1). In order to observe the growth of a dyed region during in-plane fluid injection, we replaced a metal platen in the permeability apparatus with a device to allow optical access to the compressed sheet. The platen replacement is a large cube of transparent, rigid plastic which will transmit force from the Carver press assembly to the paper (see Figure 1). A metallic mirror oriented at 45° from horizontal was cast into a plastic cube, as shown in Figure 2. The use of a mirror to observe in-plane fluid flow was inspired by the work of Adams et al. (2-5) at TRI. The mirror allows a viewer or a camera standing in front of the cube to observe the paper while it is under compression between the plastic cube and the lower platen. The growth of a dyed zone, formed by injection of colored water through the lower platen, can be viewed during a run. Normally, only the final boundary of the dyed region is noted after a given volume of fluid has been injected.

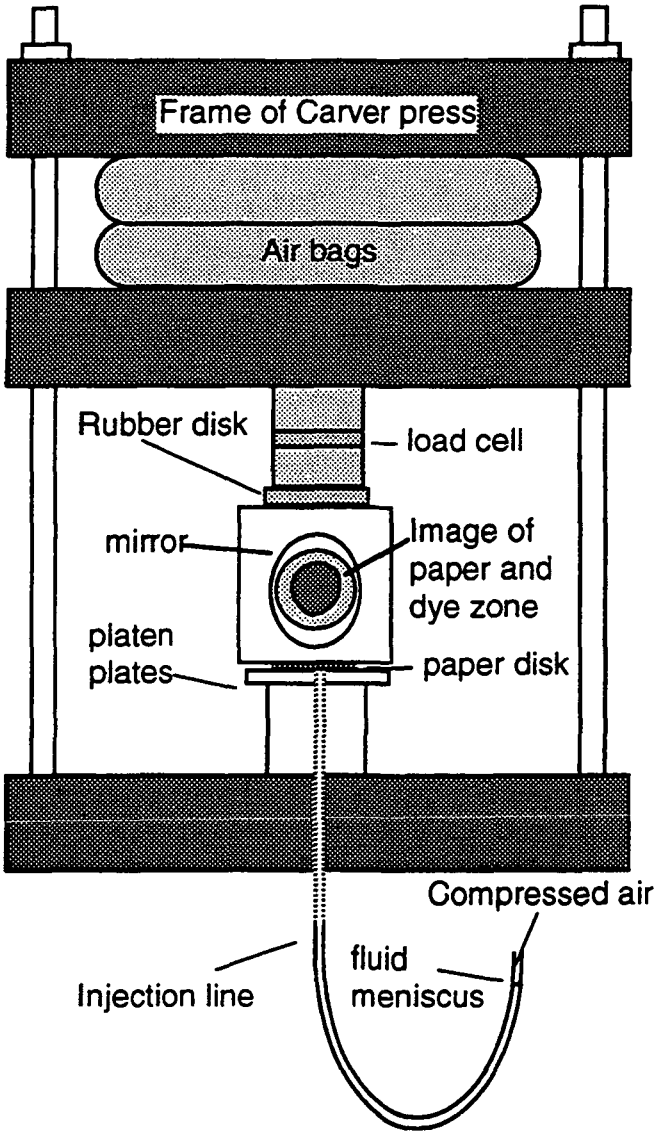

Figure 1. Modified lateral flow apparatus for dye injection tests.

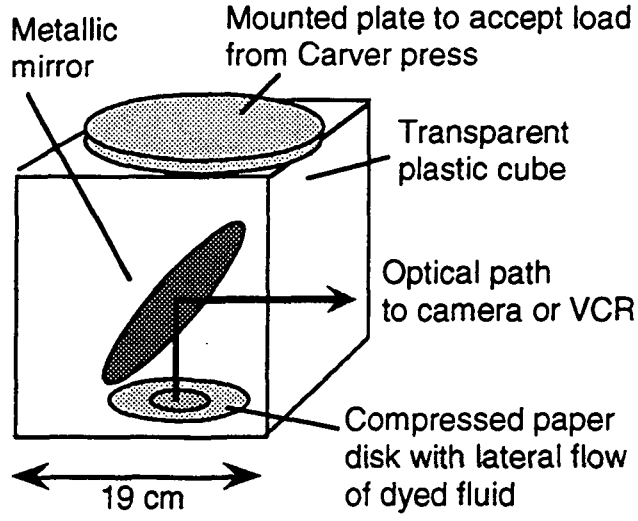

Figure 2. Plastic block with mirror for optical access to a compressed sheet.

The idea of our method is simple: inject fluid into paper, and compare the volume of fluid injected to the volume of the dyed region (based on thickness and dyed area) multiplied by sheet porosity. Sheet porosity is determined from sheet thickness under compression and basis weight:

$$\varepsilon = 1 - \frac{BW}{\rho_c L}, \qquad (1)$$

where BW is the sheet basis weight, ρ_c is the matrix density (e.g., the density of pure cellulose in filler-free sheets), and L is the sheet thickness. The area of the dyed zone can be measured after injection, or if the sheet has been marked with measured lines, the dyed area can be determined at various intervals during dye injection by viewing the dye boundary through the plastic cube.

Thickness is determined from three LVDT sensors distributed around the lower platen. LVDT rods protrude from the lower surface of the plastic block. The signal from the sensors responds monotonically to the position of the rods in the sensor. The thickness readings from the three sensors are averaged to give the sheet thickness.

In sheets that were initially dry, saturation was performed under vacuum to reduce the presence of air bubbles in the sheet. We placed a dry sample on a support stand in a desiccator jar

containing a layer of water at the bottom. The lid was placed on the jar and vacuum applied to deaerate the sheet. The jar was then bumped to knock the sample off its support, causing the sheet to fall into the water. After water infiltrated the pores of the sample, the vacuum was released.

The dye used in most of this study is Versatint Purple II (Milliken Chemical, Inman, S.C.), a fugitive water-soluble dye that does not absorb significantly onto cellulose. It was selected for its nonreactivity with paper fibers. We also conducted a number of tests using blue dextran 2000 (Pharmacia Fine Chemicals, Uppsala, Sweden), a strongly colored water-soluble polysaccharide that does not absorb onto paper. The high-molecular weight (ca. $2x10^6$), highly-branched polymer is too large to pass through micropores in the paper, but can flow through interfiber pores.

Diffusion, Dispersion, and Other Problems

We assume that the dyed fluid directly displaces clear water in the pores open to flow. There are several mechanisms which challenge this assumption. First, diffusion will mix some of the dye with water in dead-end pores or micropores. This process will dilute the dye, but should have little effect on the observed motion of the dye boundary. Diffusion of dye in the flow direction may also occur, but generally will be much slower than the flow and can be neglected.

More importantly, dispersion of the dye in the flow direction will occur, inflating the size of the dyed boundary and deflating our estimates of relative porosity. Dispersion is a convective mixing process that arises because of velocity profiles in individual pores and because of the complex branching and intertwining of flow paths in a porous medium. In problems of miscible displacement in porous media, dispersion effects will blur an initially sharp concentration gradient as it advances. Dispersion in the flow direction (radially outward) will inflate the apparent growth of the dyed region (thus deflating our estimate of effective porosity).

In the past period, we have explored several aspects of dispersion with analytical and numerical solutions to the relevant but simplified flow problems. We will see that molecular diffusion reduces the degree of dispersion. While dispersion does introduce some error into our results, we will show that it need not be serious if the molecular diffusions of the dye are sufficiently large or if the initial dye concentration is properly adjusted. In any case, dispersion will tend to decrease the measured relative porosity, so our reported values may generally be taken as lower bounds.

Another issue to consider is the z-direction uniformity of the dye. Initial nonuniformities may occur (e.g., if dye flows preferentially along the bottom side of the sheet) which require time for z-direction diffusion and dispersion to even out. We have found that a dyed zoned diameter over 5 cm gives good results in terms of z-direction uniformity of the dyed boundary. If we determine relative porosity using smaller zones, two-sidedness in the dyed zone may inflate the estimate of relative porosity. In highly permeable samples, such as ceramic paper, good uniformity also requires higher injection rates.

As the boundary exceeds about 10 cm, a significant decrease in relative porosity may occur due to dispersion, depending on the pore structure. In making measurements, we generally inject enough dye to obtain a dye boundary between 5 and 10 cm. Below we will report observed changes in relative porosity with the size of the dyed zone.

Experimental Results

In our last PAC Report, we showed preliminary results that gave relative porosity values much higher than predicted by the model of Kyan et al. We found that roughly 90% of the extrafiber pore space (based on specific volume estimates from permeability measurements) was

open to flow, while the Kyan model indicates that only 20-30% of the extrafiber pore space should be open to flow for the conditions of our tests.

RECENT PROGRESS

Further Experimental Results

In the last period, we have conducted further tests in a variety of paper types and have confirmed the preliminary estimates previously reported. Tests have been conducted in papers of bleached softwood kraft pulp, bleached hardwood kraft pulp, unbleached softwood kraft pulps, OCC, ONP, commercial blotter paper, and commercial ceramic fiber papers. Relative porosity in swollen wood fiber sheets is typically in the range of 40 to 60%, which corresponds to nearly 90% of the estimated extrafiber pore space being open to flow.

We have also conducted measurements comparing two different dyes to determine if dye-related effects are a source of systematic error. Results with Dextran Blue 2000 (MW ca. $2x10^6$) and Versatint Purple II (MW ca. 9000) gave no clear difference in relative porosity results, suggesting that the measurement technique probably is not sensitive to dye properties for nonabsorbing dyes (dyes with lower diffusion coefficients might give different results, as discussed below).

Examination of Kyan's geometrical model

The topic of relative or effective flow porosity in fibrous media has not received extensive treatment in the past. Kyan et al. (6) treated the issue theoretically, deriving expressions for relative porosity based on geometrical considerations for a structure composed of cylindrical fibers arrayed in a regular pattern. They noted that the pressure drop for flow in fibrous structures tends to be surprisingly high given the typically high porosity of the webs. They postulated that one reason for

the high pressure drop is that much of the pore space is occupied by stagnant fluid, or in other words, that the relative porosity is low. The derivation assumes that all the pore space behind a fiber in a representative cell of the fibrous structure (see Figure 3) is stagnant, and makes other simple assumptions about the geometry of the fibrous medium. The derived expression for effective flow porosity is

$$\varepsilon_{eff} = N_e^2(1-\varepsilon)\ (0.5/\pi) \tag{2}$$

where N_e is the effective porosity number,

$$N_e = \left(\frac{\pi}{0.5(1-\varepsilon)}\right)^{1/2} - 2.5. \tag{3}$$

These formulae give relative porosity values, $\varepsilon_{eff}/\varepsilon$, much less than unity. For example, a fibrous web with a porosity of 50% would have $\varepsilon_{rel} = 0.174$. Figure 4 shows predicted relative porosity as a function of total porosity.

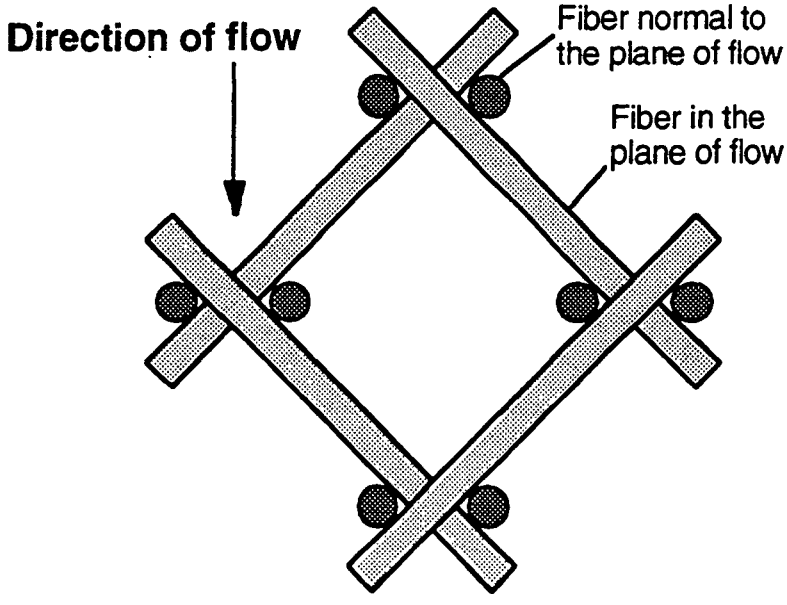

Figure 3. Unit cell of a fibrous medium used in the analysis of Kyan et al. (6).

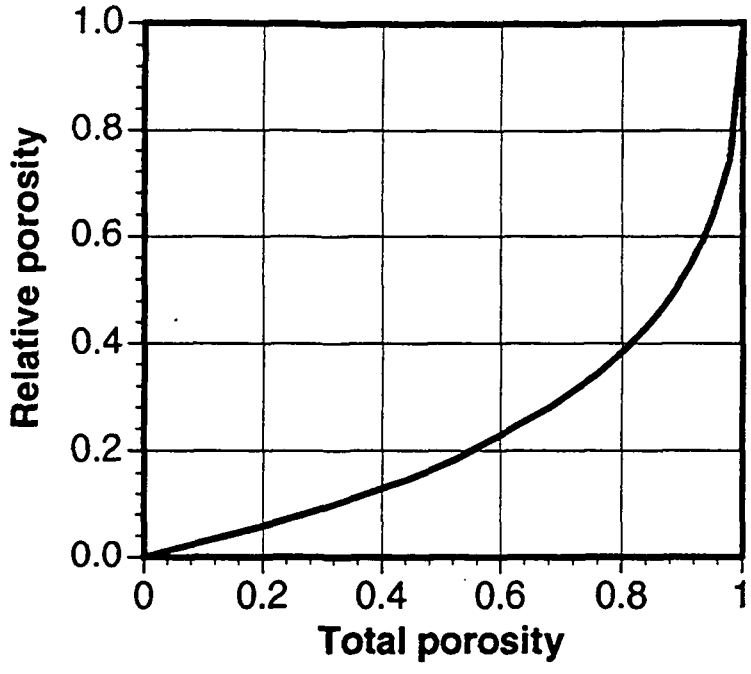

Figure 4. Predicted relative porosity based on the approach of Kyan et al. (6).

In the case of a swollen fiber, the porosity used in Equations 2 and 3 should be the extrafiber porosity, ε_0, if we assume that water trapped in the fiber does not flow. Again, we can use water retention ratios or specific volume data to estimate ε_0 as a function of ε, and then obtain new estimates for relative porosity based on Kyan's approach. The results are shown in Figure 5 for several values of specific volume, including the specific volume for completely unhydrated cellulose, 0.65 cc/g.

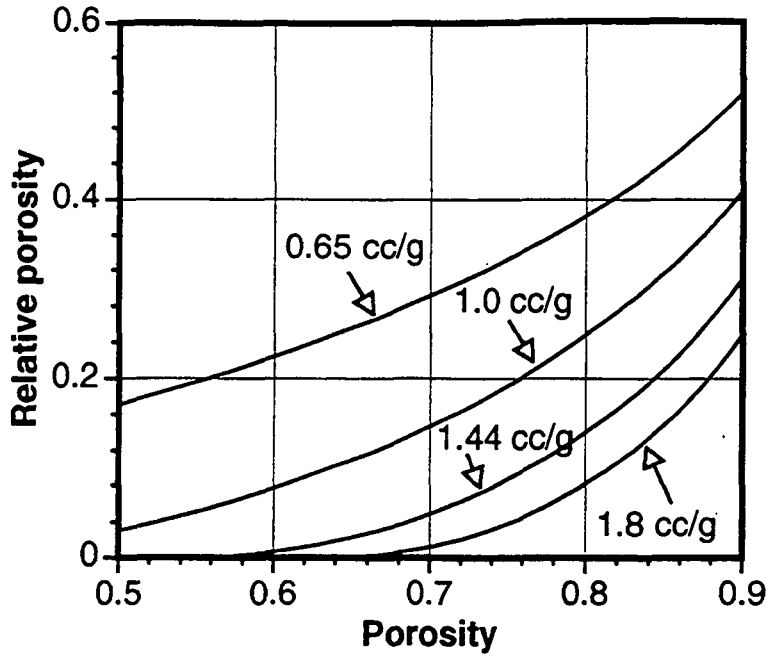

Figure 5. Relative porosity results based on a combination of Kyan's model (6) and extrafiber porosity analysis. Unhydrated fiber corresponds to α = 0.65 cc/g.

Significant reductions in relative porosity are predicted with swelling. In general, in the total porosity range of 0.6 to 0.75, where we expect typical furnishes to have specific volumes of roughly 1.0 cc/g or higher, the predicted relative porosity should be no more than 20%, based on our application of the only known model for relative porosity in a fibrous medium. In that same total porosity range, however, relative porosities as high as 80% could be achieved if the extrafiber pore space were free of dead-end pores and other zones of stagnant fluid. We will now test the applicability of the above analyses with experimental methods.

DISPERSION ANALYSIS

Dispersion of the dye as it moves through a porous medium can increase the apparent area occupied by dye, and in turn decrease the experimental estimate of relative porosity. In our initial work, we often did not see a dependence of relative porosity with dye zone diameter because it was either restricted to a narrow range or because the interaction between dye visibility and dilution

(from dispersion) fortuitously kept the apparent dye boundary in the "proper" location for good results. However, several sets of data, as shown in Figures 6 and 7, do show apparent relative porosity decreasing with increased extent of dye injection, indicating an experimental artifact that must be dealt with.

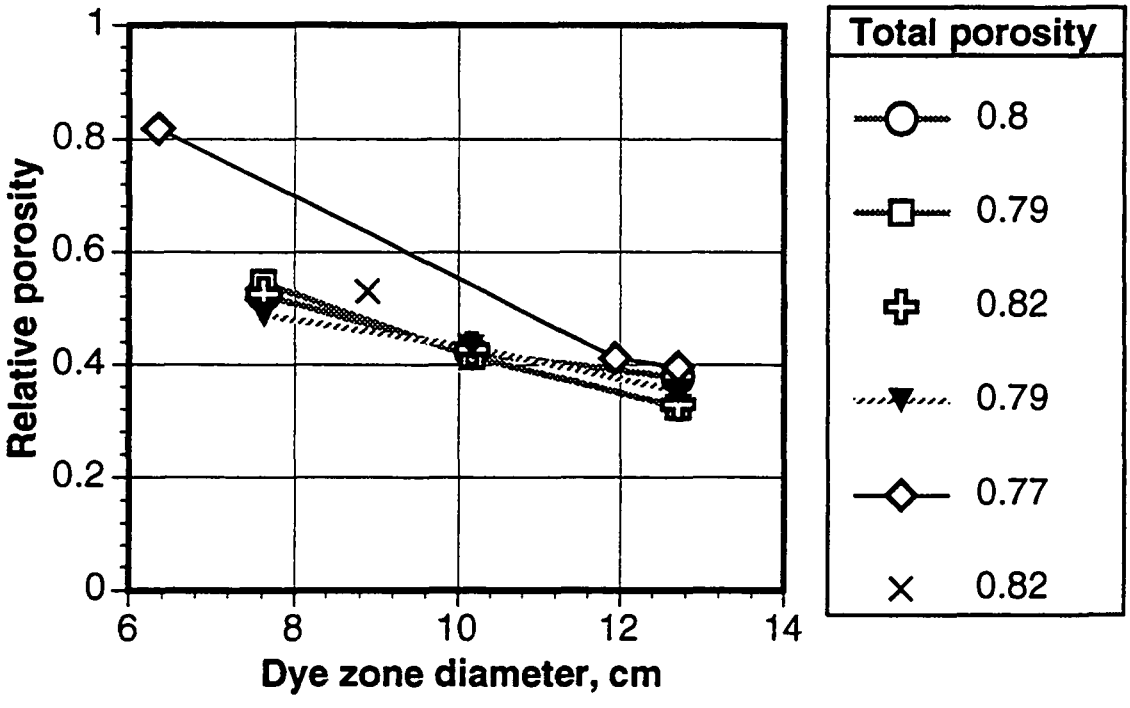

Figure 6. Relative porosity versus dye diameter in bleached kraft handsheets.

Much of the preliminary work with unbleached kraft was conducted before we completed our analysis of dispersion, which is presented below. In these tests, we usually did not notice a significant dependence of relative porosity on dye zone diameter; i.e., similar results were obtained in virgin sheets for dye zones from 6 to 12.7 cm in diameter. In retrospect, the difficulty of detecting diluted dye in a dark sheet probably prevented dispersion from affecting our results significantly, as we will discuss below.

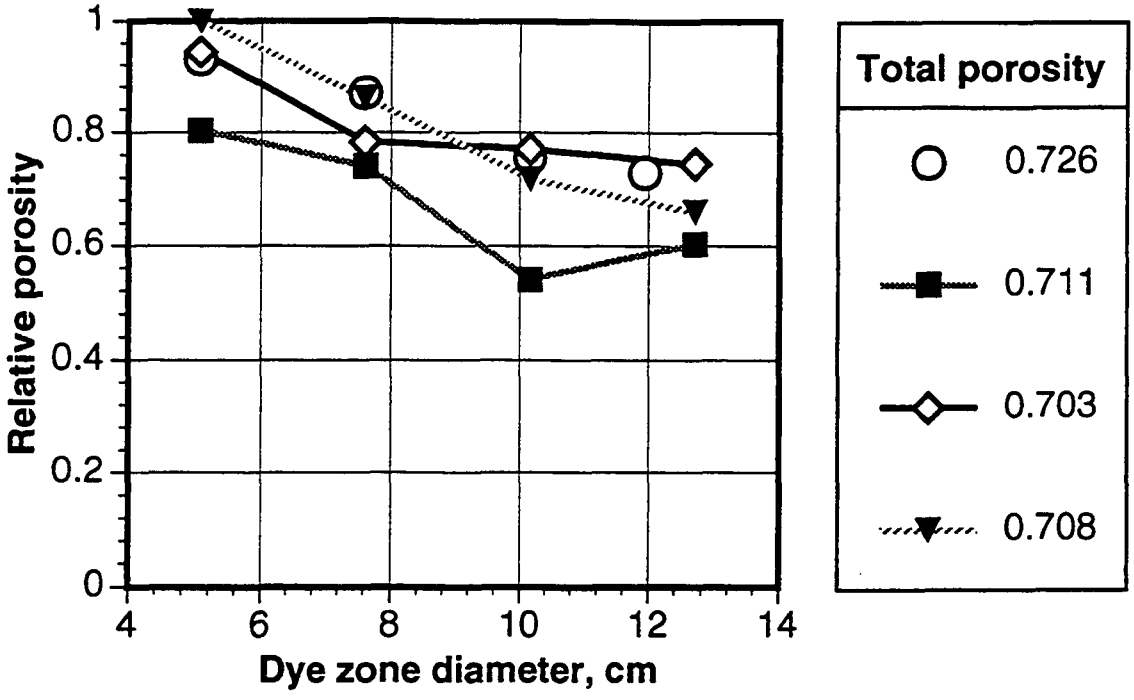

Figure 7. Relative porosity results in saturated blotter paper as a function of dye zone diameter injected into the sheet.

The issue of dispersion will be considered in two simple ways. We will first consider the dispersion that occurs at a microscopic level in a single cylindrical pore extending through a porous medium. Then we will treat the averaged, macroscopic case of dispersion in a porous medium using a radial geometry that corresponds to our experimental conditions. In both cases we will consider how the dispersion of an initially sharp dye boundary may affect our relative porosity results.

Dispersion in a Capillary Tube: The Taylor Dispersion Problem

Flow in a single pore can be simulated as laminar flow in a cylindrical capillary tube. The parabolic velocity profile for laminar flow leads to dispersion, for the fluid traveling in the middle

of the tube flows at twice the average velocity, while the fluid at the walls has zero velocity. If a sharp boundary between dyed fluid and clear fluid existed initially, this boundary will soon be spread out in the flow direction, as depicted in Figure 8.

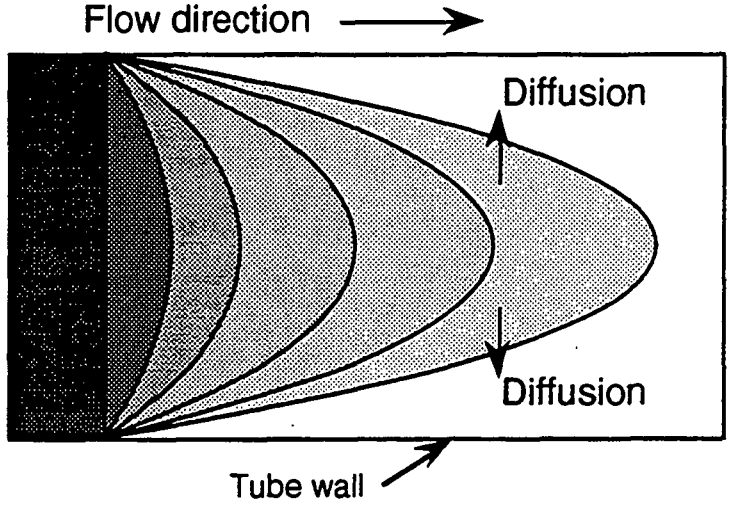

Figure 8. Distortion of a flat dye-water boundary moving in a flow with a parabolic velocity profile. Some of the dye advances faster than the average flow velocity.

The dispersion of the dye boundary is partially countered as dye from the fast-flowing center of the tube diffuses into slower moving fluid. If diffusion is rapid, the advancing dye front becomes narrow (assuming that the axial flow is fast compared to axial diffusion).

The simplified convection equation for this problem is

$$\frac{\partial C}{\partial t} = D_d\left(\frac{\partial^2 C}{\partial r^2} + \frac{1}{r}\frac{\partial C}{\partial r} + \frac{\partial^2 C}{\partial x^2}\right) - 2\overline{V}\left(1 - \frac{r^2}{R^2}\right)\frac{\partial C}{\partial x} \qquad (4)$$

where C is the concentration of dye, t is time, r is the radial distance from the centerline of the capillary, R is the radius of the capillary, x is distance in the flow direction, and $\overline{V}$ is the average velocity of the fluid. In Equation 4, dye transport in the x-direction is assumed to occur predominantly by axial convection rather than molecular diffusion, so the term for diffusion in the

x-direction has been dropped. Taylor (7,8) has provided approximate solutions for this problem, depending on the flow characteristics. If

$$\frac{2L}{\overline{V}} >> \frac{R^2}{14D_d}, \tag{5}$$

where L is the distance downstream from the original dye front, then radial diffusion dominates. In that case, at a distance x downstream from the original dye boundary, the ratio of average dye concentration, C_{avg}, to the undispersed (initial) dye concentration, C_o, is:

$$\frac{C_{avg}}{C_o} = \frac{1}{2}\left(1 \pm \text{erf}\frac{x - Vt}{2\sqrt{D't}}\right) \tag{6}$$

where D' is a dispersion coefficient related to the average velocity and the molecular diffusion coefficient, D_d, by

$$D' = \frac{R^2 \overline{V}^2}{48D_d}. \tag{7}$$

The length of the transition zone, defined as the region in which concentration varies from 10% to 90% of C_o, is given by

$$L_{tr} = 0.52R\overline{V}\sqrt{\frac{t}{D_d}} \tag{8}$$

which shows that the rapid diffusion leads to a plug flow motion of the displacing fluid, in spite of the parabolic velocity profile (9).

The Versatint Purple II dye is a proprietary polymer-based dye with a molecular weight near 9000. Although diffusion coefficients are not available for this dye, the value for diffusion in water probably lies in the range of $1x10^{-7}$ to $1x10^{-6}$ cm^2/s, based on reported coefficients for other polymers of similar molecular weight (10). Using the limits of this range, we can calculate the dispersion in the dye front. In Figure 9, we show the results for a true dye-injection distance of 5

cm ($t^* \overline{V}$ =5 cm) through a 100 μm pore with a mean velocity of 0.05 cm/s (a representative velocity for much of our work). Axial convection in the tube makes some dye present well beyond the "correct" penetration distance of 5 cm. If a dye with $D_d = 1x10^{-7}$ cm/s were used, and if a concentration only 10% of the original dye concentration would be identified as the edge of the dye boundary, then the experimenter would report 5.4 cm as the distance of dye penetration instead of 5.0 cm, and the estimated relative porosity would be underestimated by about 10%. The assumed pore size of 100 μm is larger than most pores in paper; smaller pore sizes lead to decreased dispersion, so the estimate of 10% error may be an upper limit for this line of analysis. Of course, this analysis is based on flow in a single tube, which overlooks the real nature of the dispersion problem in a complex porous medium. A more appropriate approach is now considered.

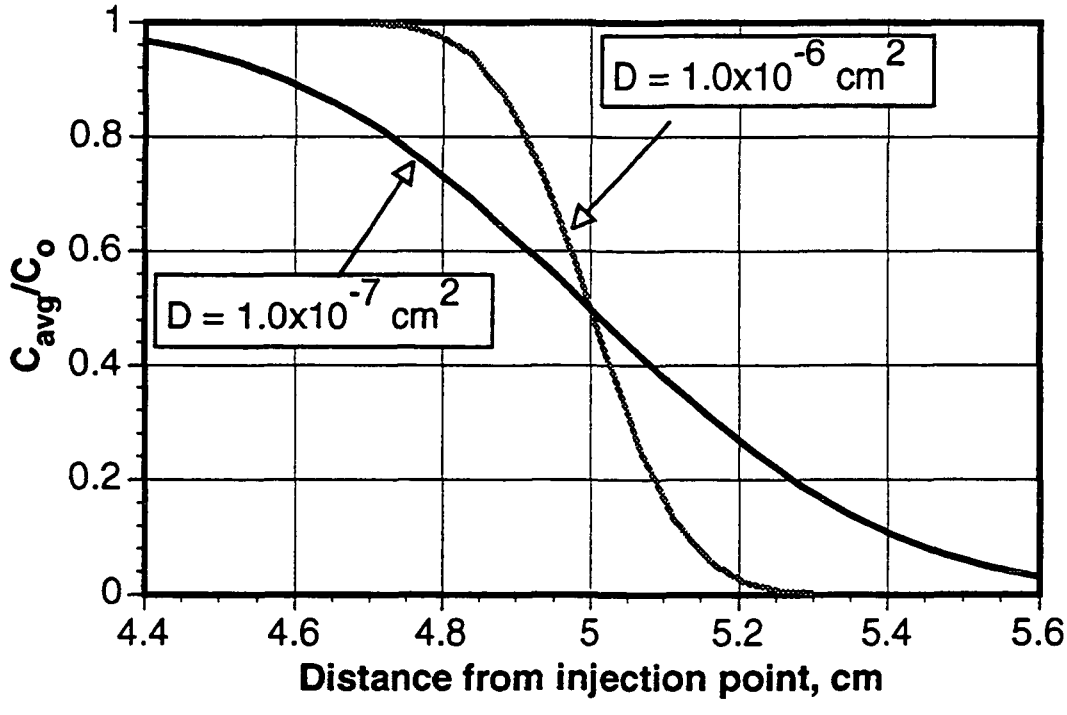

Figure 9. Predicted dispersion of a dye boundary after 5 cm travel in a capillary tube.

Dispersion in a Porous Medium

A real porous medium has a complex network of pores and throats which is best treated at the macroscopic level using empirical parameters such as permeability to describe the average transport behavior of the system. The geometry we will deal with is shown in Figure 10. We will treat the porous medium as a homogeneous continuum, with a steady, radially symmetric velocity field emanating from the injection port. At time t = 0, the injected water is replaced with a slug of aqueous dye solution having the same properties as water except for the dye concentration. Our fundamental transport equation (averaged over the homogenous porous medium) becomes

$$\frac{\partial C}{\partial t} + v(r)\frac{\partial C}{\partial r} = \frac{1}{r}\frac{\partial}{\partial r}\left(rD\frac{\partial C}{\partial r}\right) \tag{9}$$

where D is the effective dispersion coefficient in the porous medium in m^2/s, and v(r) defines the velocity field as a function of radial position. For steady radial flow in a fibrous mat, with an inlet port of size r_i and a mat diameter of r_o, the velocity is given by

$$v(r) = \frac{K\Delta P}{\mu r \ln(r_o/r_i)} \equiv \frac{B}{r} \tag{10}$$

where ΔP is the difference between the injection pressure and atmospheric pressure, μ is the fluid viscosity, and B is a constant for a given flow condition. geometry, fluid, and pressure drop across the sample. If we combine Equations 9 and 10, and assume that the effective dispersion coefficient is a constant, the dye transport equation becomes

$$\frac{\partial C}{\partial t} = D\left(\frac{\partial^2 C}{\partial r^2} + \frac{1}{r}\frac{\partial C}{\partial r}\right) - \frac{B}{r}\frac{\partial C}{\partial r}. \tag{11}$$

In dimensionless form, this becomes

$$\frac{\partial C'}{\partial \tau} + \frac{(P-1)}{r'}\frac{\partial C'}{\partial r'} = \frac{\partial^2 C'}{\partial r'^2} \tag{12}$$

where $\tau \equiv Dt/\Delta r^2$ ($\Delta r = r_o - r_i$), $r' \equiv r/\Delta r$, $C' \equiv C/C_o$ (C_o is the initial dye concentration), and $P \equiv B/D$ or $rV(r)/D$, which we term the radial Peclet number (as opposed to the "pore" Peclet number, introduced below).

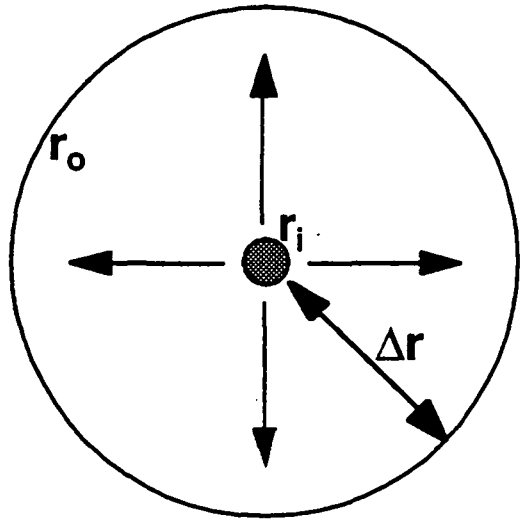

Figure 10. Radial geometry of fibrous mat with dye injection flow.

The assumption of constant dispersion coefficient is helpful in performing a crude analysis of this problem, but in reality the dispersion coefficient will vary with position since it is a function of flow velocity. Greenkorn (11) provides a useful discussion of longitudinal dispersion and its complex relationship to flow velocity and molecular diffusion. The dimensionless dispersion number, D/D_d, is a function of the pore Peclet number, $Pe \equiv a\,\overline{V}\,/D_d$, where a is the average pore radius. For the flows used for this study, pore Peclet numbers greater than 20 are typical, for which we may use the approximate relationship

$$\frac{D}{D_d} \approx \gamma Pe^{1.2} \qquad (13)$$

where γ is an empirical parameter on the order of unity. In considering the relationship between P in Equation 12 and the terms in Equations 10 and 13, we see that either a high molecular diffusivity

or a low flow velocity increases P, which means that convection of the dye boundary dominates over dispersion of the boundary. One of the mechanisms that reduces the impact of dispersion when molecular diffusion is high or velocity is low is the Taylor dispersion mechanism we considered above (e.g., see Equation 7). However, our analysis has assumed that the velocity is at least high enough to make longitudinal diffusion negligible compared to convection. If the velocity is too low ($Pe < 1$), then dispersion would become high due to longitudinal diffusion.

Application of estimated flow and diffusion parameters for our problems indicates that the radial Peclet number, P, should be no less than 100 and is more likely on the order of 1000. Even though Equation 12 is approximate and does not properly consider the variation of D with position, we will solve it for our problem to gain rough insights into the effect of dispersion on our results. (We have also solved the transport problem using two different forms of a variable dispersion coefficient that includes the effect of velocity variation in the flow field. The effect of variation in the dispersion coefficient for our problem proves to be minor. The numerical results thus obtained do not differ in substance from those reported here.)

The initial condition and boundary conditions are:

$$\tau = 0: \; C' = 0$$

$$r' = r_i/\Delta r: \; C'=1 \; (\tau>0)$$

$$r' = r_o/\Delta r: \; \partial C'/\partial r' = 0.$$

We used a finite difference approach (explicit form with second-order central differencing and upwind differencing of convective terms) to solve Equation 12 for various values of P. Results are shown in Figures 11 through 13 for P values of 10, 100, and 1000. In each of these figures, we show four different breakthrough curves corresponding to dye breakthrough at

locations of $\Delta r/4$, $\Delta r/2$, $3\Delta r/4$, and Δr (Δr is the distance from the edge of the injection port to the edge of the paper disk, or 6.35 cm - 0.28 cm = 6.07 cm). Breakthrough is arbitrarily defined as the moment when dye at a concentration of $0.1C_o$ first appears at the location of interest. The breakthrough points are marked in each figure.

In Figure 11, P is low enough that dispersion dominates. The dye boundaries are broad and diffuse. Large errors in measurement (ca. 50% or more in calculated relative porosity) could arise if dye at a concentration of $0.1C_o$ was taken as the dye injection boundary. In Figure 12, where P = 100, the effect of convection is more important, and the dye boundary advances with less broadening.

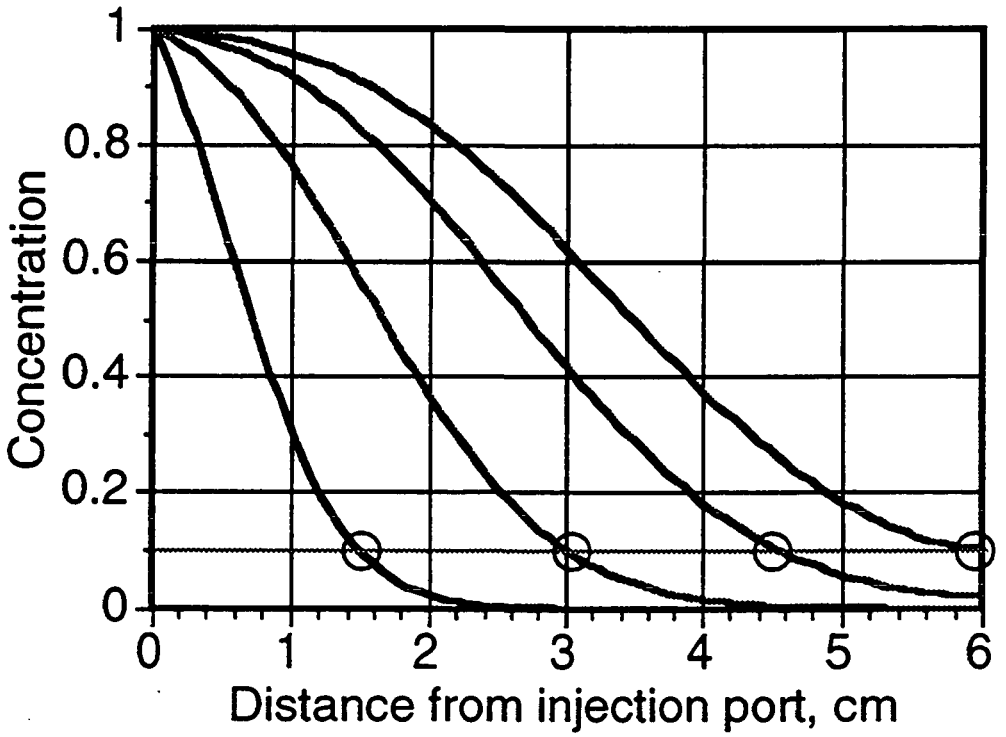

Figure 11. Computed breakthrough curves for P = 10.

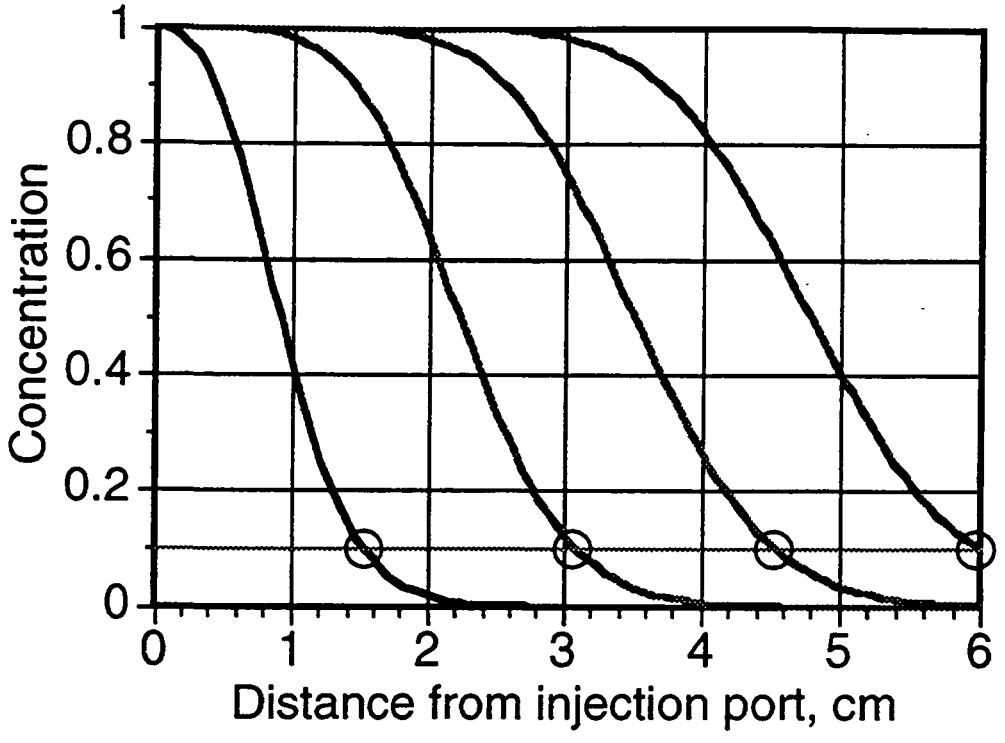

Figure 12. Computed breakthrough curves for P = 100.

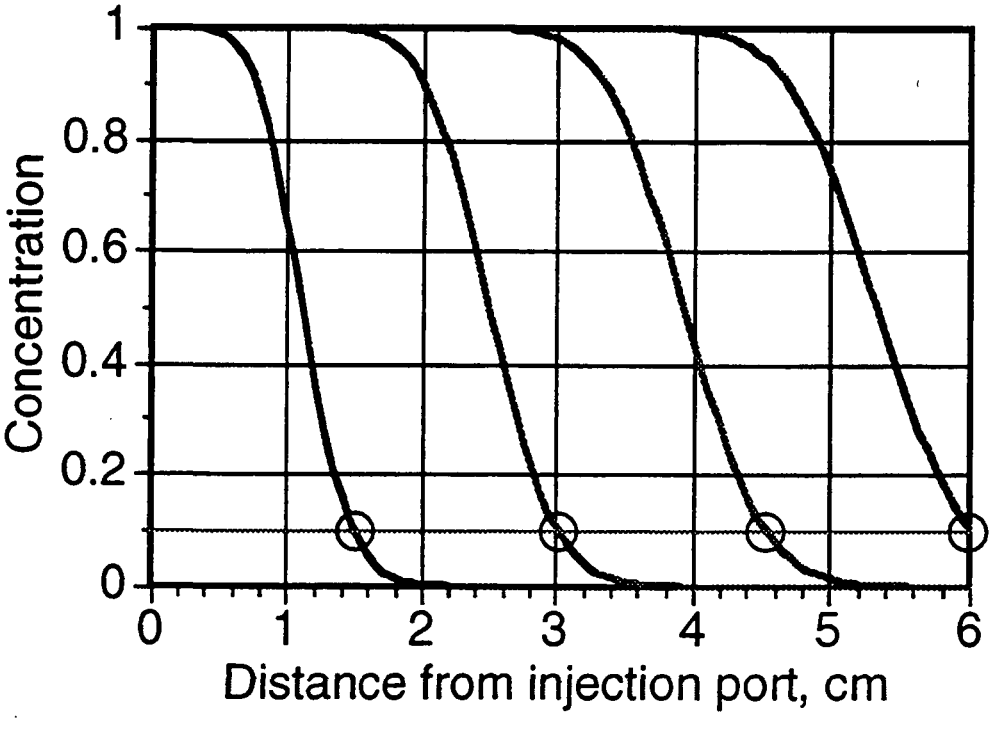

Figure 13. Computed breakthrough curves for P = 1000.

In Figure 13, where the P value of 1000 is more representative of our experimental conditions, dye concentration boundaries are narrower still. For example, consider an experiment in which we inject dye until a dye radius of 4.5 cm is detected (4.5 cm corresponds to $3\Delta r/4$, the detection point for third breakthrough curve). A numerical integration of the dye concentration given by the third breakthrough curve shows that the "correct" location of the dye boundary is 3.95 cm from the injection port – in other words, if the same amount of dye were injected with zero dispersion and pure plug flow, the dye boundary would be 3.95 cm. If dye diluted to 10% of the original concentration was mistaken for the "true" dye boundary (which might have been possible in several of our experiments), then we would have used a value of 4.5 cm instead of 3.95 cm for the extent of dye boundary growth. This gives an error of about 25% in the size of the dye boundary, which in turn would deflate the estimated relative porosity by about 20% of its correct value. The "correct" dye concentration to track is about 45% of the injected value (the radial geometry requires this to be less than 50%), which means that if we took a 45% dye solution as the location of the dye boundary, then dispersion would have a negligible effect on our determination of relative porosity. Based on our experimental procedures, we estimate that relative porosity error due to dispersion is usually in the range of 0 to -20%, although we showed some more extreme evidence of dispersion in Figures 6 and 7 above. In many experiments, the dye boundary appeared to be reasonably sharp, with an apparent width less than roughly 0.5 cm. In cases where the dye boundary was not sharp (based on appearance), the boundary used for calculations was taken as the approximate midpoint of the region with a visible dye concentration gradient, which should reduce some of the error caused by dispersion.

The analytical and numerical analyses show that some error is introduced by dye dispersion, but the effect does not jeopardize conclusions based on our simple methods. In fact, if the dye concentration is such that the detected dye boundary corresponds to slightly less than 50% of the injected dye concentration, then the error may be negligible (as it may have been in the tests with unbleached pulp). Dispersion errors will lower our estimates of relative porosity.

DISCUSSION

We have presented several sets of results from a study of relative porosity in fibrous structures. We conclude that much of the extrafiber pore space is available to flow. Adopting our results with nonswelling ceramic fibers, roughly 90% of that pore space may permit flow – at least under an in-plane pressure gradient.

Relative porosity values in paper were observed ranging from roughly 40% to over 80% in the total porosity range of 65 to 80%. These papers were not heavily refined, and based on permeability measurements in these sheets or in sheets from similar pulps, the compressed specific volume is expected to be between 1.0 and 1.5 cm^3/g. Fibers that have been dried (recycled fibers or resaturated blotter paper) will have lower specific volumes than the original virgin fibers.

If we assume that 90% of the extrafiber porosity is open to flow, or $\varepsilon_{rel} = 0.9\ \varepsilon_o$, then our previous results based on specific volume can be modified to make a more realistic prediction of relative porosity. The results are shown in Figure 14. Relative porosity values for moist paper made from lightly refined pulp may typically lie between or near the curves shown.

We have only considered relative porosity for in-plane flow. For flow in the transverse direction, it is possible that the differing pore structure could affect relative porosity. For example, flow normal to a flat fiber may have a stagnant zone on the downstream side of the fiber at sufficiently high particle Reynolds numbers (when inertial effects are important). In creeping flow, however, flow over a flattened fiber ought to be able to curve around the fiber surface, leaving no stagnant zones due solely to the fiber shape. But if relative porosity is an anisotropic parameter, we would anticipate a lower value for the transverse direction than for lateral flow.

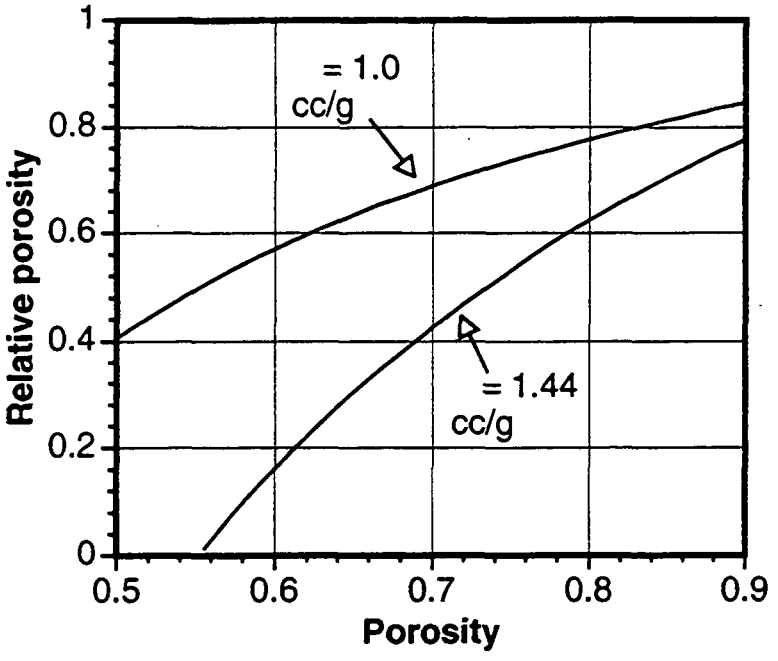

Figure 14. Predicted relative porosity results based on 90% of extrafiber pore space being open to flow.

Our results are subject to several sources of error, including dispersion, and can only be taken as estimates. However, most sources of error will tend to lower the calculated relative porosity. The errors are unlikely to reverse our conclusion that dead-end pores in the extrafiber pore space are relatively insignificant, at least for the papers and the flow conditions of our study.

Applications

Mechanical water removal processes rely on flow of water, which must occur in the open pore space. (As compression occurs, water is squeezed from the cell walls into the open pores where it can flow; the specific volume or WRR is simultaneously reduced.) An understanding of relative porosity is relevant to the limitations of mechanical dewatering. In wet pressing, for example, as the sheet is compressed, a limit is reached when the relative porosity goes to zero in a highly compressed sheet.

Relative porosity is especially important in an alternative to wet pressing, displacement dewatering. In displacement dewatering, high densification of the sheet is avoided by using a gas phase to push liquid water out of the pores of a lightly compressed sheet. The objective is to decouple density and dryness, yielding a dewatered sheet with high bulk. This process has been investigated for several years at IPST (12). The effectiveness of the process will be directly related to the effective porosity. If the effective porosity were unity, in theory, one could hope to displace all of the liquid from the sheet (in reality, viscous fingering and capillary effects would lead to some water retention even then). In practice, we can only remove a fraction of the available water. For example, in a sheet pressed to a porosity level of 70% (giving 40% solids when saturated with water), a reasonable relative porosity value of 50% means that no more than 50% of the fluid in the compressed sheet could be displaced. If this much fluid were displaced, the solids level would be raised from 40% (for a saturated sheet) to 57% with no significant increase in densification. In practice, only about half of the water in open pores is removed by gas displacement. (This is a rough estimate.) However, the relative porosity value, if known, helps put an upper bound on what could be achieved in an ideal process.

For the penetration of ink, size, or coating color into a dry sheet, dry relative porosity tests may be of some value. Based on our tests with lateral flow, air entrapment in the pores does not seem to be a serious problem. Of course, z-direction relative porosity measurements are needed to properly address this issue.

RELATIVE POROSITY CONCLUSIONS

The Kyan model for relative porosity appears to underpredict relative porosity values in real fibrous structures. Based on our results here, the extrafiber pore space of a paper structure is largely open to flow, with perhaps only 10% of that space truly confined to dead-end pores or stagnant zones. Of course, the details of the sheet formation will determine what fraction is open to flow. We clearly need to expand our base of results to clarify this issue.

The effects of diffusion and dispersion have been considered and treated analytically and numerically, though with substantial simplification. Our analysis suggests that dispersion can introduce error into our results, but for our procedures (using Versatint Purple II dye) and our flow conditions, this error will often be less than 20% and can be made negligible in some cases.

A thorough investigation of relative porosity, or of two-phase flow processes in paper, should consider the possibility of anisotropy and velocity-dependent effects. To date, we have done neither.

Relative porosity measurements in the thickness direction of paper appear to pose serious experimental challenges. Flow rate effects will be explored, but we expect that they will be minor as long as inertial effects can be neglected (i.e., as long as Darcy's law is sufficient to describe the flow). For most papermaking operations after the forming section, inertial effects are minor (even in wet pressing).

Further work will include measurements with nonswelling fluids injected into paper to better understand the difference in pore structure between wet and dry sheets. Additional studies of recycling effects will also be carried out.

II. INERTIAL EFFECTS IN FIBROUS MEDIA

In the past period we have examined inertial effects in fibrous media, extending work performed for a separate research project. We have determined that previous assumptions about inertial effects in fibrous media may be in error, particularly with respect to the dependence of inertial terms on fiber diameter. In the experimental work reported below, we used high velocity air flow through paper made from well characterized ceramic fibers on a pilot Fourdrinier machine. The paper samples were supplied by Thermal Ceramics of Augusta, Georgia. While we have yet to perform the inertial effects tests in cellulosic paper, we expect our preliminary observations to still be valid. Until the work in paper has been completed (scheduled for Spring of 94), the results shown here should be viewed as preliminary.

THEORY AND PREVIOUS WORK

Darcy's law (13) can provide more useful information, though Darcian permeability is less easily measured. Darcy's law states that the velocity of fluid flow through a porous medium is directly proportional to the pressure gradient:

$$v = \frac{K}{\mu}\frac{\Delta P}{L} \qquad (14)$$

where v is the superficial velocity (flow rate divided by area), K is the permeability, μ is the fluid viscosity, and ΔP is the pressure drop in the flow direction across a distance L. The units of K are m^2. In Equation 14, the permeability is an empirical proportionality parameter linking fluid velocity to pressure drop and viscosity. For a homogeneous medium, K is not a function of ΔP, sample length, or viscosity, but is an intrinsic parameter describing the flow resistance of the medium.

In a compressible medium, permeability will be a strong function of the degree of compression. The relationship between permeability and porosity is often expressed in terms of the Kozeny-Carman equation. This equation is based on a conduit model of flow through porous

media (treating the medium as if it contains cylindrical pores running from one end to the other). The general form of this equation is:

$$K = \frac{1}{\kappa S_o^2} \frac{\varepsilon^3}{(1-\varepsilon)^2} \tag{15}$$

where ε is the porosity (fractional void volume), S_o is the surface area per unit volume of solid material, and κ is a shape factor (the Kozeny constant) which accounts for effects of channel shape and orientation. The Kozeny constant can be derived for ideal, simple pore structures, but becomes an empirical factor for real porous media. In many cases it is not constant but a function of porosity. For fibrous media, a value of 5.55 is a widely used value which works well in many cases (14), although values typically may lie in the range of 3-7 for porosities less than 0.8 (15) and can be much greater than 5.55 for high porosity.

For an infinitely cylindrical fiber, the ratio of surface area to volume is simply:

$$S_o = \frac{4}{D_f} . \tag{16}$$

(For D_f in meters, Equation 16 gives units of m^2/m^3. With D_f in microns, S_o has units of m^2/cm^3.) Combining Equations 15 and 16 and using 5.6 as the value of the Kozeny constant, we obtain:

$$K = \frac{D_f^2 \varepsilon^3}{90 (1-\varepsilon)^2} . \tag{17}$$

Inertial Flow Effects (High-Velocity Flow)

At sufficiently high flow rates, Darcy's law is no longer valid. The relationship between pressure drop and flow rate departs from linearity, with an additional quadratic term becoming significant:

$$-\frac{dP}{dx} = \alpha v + \beta v^2 , \tag{18}$$

which is often modeled in terms of Darcian permeability and a Forchheimer constant, C:

$$-\frac{dP}{dx} = \frac{\mu v}{K} + \frac{\rho C v^2}{\sqrt{K}} , \tag{19}$$

where ρ is the density of the fluid and K is Darcian permeability. Empirically, inertial effects are often well modeled by the Ergun equation, which relates a dimensionless friction factor to the particle Reynolds number for unconsolidated (uncompressed) media such as glass beads or sand:

$$f_p = 1.75 + 150/Re_p, \tag{20}$$

where the dimensionless parameters are defined as:

$$f_p = \frac{D_p \varepsilon^3}{\rho v^2 (1-\varepsilon)} \frac{\Delta P}{L}, \tag{21}$$

$$Re_p = \frac{D_p v \rho}{(1-\varepsilon) \mu} . \tag{22}$$

For fibrous media, the analysis leading to Equation 17 can be applied to show that the Ergun equation might be more appropriate for fibrous media if we use 90 instead of 150 as a constant, giving

$$f_p = 1.75 + 90/Re_p. \tag{23}$$

We can show that if the Kozeny-Carman equation is valid (Equation 15 or 17), then the inertial components of Equations 19 and 20 are consistent only if the parameter C in Equation 6 varies inversely with porosity to the 3/2 power:

$$C(\varepsilon) = \frac{\Gamma}{\varepsilon^{3/2}} , \tag{24}$$

where Γ should be a constant. For a fibrous medium in which the fibers are long and uniform in diameter, we can combine Equations 17, 19, 23, and 24 to determine that Γ should be approximately 0.18.

Analysis becomes more complex when we realize that gas density and velocity are changing across a sample during flow. For an ideal gas, however, we can show that Equation 19 can be integrated and manipulated to yield a simple result:

$$\frac{\Delta P}{L} = \frac{\mu v_{avg}}{K} + \frac{\rho_{avg} C v_{avg}^2}{\sqrt{K}}, \tag{25}$$

where v_{avg} and ρ_{avg} are the gas velocity and gas density evaluated at the average absolute pressure across the sample (the average pressure is the simple average of the inlet and outlet pressures at the sample boundaries). In terms of porosity and the factor Γ, Equation 25 can be rewritten as:

$$\frac{\Delta P}{L} = \frac{90\mu v_{avg}(1-\varepsilon)^2}{D_f^2 \varepsilon^3} + \frac{\sqrt{90\Gamma}(1-\varepsilon)\rho_{avg} v_{avg}^2}{D_f \varepsilon^3}, \tag{26}$$

which will be useful in the analysis of the data presented below.

Experimental Methods

The apparatus for measuring air flow effects in ceramic paper samples is shown in Figure 15. The device is an adaptation of the IPST liquid permeability apparatus. The upper and lower heads in Figure 15 are mounted in a Carver press frame that uses a pneumatic system, including Firestone air bags, to compress a sample assembly between the two heads. For this study we applied loads up to 2000 lbs, giving a pressure of nearly 300 psi for the 3-inch diameter samples used in this study.

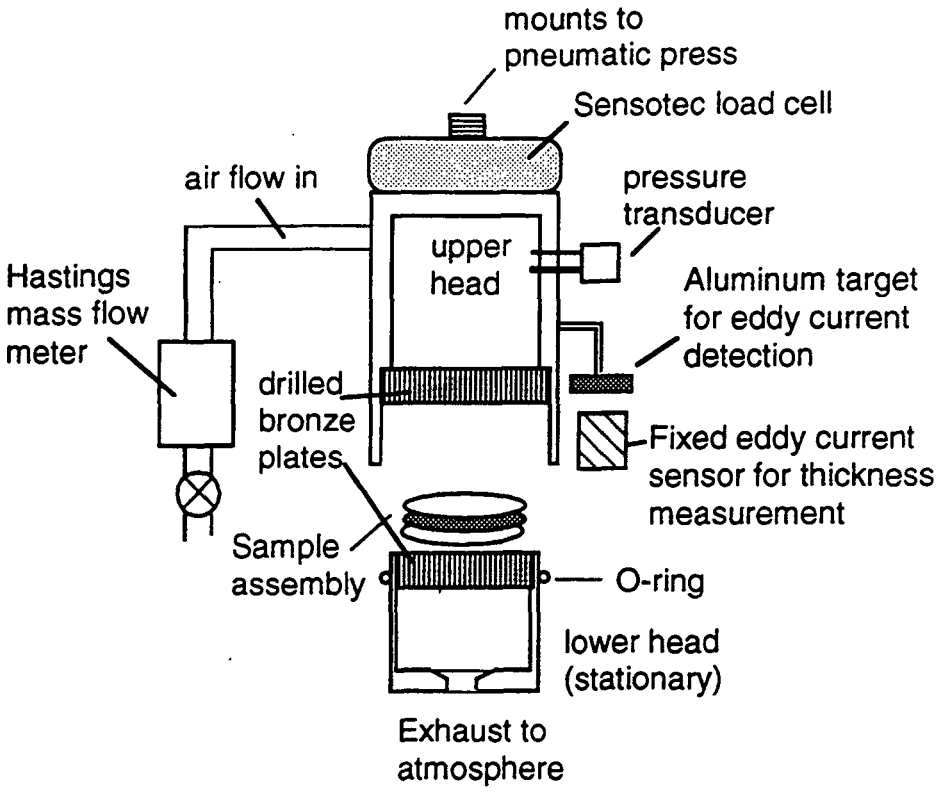

Figure 15. Air flow apparatus for measurements in ceramic paper.

A critical consideration in air flow measurements is the flow path through the sample. Three objectives must be met: (1) the flow must be applied uniformly to the flow area, meaning that the inherent nonuniformity of flow coming through a drilled metal surface must be evened out; (2) mechanical pressure must also be applied uniformly; and (3) the flow must traverse the sample in a controlled and known flow region. These objectives are achieved using a multilayer sample assembly that distributes mechanical load and flow, while restricting flow to a central circular region of the sample. To increase the maximum velocities that we could obtain in our system, we restricted the flow area to a circle 0.67 inches (1.7 cm) in diameter, representing only 5% of the total sample area for the 3-inch disks that are cut for placement in the sample assembly. The sample assembly is a stack of thin plastic disks, bronze wire and fine woven plastic mesh, as shown in Figure 16. The porous segments of the assembly (wire meshes) must have sealed edges to prevent flow bypassing the sample by traveling sideways through the wire mesh, around the sample, and

then sideways through the lower wire mesh and out of the test apparatus. This problem is termed "edge flow," and is easily detected by placing an impermeable plastic sheet over a sample and then observing air flow rates as a function of applied pressure. We achieved negligible edge flow with our sample assembly design. We also examined impressions made with carbon paper in the loaded sample assembly to ensure that acceptable mechanical pressure uniformity was achieved.

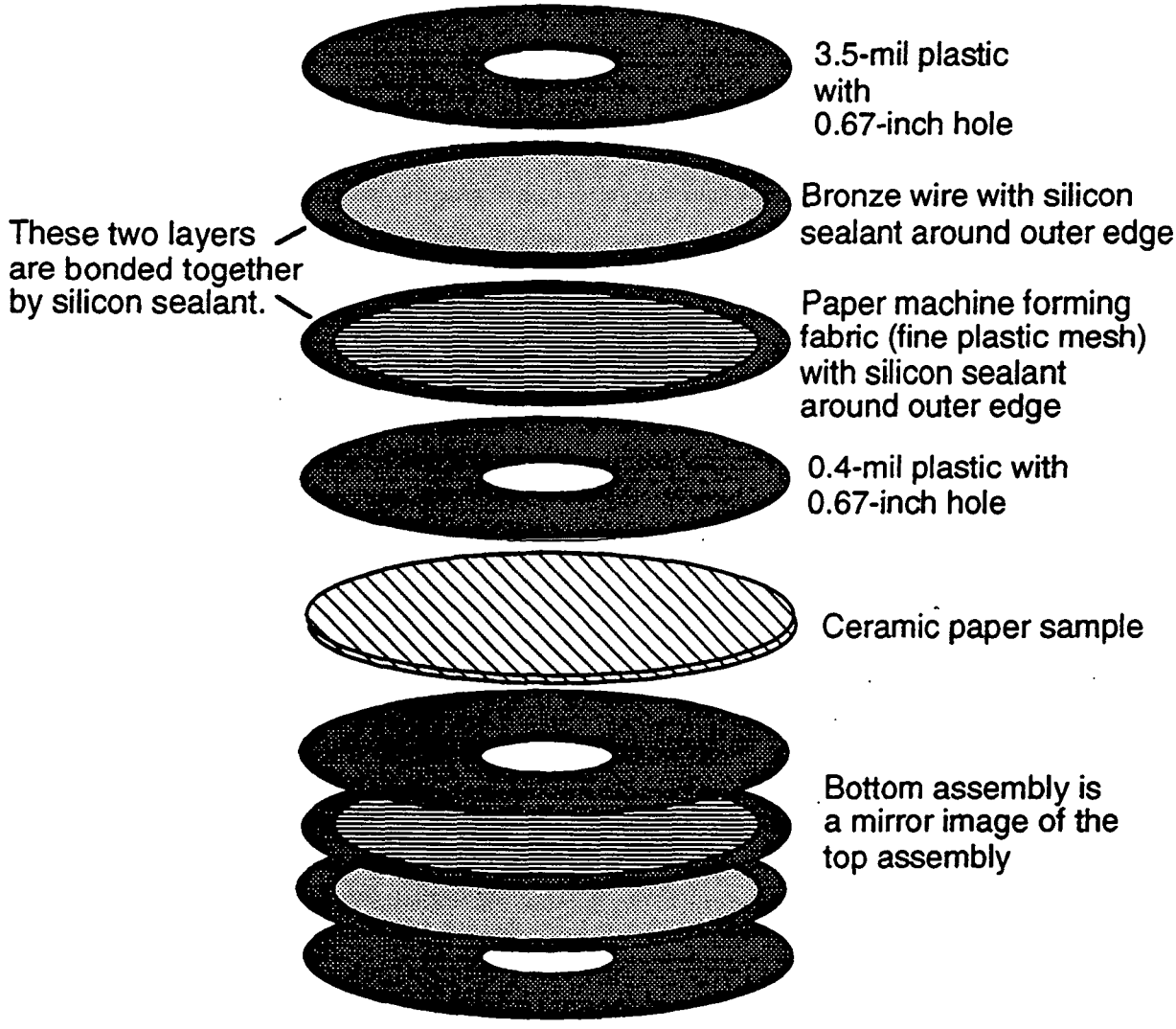

Figure 16. Sample assembly for air flow measurements.

The permeability measurements for each sample are made by measuring the flow through the sample at a known pressure drop, with the sample pressed under various loads (from 30 to 300 psi). Air mass flow rate is obtained from a Hastings mass flow meter installed after a manual

control valve from an air line. The flow meter has a range of 0-750 standard liter per minute (SLPM), with a resolution of 1 SLPM. Our typical flow range was 8 to 300 SLPM. This meter is especially convenient for this study in that it directly indicates mass flow, independent of the flow pressure or temperature. Permeability measurements require knowledge of pressure drop, absolute pressure, gas viscosity, gas flow rate, and sample thickness.

At each load, the thickness of the sample is measured using an eddy current transducer. The sample thickness is obtained by taking the difference between the ECT reading when a ceramic paper sample is present in the sample assembly and the reading when no sample is present, with both readings at the same applied load. The ECT sensor is adjusted to give a voltage signal linearly proportional to distance for an operating range of 160 mils.

As the load increases, the thickness of the sample also decreases, thus decreasing sample porosity. Porosity is calculated from the sample thickness, the dry sample weight, and the density of the pure ceramic:

$$\varepsilon = 1 - \frac{m_s}{AL\rho_f}, \tag{27}$$

where ε is porosity (fractional void volume), A is the area of the sample, L is its thickness, and ρ_f is the density of the fibers themselves. A value of 2.26 g/cm^3 has been used for the samples supplied for this study.

In making a measurement, we obtain pressure drop versus flow rate information at a given degree of compression by increasing the flow rate into the upper chamber (a valve is adjusted) and recording the air pressure in the upper chamber as well as the mass flow rate. ECT voltage readings and mechanical pressure (load in pounds) are also recorded. The inherent flow resistance in the system when no sample is present must be considered. We derived functions relating flow

resistance to flow rate, enabling us to subtract the portion of the pressure drop due to the piping, mesh, etc., from the measured pressure drop to obtain the frictional losses in the sample alone.

In obtaining permeability and inertial loss information from air flow measurements, information about flow rate, pressure drop, sample thickness, mechanical load, and sample weight are combined to yield data for $(\Delta P/L)/v_{avg}$ and ρv_{avg}. The motivation for this is that Equation 25, if both sides are divided by average velocity, yields a relationship amenable to linear regression:

$$\frac{\Delta P}{L v_{avg}} = \frac{\mu}{K} + \frac{C}{\sqrt{K}} \rho_{avg} v_{avg} , \tag{28}$$

or, if we substitute for C using Equation 24,

$$\frac{\Delta P}{L v_{avg}} = \frac{\mu}{K} + \frac{\Gamma}{\sqrt{K\varepsilon^3}} \rho_{avg} v_{avg} . \tag{29}$$

The regression yields constants for the intercept and slope which can then be used to obtain K (since the air viscosity is known) and then Γ, the inertial loss factor. Once K has been obtained, we can obtain the effective fiber diameter based on the porosity using Equation 17. (Note that $\rho_{avg} v_{avg}$ is equivalent to the mass flow rate divided by the flow area.)

Permeability Results

Figure 17 displays the effective fiber diameter results for the nine basic sample types examined during part of the present study. Multiple samples for each sample type have been averaged. Here fairly linear relationships are evident between shot and effective diameter, and true diameter and effective diameter. The lowest effective diameter occurs for the lowest shot and the lowest true fiber diameter. The highest effective diameter occurs with the highest shot and the greatest true fiber diameter. (Since permeability is proportional to the square of effective fiber diameter, a similar plot for permeability will show similar trends). Our measurements of these samples gave effective diameters between 3 and 4 μm.

The fiber diameters shown in Figure 17 were obtained for the high-load permeability runs (2000 lb loads), but similar fiber diameters were obtained at lower degrees of compression. Indeed, calculated effective fiber diameter was generally insensitive to load or porosity for a given sample, meaning that permeability measurements at low load can be applied to predict permeability behavior at higher load.

Figure 18 shows a plot of the inertial loss factor, Γ, as a function of shot and fiber diameter. In this case the lowest inertial effects are seen in the most permeable samples. The largest inertial loss factor occurs for sample 2 of Phase 2, which has the lowest permeability. Inertial loss is probably strongly affected by the minimum throat size of the pores through which the air flows. Low permeability materials may have greater loss factors. When Γ and K are known, Equation 15 can be used to predict the pressure drop that will occur for a given flow rate, or vice versa.

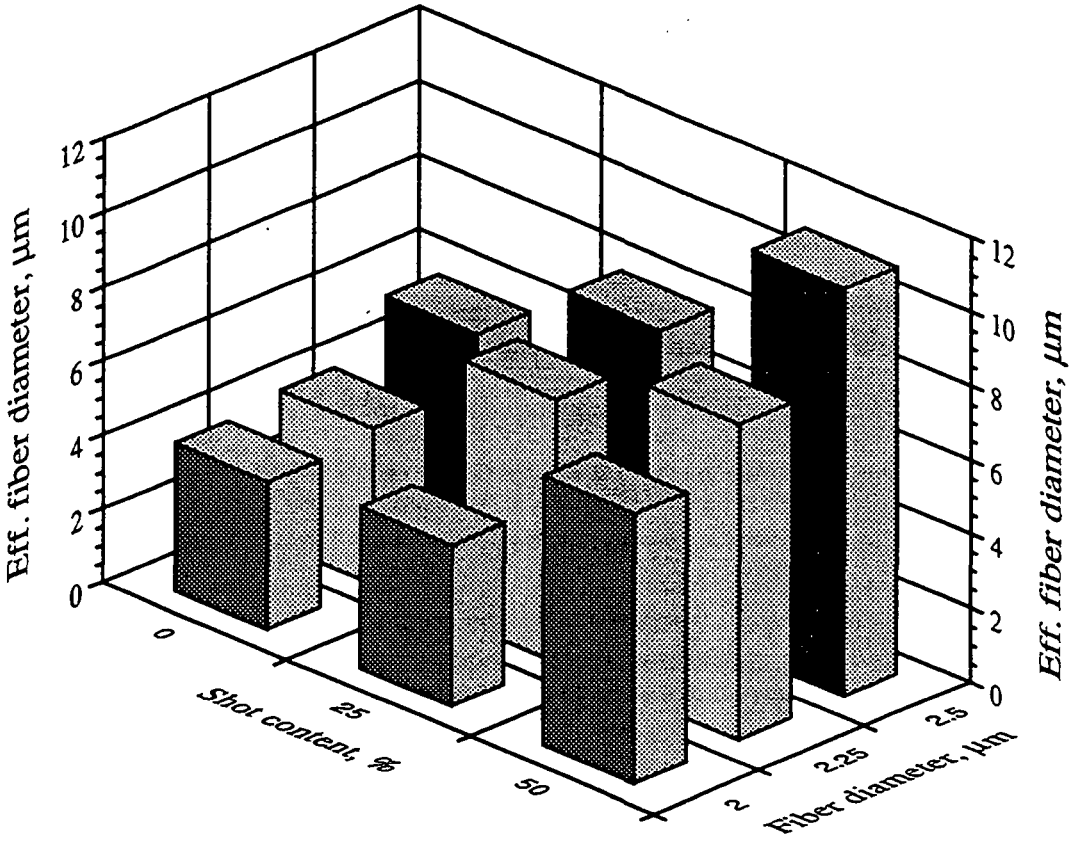

Figure 17. Effective fiber diameter as a function of shot content and fiber diameter.

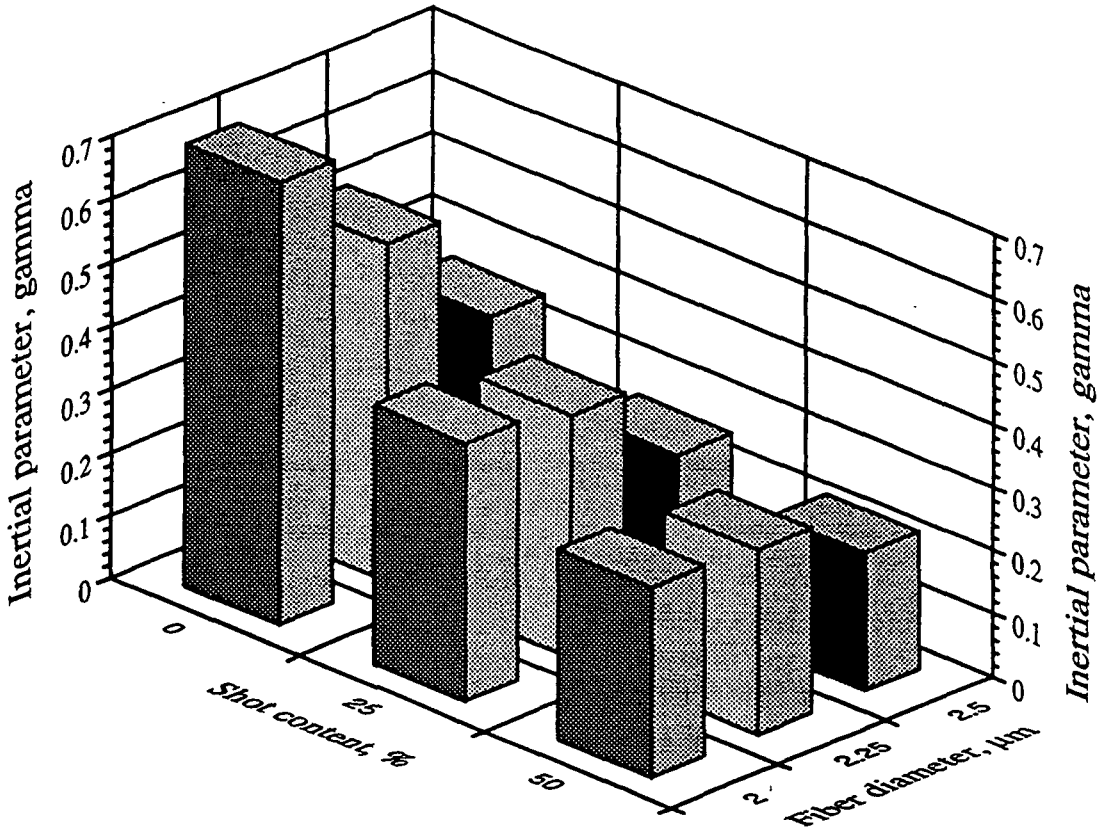

Figure 18. Inertial coefficient as a function of shot content and fiber diameter.

Accuracy

Most of the reported permeability values have a 95% confidence interval of roughly ±10%. Effective fiber diameters have a confidence interval of roughly ±6%. Higher error is accrued in determining Γ, and the 95% confidence interval may be as high as ±30%. In the regression used to obtain permeability and Γ at a given degree of compression, the standard error (one standard deviation) for the intercept (from which we obtain K) was typically less than 2%, while the standard error for the slope (from which we obtain Γ) usually ranged from 4% to 10%.

Discussion

Previous workers have suggested that inertial parameters such as Γ are indendent of fiber diameter for a given structure, but we have found a consistet dependence in fiber diameter.

The relative importance of permeability and inertial losses for a process will depend strongly on the velocity of the flow. For the relatively low velocities of this study (<20 m/s through the sample), inertial forces were of secondary importance. At much higher velocities, however, they may dominate the flow. In any case, the samples with larger pressure drops at low flow rates due to low permeability will also have larger pressure drops at high flow rates due to large inertial loss factors.

ACKNOWLEDGMENT

Thanks to Tom Merchant and Ye Xiao-Liang for technical assistance in this study. Thanks to Bernard Miller of TRI for a valuable discussion on relative porosity concepts. Thanks to Thermal Ceramics of Augusta, Georgia for providing ceramic paper samples and for allowing portions of previously conducted research to be applied to the broader issue of flow through fibrous media.

LITERATURE CITED

1. Lindsay, J. D., and Brady, P. H., "Studies of Anisotropic Permeability With Applications to Water Removal in Fibrous Webs," Part I, Tappi J., 76(9): 119 (1993).

2. Adams, K. L., and Rebenfeld, L., "In-Plane Flow of Fluids in Fabrics: Structure/Flow Characterization," Textile Research J., 57(11): 647 (1987).

3. Adams, K. L.; Miller, B., and Rebenfeld, L., "Forced In-Plane Flow of an Epoxy Resin in Fibrous Networks," Polymer Eng. and Sci., 26(20): 1434 (1986).

4. Adams, K. L.; Russel, W. B., and Rebenfeld, L., "Radial Penetration of a Viscous Liquid into a Planar Anisotropic Porous Medium," Int. J. Multiphase Flow, 14(2): 203 (1988).

5. Miller, B.; Friedman, H. L., and Amundson, R., "In-plane Flow of Liquids into Fibrous Networks," 1991 TAPPI Nonwovens Conference, Marco Island, Florida, May 1991.

6. Kyan, C. P., Wasan, D. T., and Kintner, R. C., "Flow of Single-Phase Fluids Through Fibrous Beds," Ind. Eng. Chem. Fundam., 9(4): 596 (1970).

7. Taylor, G. I., *Proc. Roy. Soc. A*, 219: 186-203 (1953).

8. Taylor, G. I., *Proc. Roy. Soc. A*, 223: 446-468 (1954).

9. Bear, J., *Dynamics of Fluids in Porous Media,* American Elsevier Publ. Co., New York, 1972, p. 585.

10. Brandrup, J., and Immergut, E. H., editors, *Polymer Handbook*, 2nd ed., John Wiley and Sons, New York, pages IV-73 and IV-85.

11. Greenkorn, R. A., *Flow Phenomena in Porous Media*, Marcel Dekker, Inc., New York, 1983, pp. 183-220.

12. Lindsay, J. D., "Displacement Dewatering to Maintain Bulk," Paperi ja Puu, 74(3): 232-242 (1992); also presented at the Helsinki Symposium on Alternate Methods of Pulp and Paper Drying, Helsinki, Finland, June 4-7, 1991.

13. Dullien, F. A. L., *Porous Media: Fluid Transport and Pore Structure*, Academic Press, New York, 1979.

14. Fowler, J. L., and Hertel, K. L., "Flow of a Gas Through Porous Media," J. Appl. Physics, 11: 496-502 (1940).

15. Chen, F. J., "The Permeability of Compressed Fiber Mats and the Effects of Surface Area Reduction and Fiber Geometry," Ph.D. Dissertation, The Institute of Paper Chemistry, Appleton, Wisconsin, June 1982.

FUNDAMENTALS OF DRYING

STATUS REPORT

FOR

PROJECT 3470

March 22, 1994

Institute of Paper Science and Technology
Atlanta, Georgia

Project Title: FUNDAMENTALS OF DRYING
Project Staff: David Orloff
Budget (FY92-93): $207,000
Reporting Period: March 1993 - March 1994
Division: Engineering and Paper Materials
Project Code: DRYING
Project No. 3470

OBJECTIVE

To develop an understanding and a database for commercialization of advanced water removal systems, based on high intensity drying principles. This new technology will reduce capital costs, increase machine productivity, reduce the amount of energy used, and improve properties.

GOAL

To commercialize the impulse drying process by 1998.

SUMMARY

Over the past year we have concentrated on expanding our knowledge of impulse drying to serve as a framework for decision making regarding its commercialization. Our focus has expanded to include mechanical design issues as well as process issues.

Key accomplishments for the reporting period include:

- Union Camp, Beloit and the Institute have agreed, in principle, to form a research and development agreement for the purpose of commercializing impulse drying for board grades.

- Experiments on Beloits' batch-pilot extended-nip shoe press confirmed the conditions under

which multi-ply/recycle containing linerboard could be successfully impulse dried and printed. In addition, sheet sticking problems were resolved by insuring the smoothness of the surface of the press roll, and by operating at roll surface temperatures above 150°C.

- A numerical model of a proposed controlled-crown impulse drying press roll was initiated in order to explore design parameters that optimize energy utilization and to predict stress within the impulse drying press roll.

- The design of a high speed test stand to document the long term durability of impulse drying press roll coatings has been initiated. In addition, the hydraulics and controls of the Institutes' impulse drying simulator have been improved to allow better control of press pulse shape.

- Student work was undertaken to determine the interdependency of the "thermal mass" of the heated press roll surface and press impulse on impulse drying performance.

- Student work to measure heat and mass transfer to a sheet during steam box operation has begun with the design and construction of an apparatus that can operate at speeds of 2500 feet per minute.

- Student work to investigate ways of opening the operating window of impulse drying have begun with the design of an apparatus to determine the effect of nip opening pressure on flash evaporation and sheet delamination.

DISCUSSION

The Research and Development Agreement For the Commercialization of Impulse Drying For Board Grades

In January of 1993 President Matula corresponded with the CEOs of IPST member companies to solicit their interest in participating in a consortium to commercialize impulse drying. Following those correspondences, technical presentations were made at the headquarters of interested member companies. These, in turn, were followed by business meetings, at the Institute, to form the consortium.

The end result of that process was an agreement in principle between the Union Camp Corporation, the Beloit Corporation and IPST to commercialize impulse drying for board grades.

At the time of writing of this report, the various parties are finalizing the agreement. A formal proposal to DOE, to assist in financing the project, is being prepared.

Batch-Pilot Extended-Nip Shoe Press Experiments At the Beloit Corporation

Experiments have been completed on the Beloit sheet-fed pilot impulse drying shoe press as described in a recent IPST Member Report [1]. In those experiments, both single and double-ply handsheets of various furnish structures were both impulse dried and double felted pressed. In the case of impulse drying, both the IPST "C" ceramic roll coating and a Beloit "A" roll coating were applied to cast iron rolls, ground to provide smooth surfaces, and evaluated. The major conclusions to be drawn from the study may be summarized as:

Sheet Sticking: The Beloit "A" and IPST "C" rolls were operated without sheet sticking at temperatures above 150°C with de ionized felt wash water. The Beloit "A" roll also did not stick when "hard" (calcium carbonate containing) felt water was used. Hence, it is concluded, that previously observed high temperature sheet sticking was due to excessive press roll surface roughness.

Press Roll Surface Strength: The IPST "C" roll coating was susceptible to chipping under shear, while the Beloit "A" roll did not chip.

Critical Impulse Drying Temperature: As in previous laboratory-scale experiments [2], critical impulse drying temperature was found to depend on the hydrodynamic specific surface of the heated layer of the sheet. As expected, critical impulse drying temperature was higher for the "low thermal mass" IPST "C" press roll than for the "higher thermal mass" Beloit "A" press roll. Interestingly, it was also concluded that the choice of felt influenced the critical temperature.

Press Dryness: For a given set of pressing conditions, press dryness tended to decrease when the hydrodynamic specific surface of the sheet increased. In addition, press dryness resulting from impulse drying was generally higher than that achieved by double-felted pressing. Differences in dryness ranged from 8 percentage points for sheets having low heated ply hydrodynamic specific surface to 3 percentage points for less permeable sheets. The Beloit "A" roll yielded higher press dryness than the IPST "C" roll, even though it was generally operated at lower temperature. While increasing the press load from 6000 pli to 8500 pli increased press dryness, the improvement was observed to be relatively small.

STFI Compression Strength: The Geometric mean STFI compression strength of impulse dried

sheets were consistently higher than that obtained by double-felted pressing. The difference in strength tended to be more significant for the more permeable sheet structures. For two-ply sheets, the STFI compression strength resulting from impulse drying was as much as 17 percent higher than that produced by double-felted pressing. No substantial strength difference was observed comparing sheets impulse dried with the Beloit "A" roll to those dried using the IPST "C" press roll.

Felt Water Chemistry: For an unexplained reason, using "hard" felt wash water tended to increased outgoing solids by up to about 3 percentage points. STFI Index, however was not influenced by water chemistry.

Speed Effects: Increasing machine speed results in decreasing the nip residence time from about 42 ms to about 32 ms. Decreasing residence time had the expected result of decreasing water removal and STFI compression strength for all furnishes.

Gurly Porosity: For all furnishes, the impulse dried sheets were less porous than double-felted pressed sheets, which in turn were less porous than the control sheets that were pressed to 52% solids.

Ink Penetration Test: The rate of change of the contact angle for black flexographic ink drops on the felt side of the samples were measured. The measurements were generally independent of furnish and method of pressing and were similar to measurements of commercial samples.

Sheet Surface Roughness: The roughness of the wire side of sheets was measured by Sheffield and Bentsen roughness tests. It was concluded that while the method of pressing and the extent

of refining control surface smoothness, the method of pressing was the dominant variable. In general, impulse dried samples were smoother than single-felted pressed samples, which were smoother than double-felted pressed samples.

ZD Tensile: The zd tensile strength is a measure of ply-bond strength. Impulse drying tended to increase zd tensile strength.

Burst Index: Impulse drying tended to increase burst strength as compared to double-felted pressing.

Cracking Angle: Cracking angle was found to be dependent on the level of refining of the fibers on the wire side of the sheet and the method of pressing. Refining was found to be the dominant effect, in that excessive refining leads to a low cracking angle. Impulse dried samples tended to have slightly lower cracking angles than double or single-felted pressed sheets. As impulse drying performs best when the heated ply (wire side) is not heavily refined, there should no problem in achieving acceptable cracking angle results in commercial practice.

Since the publication of the IPST member report [1], selected handsheets from the pilot experiment have been printed on a commercial flexographic printing press and evaluated for print quality. The results of those measurements are here reported.

Each of nine sheets was printed at the same conditions using undiluted, black, flexographic ink. The printed image consisted of at least one solid black region which could subsequently be analyzed for mottle. The images of all nine samples were digitized using a high resolution scanner and analyzed using, *Image 1.49* , an image analysis program [3] originally developed by the U.S. National Institute Of Health.

In this application, *Image 1.49,* was used to analyze the "unprinted" and "solid printed" areas of the sheet. For each area the normalized number of pixels having "gray scale readings" of 0 to 265 was determined. Here, a gray scale reading of 0 corresponds to white while a gray scale reading of 265 corresponds to black. From the gray scale frequency distributions, cumulative distributions were generated as shown in Figure 1 through Figure 9.

Figure 1 through Figure 3 characterize the printed and unprinted areas of two-ply sheets, furnish FD6, composed of a 740 ml CSF freeness virgin Kraft on the printed ply and a 50/50 blend of 740 ml CSF Virgin Kraft and 600 ml CSF OCC in the bottom ply. Figure 1 shows the double felted pressed case while Figure 2 and Figure 3 show single felted pressed and impulse dried cases respectively. The curves for the unprinted areas can be used to quantify the contrast of the black ink to the unprinted sheet, while the curves for the solid printed areas can be used to quantify mottle.

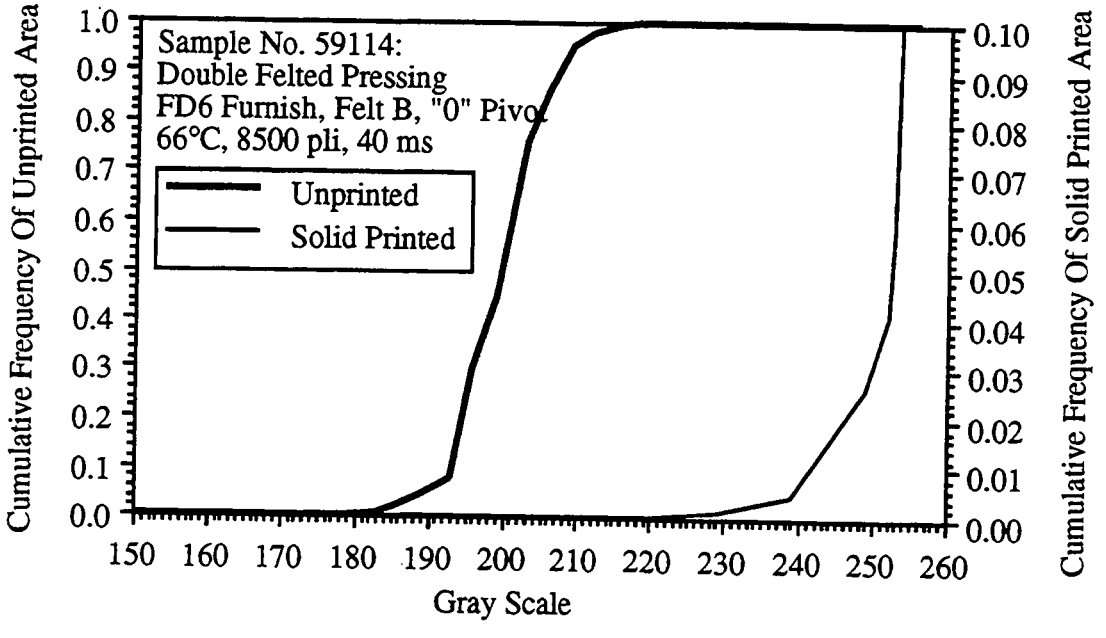

Figure 1. Cumulative frequency vs. Gray scale for printed and unprinted regions of a two-ply sheet which had been double felted pressed.

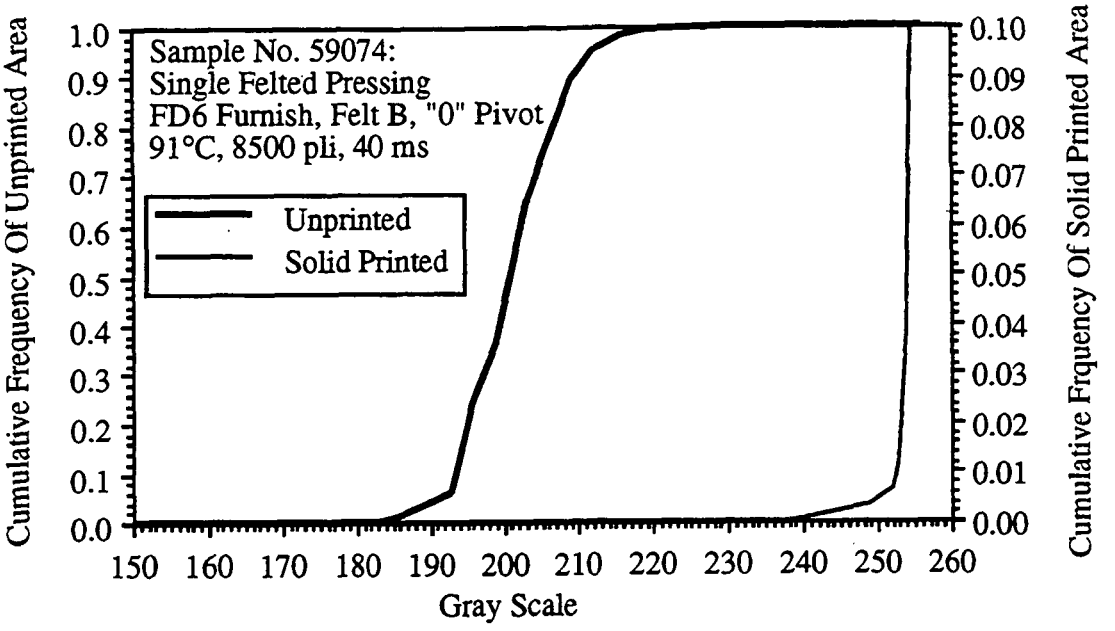

Figure 2. Cumulative frequency vs. Gray scale for printed and unprinted regions of a two-ply sheet which had been single felted pressed.

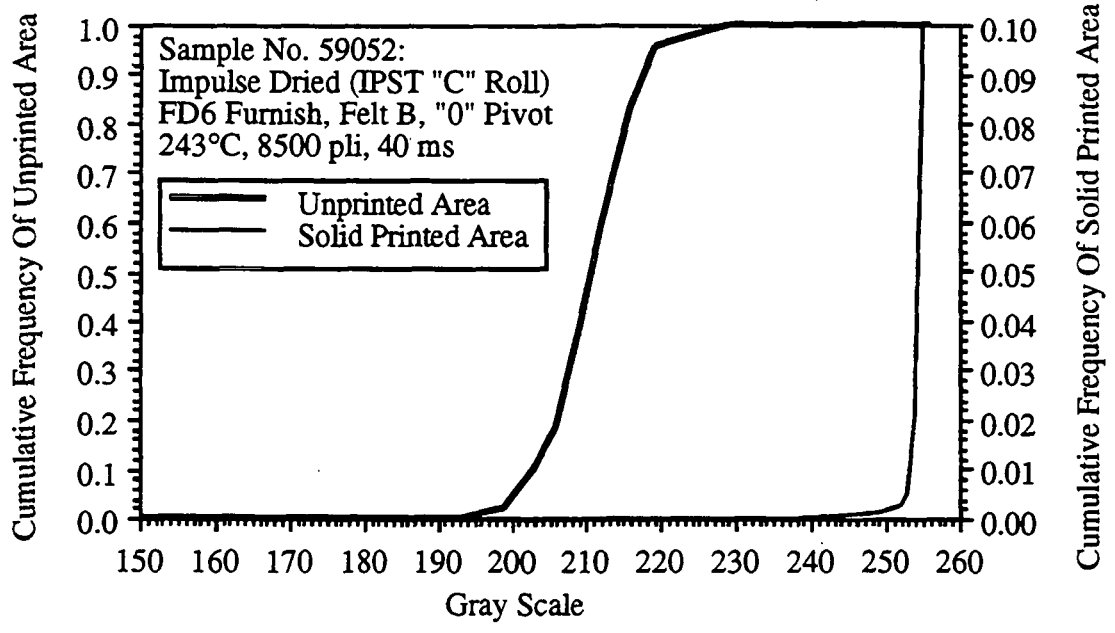

Figure 3. Cumulative frequency vs. Gray scale for printed and unprinted regions of a two-ply sheet which had been impulse dried.

Figure 4 through Figure 6 characterize the printed and unprinted areas of single-ply sheets, furnish FD5, composed of 450 ml CSF OCC. Figure 4 shows the double felted pressed case while Figure 5 and Figure 6 show single felted pressed and impulse dried cases respectively.

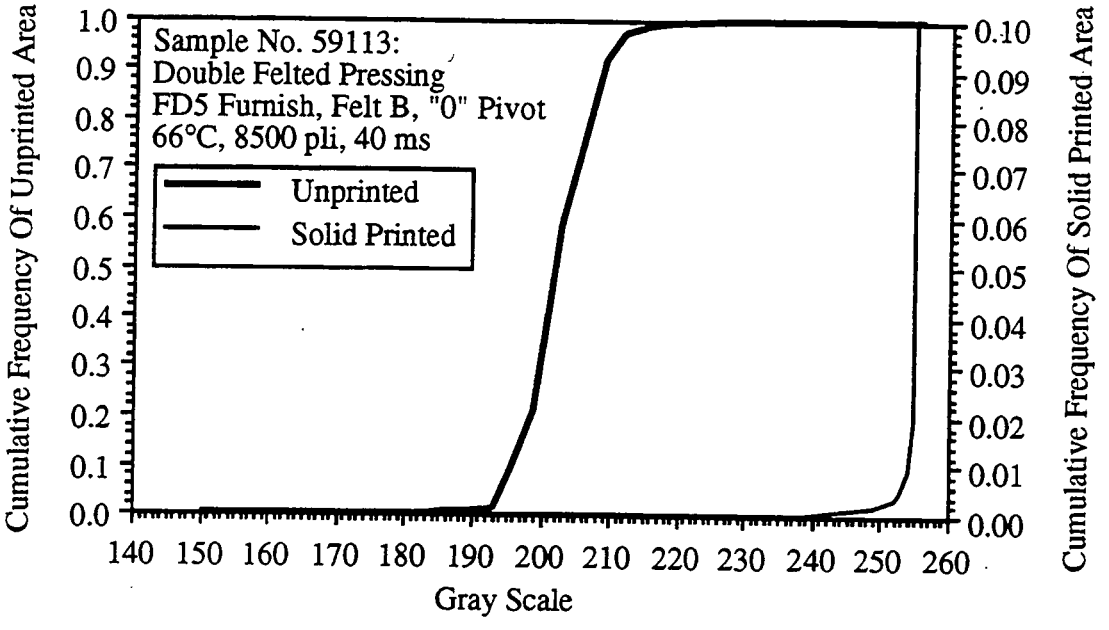

Figure 4. Cumulative frequency vs. Gray scale for printed and unprinted regions of a single-ply 100% occ sheet which had been double felted pressed.

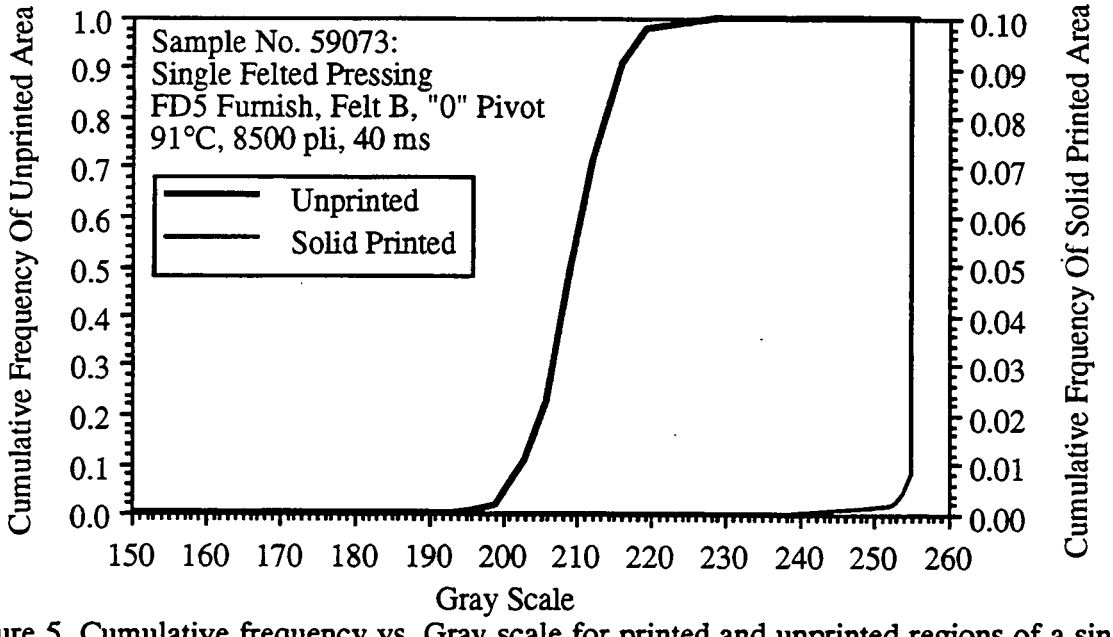

Figure 5. Cumulative frequency vs. Gray scale for printed and unprinted regions of a single-ply 100% occ sheet which had been single felted pressed.

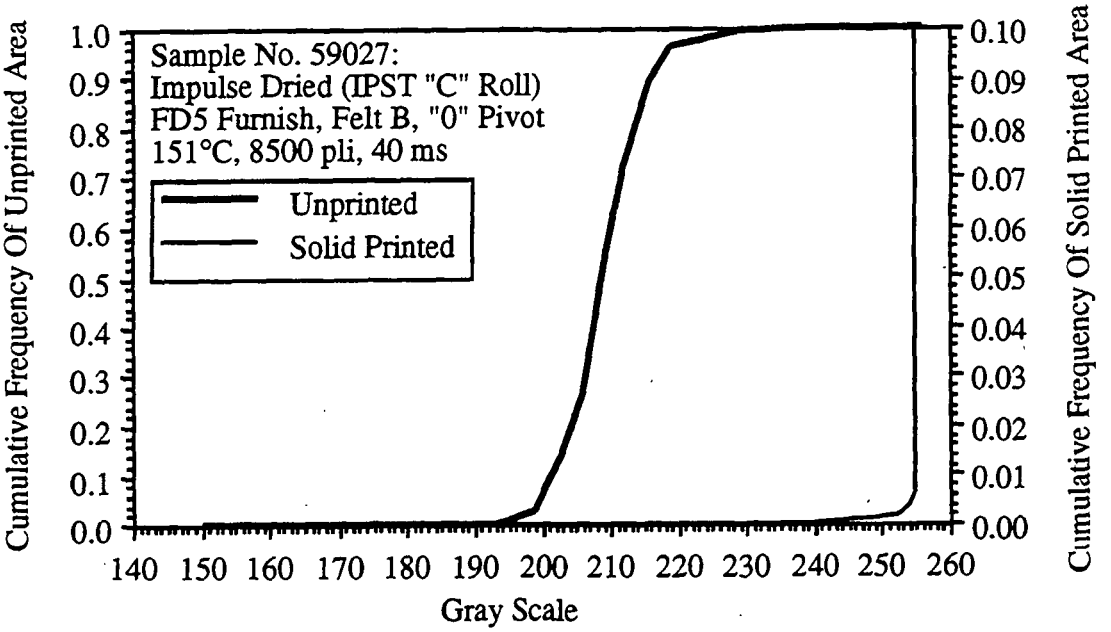

Figure 6. Cumulative frequency vs. Gray scale for printed and unprinted regions of a single-ply 100% occ sheet which had been impulse dried.

Figure 7 through Figure 9 characterize the printed and unprinted areas of single-ply sheets, furnish WF1, composed of 740 ml CSF Virgin Kraft. Figure 7 shows the double felted pressed case while Figure 8 and Figure 9 show single felted pressed and impulse dried cases respectively.

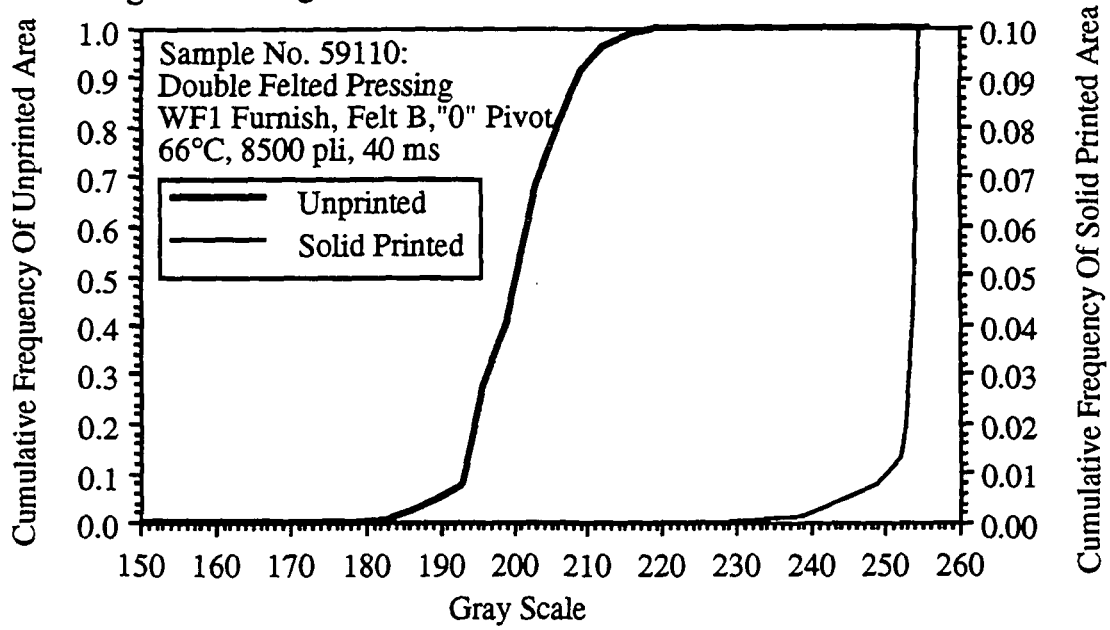

Figure 7. Cumulative frequency vs. Gray scale for printed and unprinted regions of a single-ply 100% virgin kraft sheet which had been double felted pressed.

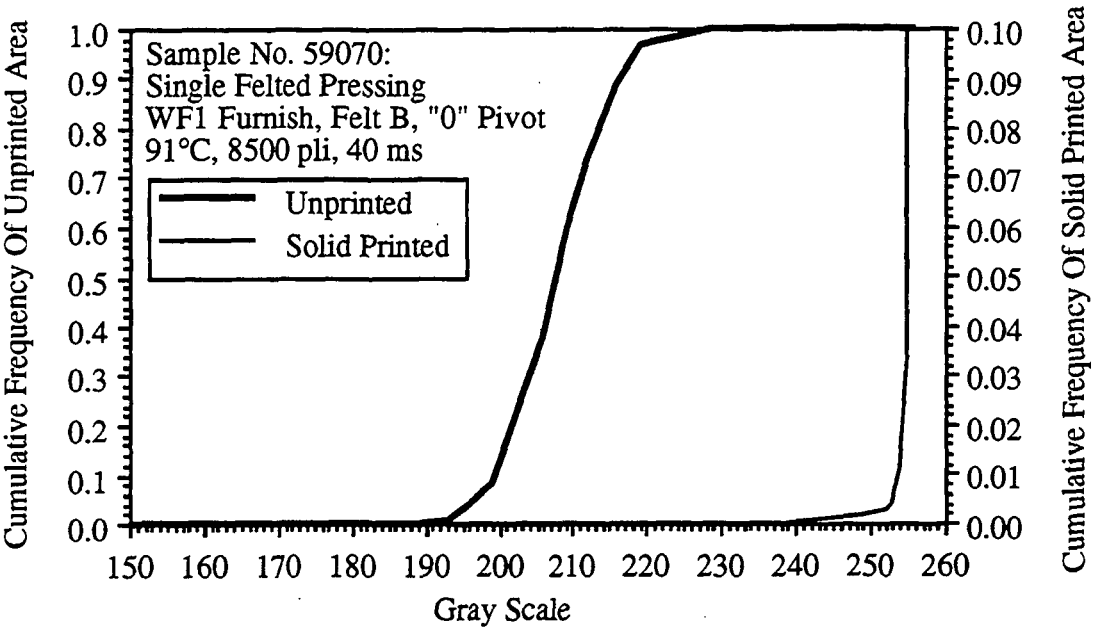

Figure 8. Cumulative frequency vs. Gray scale for printed and unprinted regions of a single-ply 100% virgin kraft sheet which had been single felted pressed.

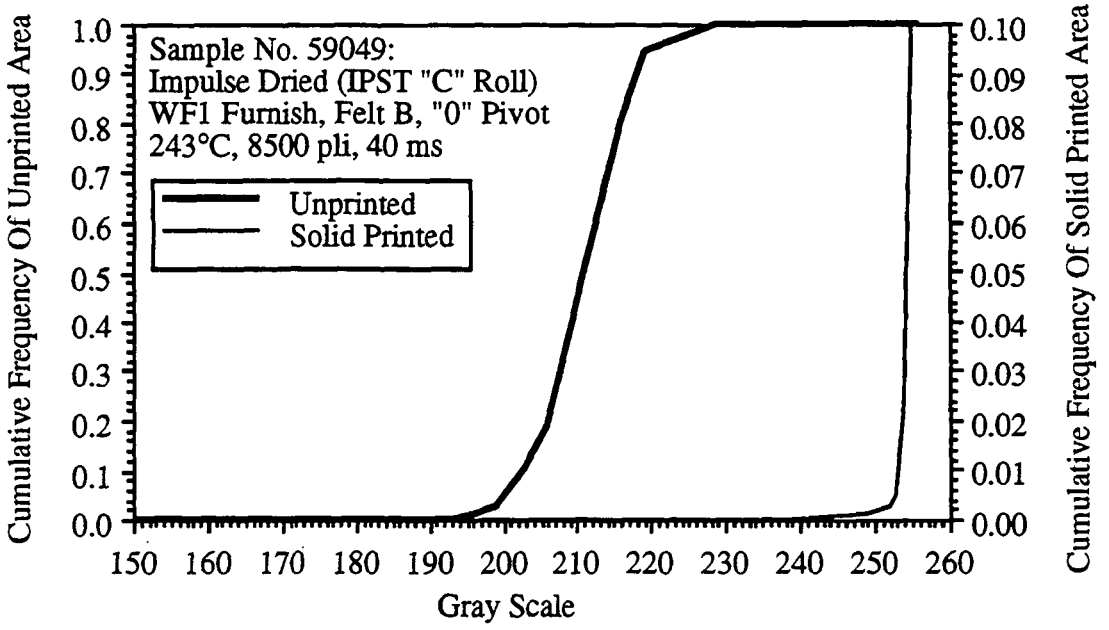

Figure 9. Cumulative frequency vs. Gray scale for printed and unprinted regions of a single-ply 100% virgin kraft sheet which had been impulse dried.

If we use the cumulative frequency of the solid area, at a gray scale of 252 as a yard stick, we can compare the relative mottle of the samples as shown in Table 1. Also shown in Table 1 is the corresponding most probable gray value of the unprinted areas, which should correlate to contrast between the ink and the sheet.

From Table 1, it is clear that double felted pressed sheets tended to have the worst mottle, while the mottle exhibited by impulse dried sheets was equal to or better than that exhibited by single felted pressed sheets. Impulse drying was observed to darken the sheet while double felted pressing lightened single-ply sheets and had little impact on two-ply sheets. As an observer will primarily evaluate sheet quality on mottle rather than contract, impulse drying is expected to positively impact print quality relative to double-felted pressing.

Table 1.

	FD6			FD5			WF1		
	DF	SF	ID	DF	SF	ID	DF	SF	ID
Cumm. Freq. (0 to 252)	0.041	0.006	0.002	0.003	0.002	0.002	0.013	0.003	0.003
Most Prob. Gray Scale of Unprinted	199	200	210	202	209	208	200	207	211

A Numerical Model Of A Proposed Controlled-Crown Impulse Drying Press Roll

Batch-pilot experiments at the Beloit Corporation have demonstrated that the IPST "C" ceramic roll coating is susceptible to shear failure when the roll operates at temperatures between 100°C and 150°C. Photomicrography of the failure zones, by Sandia National Laboratory, confirmed that these failures occurred when paper that had adhered to the roll was subjected to shear at the

doctor blade. While the Beloit "A" roll is intrinsically stronger, and did not experience failure, the issue of roll surface long term durability clearly requires further study. For this purpose an analytical modeling effort was initiated that will lead to the prediction of stress and temperature as a function of position and time in the various layers of a commercial impulse drying press roll.

As a first step in that analysis, a closed form model of lubrication and heat transfer at the boundary between the internal hydrostatic shoe and the inside of the roll shell was undertaken. The objective of the analysis was to predict pressure and temperature distributions at that interface. Once accomplished, these distributions will act as boundary conditions to a finite element model of the varied layer press roll.

A detailed discussion of the lubrication part of the model is given in an IPST Member Report [4], while publication of the heat transfer part of the model should occur by May 1994. In this report, some of the key results of the lubrication model are discussed.

Figure 10 shows a schematic of the proposed commercial-scale impulse dryer. The sheet, on special felt, enters the extended nip of the impulse dryer at location A. The specially coated roll shell, heated by induction heating in region D - E contacts the sheet at a surface temperature in the range of 150 to 250°C. Steam formed at the interface between the roll shell and the sheet increases the hydraulic pressure gradient, and the mean sheet temperature thereby reducing the viscosity of water in the sheet and increasing the conformability of the heated fibers. These effects tend to increase water removal, increase the density of the heated surface and apparent density of the sheet and thereby increase the strength of the sheet.

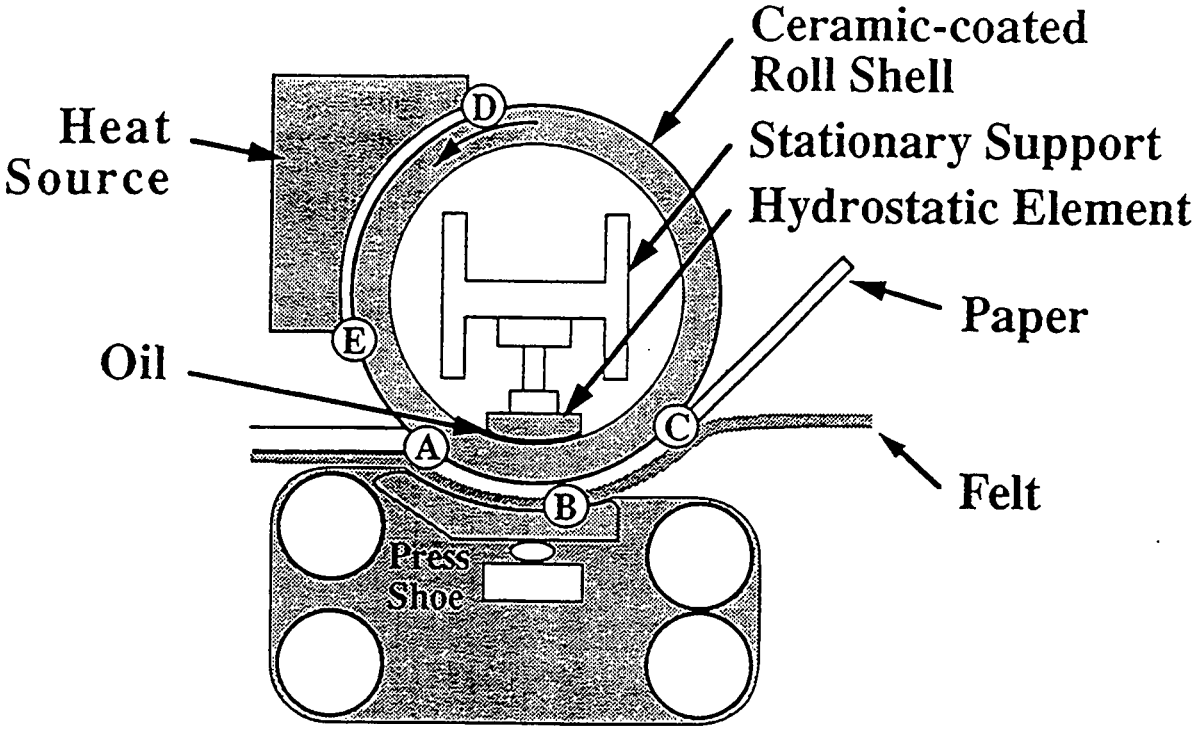

Figure 10. Schematic of a crown-compensated impulse dryer

A more detailed cross section (Figure 11), shows that the hydrostatic element acts as a piston in the cylinder formed by the internal walls of the stationary support (or central shaft). Cool pressurized oil is pumped, from outside the impulse dryer, to the space between the piston (hydrostatic shoe) and the cylinder (stationary center shaft) where it enters capillaries that feed recesses in the hydrostatic shoe. Oil exits the recesses to transmit load and provide lubrication between the stationary hydrostatic shoe and the rotating roll shell.

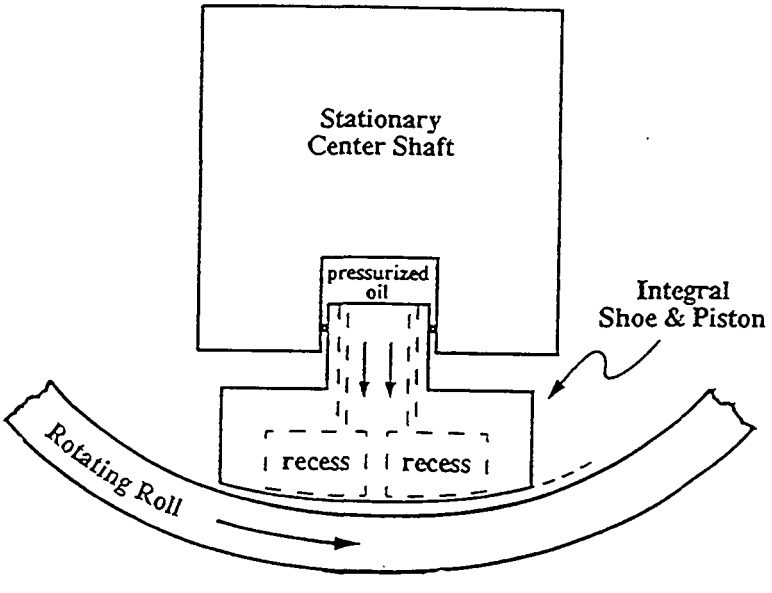

Figure 11. A schematic cross section of the hydrostatic shoe and rotating roll shell.

Within certain limits, the hydrostatic shoe is free to "rotate" through an angle, ψ, as a consequence of the oil pressure in the space between the piston and the cylinder and the shear and normal forces exerted on the bottom of the shoe by the oil flowing between the stationary shoe and the rotating shell. Figure 12 shows the geometry of the problem, where it has been assumed that the radius of the shoe is equal to the internal radius of the shell. The following additional assumptions have been made in the process of developing the model.

1. The shoe was assumed to "rotate" about its center point $(0, R+ d_0)$
2. Flow from the capillaries was assumed to be uniform flow entering into each channel at a point.
3. Flow in each channel was considered to be steady, laminar, with constant viscosity and density.
4. All geometric and flow variations along the width of the roll in cross direction were assumed to be negligible.
5. Elastic deformation of the roll was ignored.

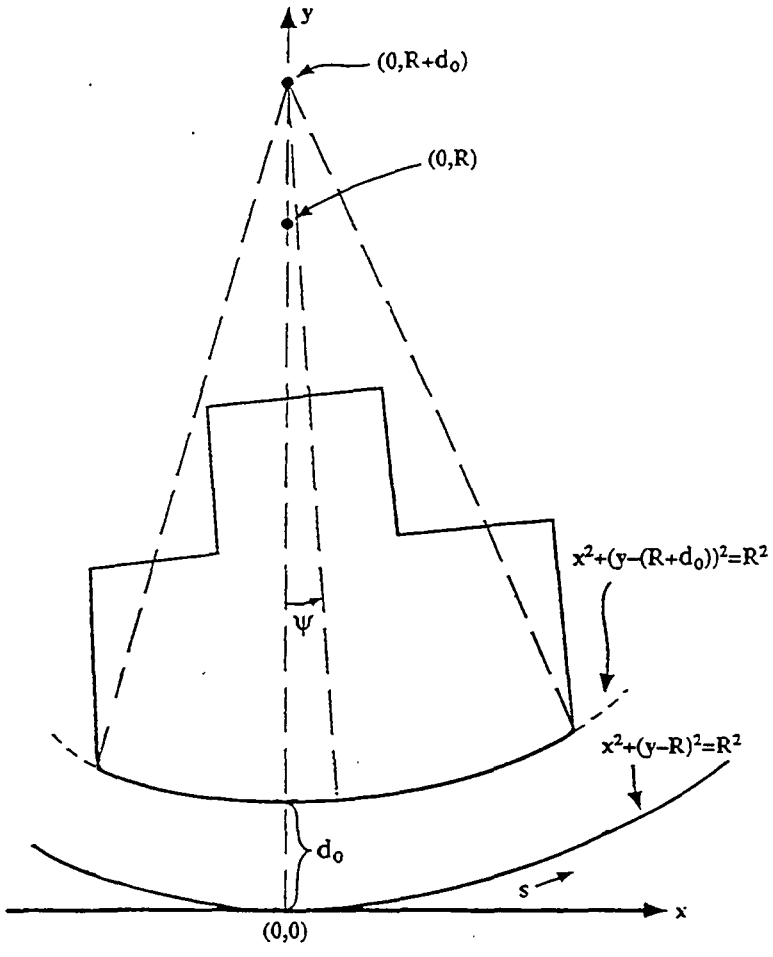

Figure 12. Geometry defining the motion of the shoe.

Approximating the curved channel between the shoe and the shell by a two-sided convergent planer-wall channel allows a closed form solution to the lubrication and heat transfer problem. In the right-hand and left -hand channels the lubricant was assumed to have the following velocity and pressure profiles: $u = u(x,y)$, $P = P(x)$, while in the center channel, $u = u(y)$ was considered.

At steady state, the hydrostatic shoe will be in static equilibrium with the various forces on the shoe being in balance. It is expected that the angle, ψ, will be influenced by; the load applied to the top of the shoe, the speed of the shell relative to the stationary shoe, and the viscosity of

the oil. Assuming an oil viscosity of 187 centipoise, the angle, ψ, may be predicted as shown in Figure 13. Note that a positive angle implies that the shoe turns in the direction of rotation of the shell.

Figure 13 shows that the angle of rotation increases with increased roll speed and with increased load. The figure also shows that the shoe is exceptionally stable to changes in load and speed as long as the load exceeds 438 KN/m (2500 pli).

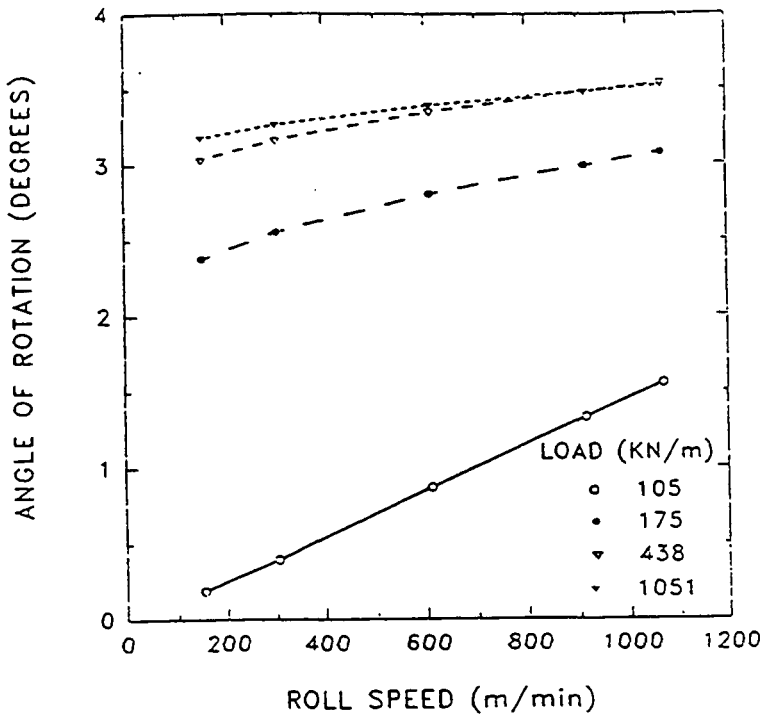

Figure 13. Angle of "rotation" of the hydrostatic shoe as a function of roll speed and applied load.

For the purpose of discussion, the "leading edge" of the shoe is defined as that side of the shoe that first experiences the roll shell as it rotates in the counterclockwise direction. Likewise, the "trailing edge" of the shoe is that side of the shoe that last experiences the rotating shell. Figure 14 shows the base oil film thickness, leading edge oil film thickness and trailing edge oil film thickness vary as functions of load and roll speed for the previously assumed oil viscosity.

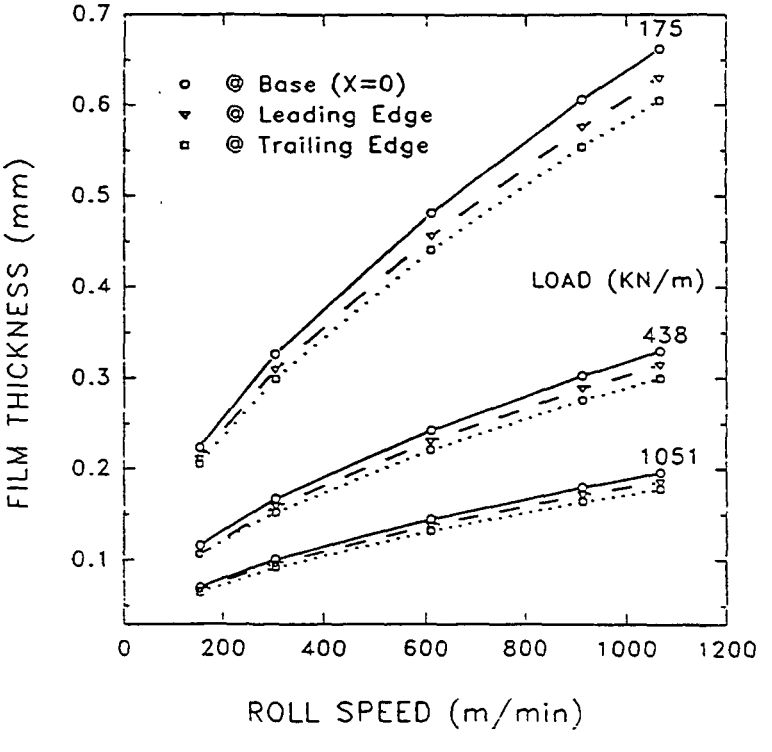

Figure 14. Base, leading edge and trailing edge oil film thicknesses as functions of applied load and roll speed.

It is observed from the figure that two channels are always converging and that the leading edge oil film thickness is always greater than the trailing edge oil film thickness. It is also observed that the oil film thickness decreases with increasing load and increases with increasing roll speed. This later effect may at first seem strange, until it is recognized that the shoe is acting like an air foil, whose lift increases with airfoil speed.

Based on the assumed oil viscosity and capillary dimensions, the volumetric flowrate of the lubricating oil may be predicted as shown in Figure 15. Lubricating oil requirements increase with increasing roll speed but decrease as the applied load is increased. An oil flowrate of 85 liters/min·m would be required at a roll speed of 610 m/min (2000 fpm) at an applied load of 1051 KN/m (6000 pli).

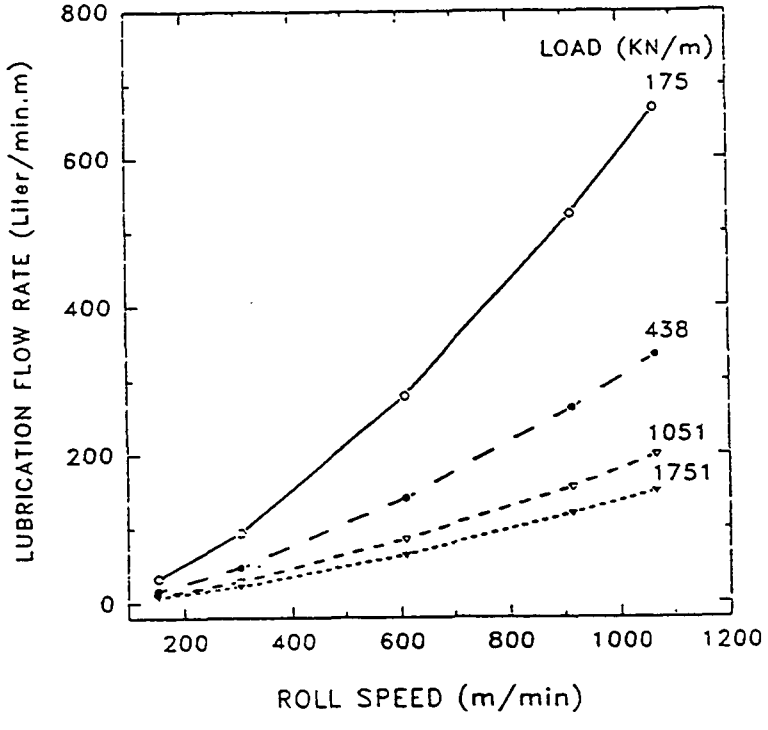

Figure 15. Volumetric flowrate of lubricating oil as a function of roll speed and applied load.

A major objective of the lubrication model is to predict the pressure (normal force) distribution applied by the oil on the inside surface of roll shell. Modeling demonstrated that the pressure distribution was insensitive to roll speed. Figure 16 shows the pressure distribution as a function of applied load. It is noted that the right channel (ending with the trailing edge) applies a much higher load to the shell than the left channel.

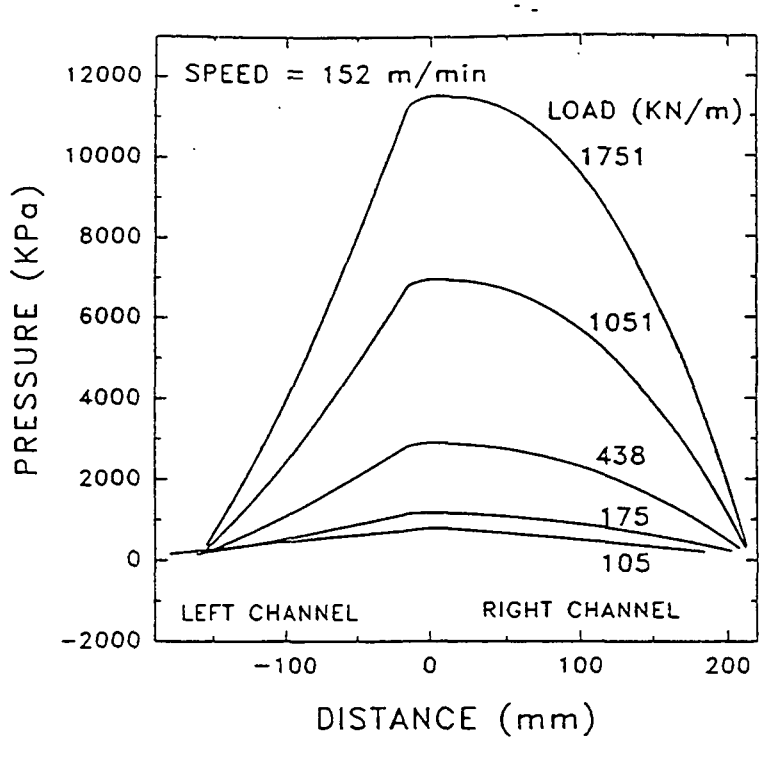

Figure 16. Pressure distribution as a function of applied load.

Solution of the heat transfer problem requires the prediction of velocity profiles in the right and left converging channels. The model was used to show that the velocity profiles are relatively similar at various locations in each of the channels. The model also shows that at sufficiently high speed and load, oil flows from the leading edge and from the recesses to the trailing edge. Hence, the design must include a source of cool oil at the leading edge and at the recesses as well as a sink for heated oil at the trailing edge.

The power required to drive the roll was also estimated. Here it was assumed that the only friction in the system was that between the shoe and the shell. Hence, bearing friction was neglected. Figure 17 shows the calculated power as a function of roll speed and applied load. As expected, it was observed that the required input power increased with both roll speed and applied load. Note that at a speed of 610 m/min (2000 fpm) and a load of 1051 KN/m (6000 pli) the power was 121 KW/m (49.5 hp/ft). Hence, an electric motor having in excess of 1624 hp would be required to operate a 10 m (394 in) wide crown-controlled press roll.

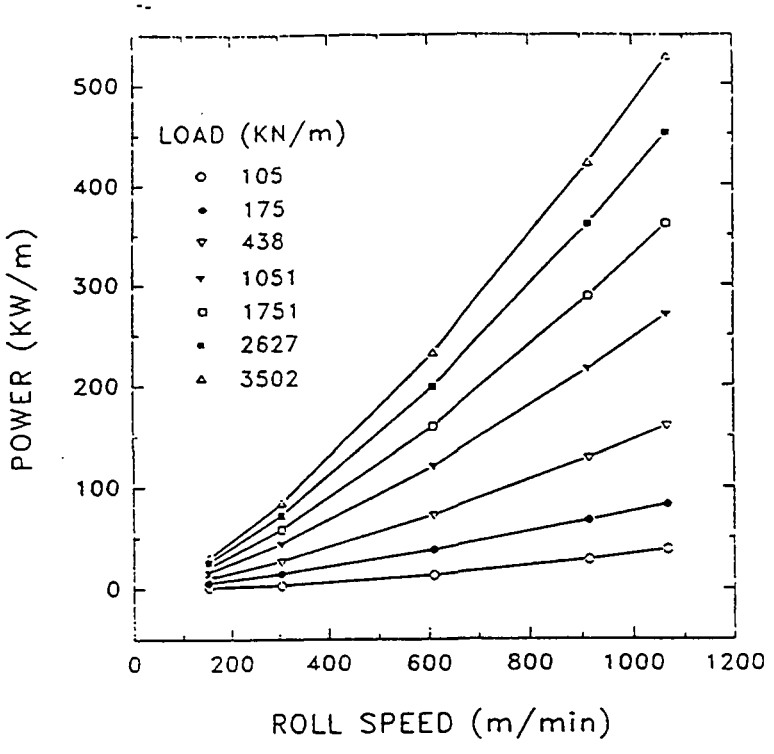

Figure 17. Estimated minimum mechanical power to operate the press roll as a function of roll speed and applied load.

Design Of A High Speed Press Roll Durability Test Stand

Through a grant from the Electric Power Research Institute, the Institute is currently designing a modification to the existing pilot impulse dryer to allow it to function as a press roll durability test stand. Current plans call for removing the second nip and installing the induction heater on the first nip in place of the infrared heater. With some additional drive changes, this will allow the pilot unit to operate at speeds of 2500 fpm.

Once designed, a grant from the U.S. Department of Energy will fund the construction, instrumentation and operation of the durability test stand. In operation, a steel roll will be coated with as many as three test coatings in 3 inch wide CD bands. The coated roll will then be heated by induction to a surface temperature of 250°C. The roll will be driven at 2500 fpm and loaded against a felt that has been saturated with water to provide a heat sink similar to that provided by paper in impulse drying. The roll surface will be continuously monitored by infrared thermography to detect the onset of surface flaws in the coating. In addition the state of strain on the roll surface will be measured using three dimensional speckle interferometry. These surface strains will then be used with experimental stress-strain data to determine surface stresses. Experimental surface stresses will then, in turn, be compared to the predictions of the finite element model.

Interdependency Of "Thermal Mass" And Press Impulse

Laboratory experiments were conducted to determine the interdependency of the "thermal mass" of the heated press roll surface and press impulse on impulse drying performance. Process conditions were chosen that were similar to the conditions used for the Beloit batch-pilot

extended-nip shoe press experiments [1], providing laboratory confirmation of the results. The IPST "C" surface coating and an alternate coating IPST "A" were used as well as a mild steel IPST "S" surface for contrast, all platens had surface thermocouples to record energy transfer. Each surface coating was tested at a constant dwell time of 40 ms at press loads of 6000, 7500, and 9000 pli using extra sheets of furnishes FD5 and FD6, left over from the Beloit trials.

Table 2 shows K (thermal mass) values for all three platens at different temperatures.

Table 2. "Thermal mass" values for each coating type

Temperature (∞C)	IPST "A"	IPST "C"	Mild Steel
100	3260	1973	7211
200	3619	2050	7729
300	3949	2084	8178
400	4633	2091	8624

It was expected that lower "thermal mass" would result in higher critical temperatures with lower energy transferred to the sheet. The IPST "A" coating was expected to have critical temperatures, outgoing solids and energy transfer values between the IPST "C" and IPST "S" coatings. Previous work had shown a pressure dependence for energy transfer a similar mild steel platen, but very little pressure dependence for the ceramic coating. The previous results were obtained with an eroding probe-type thermocouple for the mild steel case. The present work, utilizing similar vacuum deposited surface thermocouples, for all platens, was designed to confirm and extend previous work to higher pressures and to contrasting sheet structures.

Figure 18 shows, as expected that critical impulse drying temperatures were substantially higher

for FD6 sheets having hydrodynamic specific surface of 1.3 m^2/g than for FD5 sheets having hydrodynamic specific surface of 10.5 m^2/g. The figure also shows, as expected, that use of platens with lower "Thermal Mass" resulted in higher critical temperatures. In addition, the figure shows that for the FD6 sheets, increased press loading increases critical temperature until a maximum was reached at about 8000 pli.

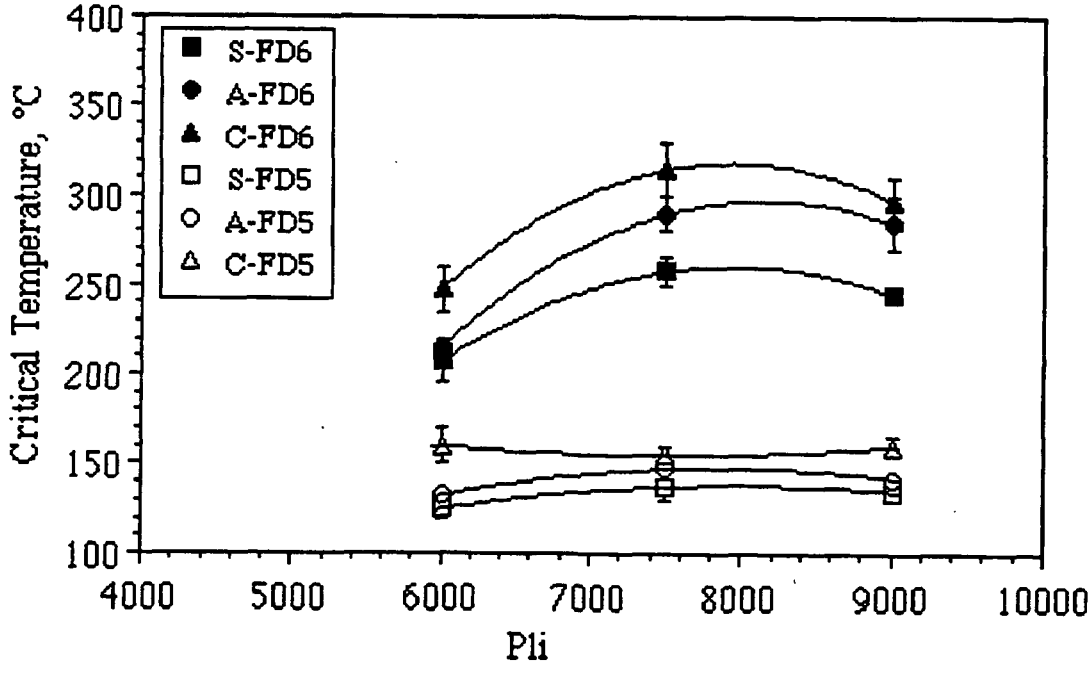

Figure 18. Critical Impulse Drying Temperature As A Function Of Pli

As of the writing of this report only limited outgoing solids data is available, as show in Figure 19. The figure, suggests that even though the IPST "C" roll operated at higher temperature than the IPST "A" surface, outgoing solids were higher for the IPST "A' case than the IPST "C" case. For the IPST "A" surface, outgoing solids was highest at the highest press load of 9000 pli, while the IPST "C" surface yielded maximum outgoing solids at about 8000 pli.

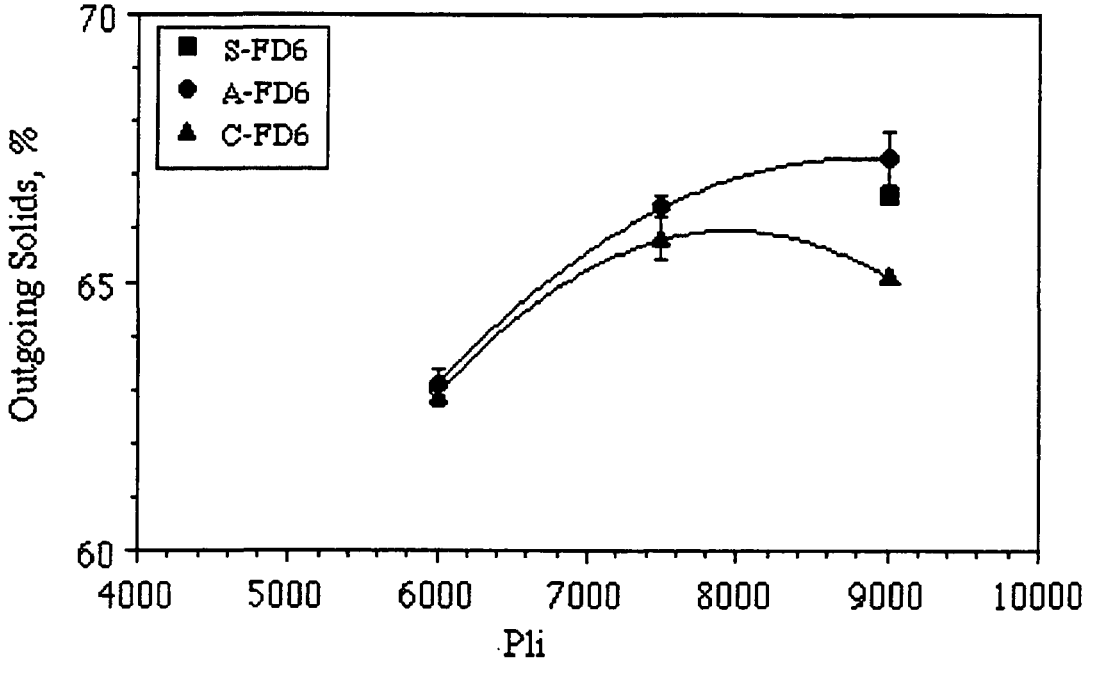

Figure 19. Outgoing Solids As A Function Of Pli

Figure 20 confirms that the IPST "C" roll surface is relatively independent of press load, while the IPST "S" roll surface is highly dependent on press load. Unfortunately, we do not have sufficient energy data for the IPST "A" surface to show its press load dependency. It is interesting to note the similar sheet impulse dried at the same impulse but with different press roll surfaces delaminated at different amounts of energy transfer. This suggests that we need to examine differences in the density and permeability of the pressed sheets to explain this. At the time of this writing, we have initiated these measurements.

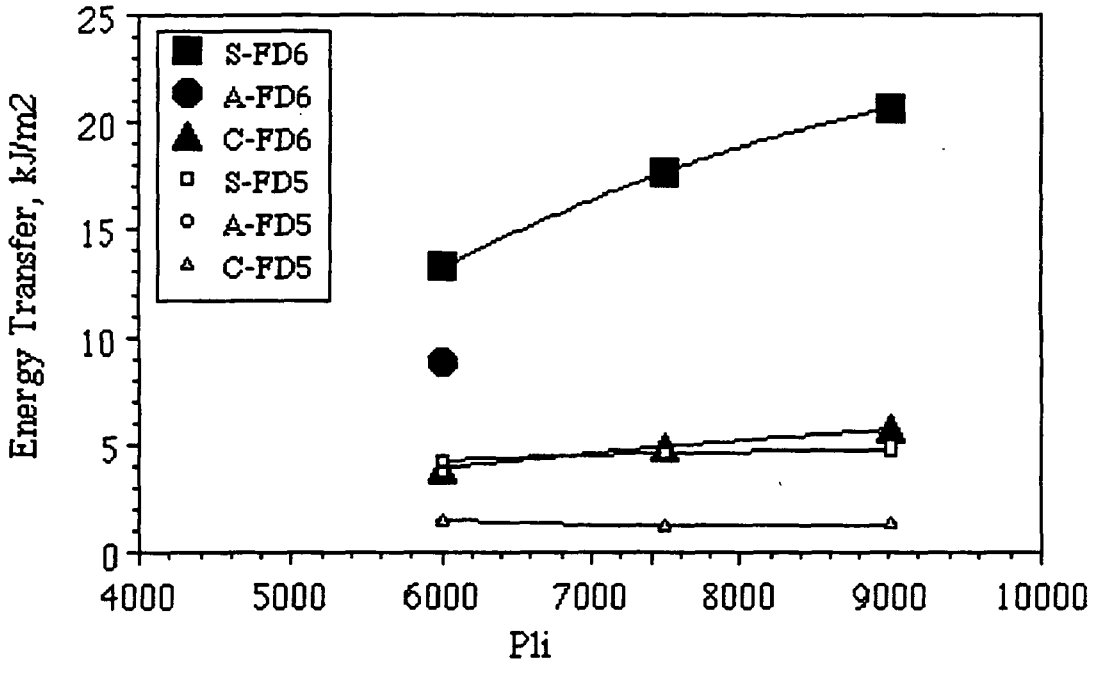

Figure 20. Energy Transfer To The Sheet During Impulse Drying As A Function Of Pli

Figure 21 presents zd- specific elastic modulus data for the present experiments. It was observed that maximum sheet strength was obtained by impulse drying with the IPST "C" surface for the FD6 sheet and with the IPST"A" surface for the FD5 sheet. The IPST "S" surface was consistently lower in strength. Additional physical property data, including STFI compression strength will be reported at the PAC meeting.

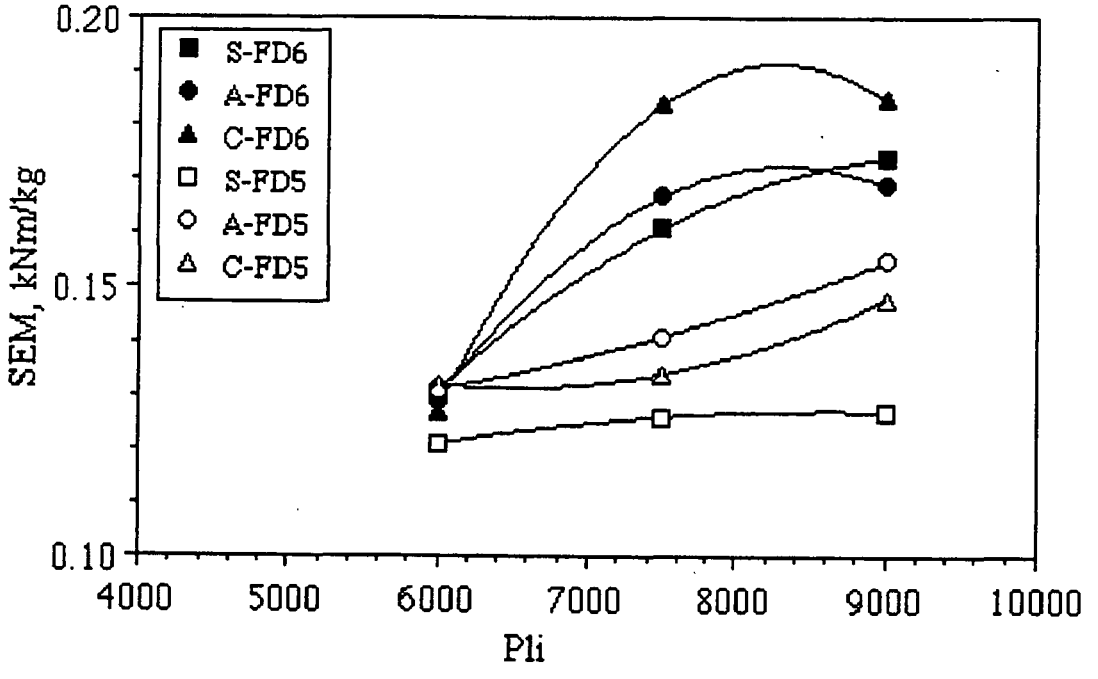

Figure 21. zd- Specific Elastic Modulus As A Function Of Pli

Figure 22 shows the ratio of water removed to energy transfer during impulse drying as a function of press load. The data confirms, that the IPST "C" roll surface results in more water removal for a given amount of energy transfer to the sheet.

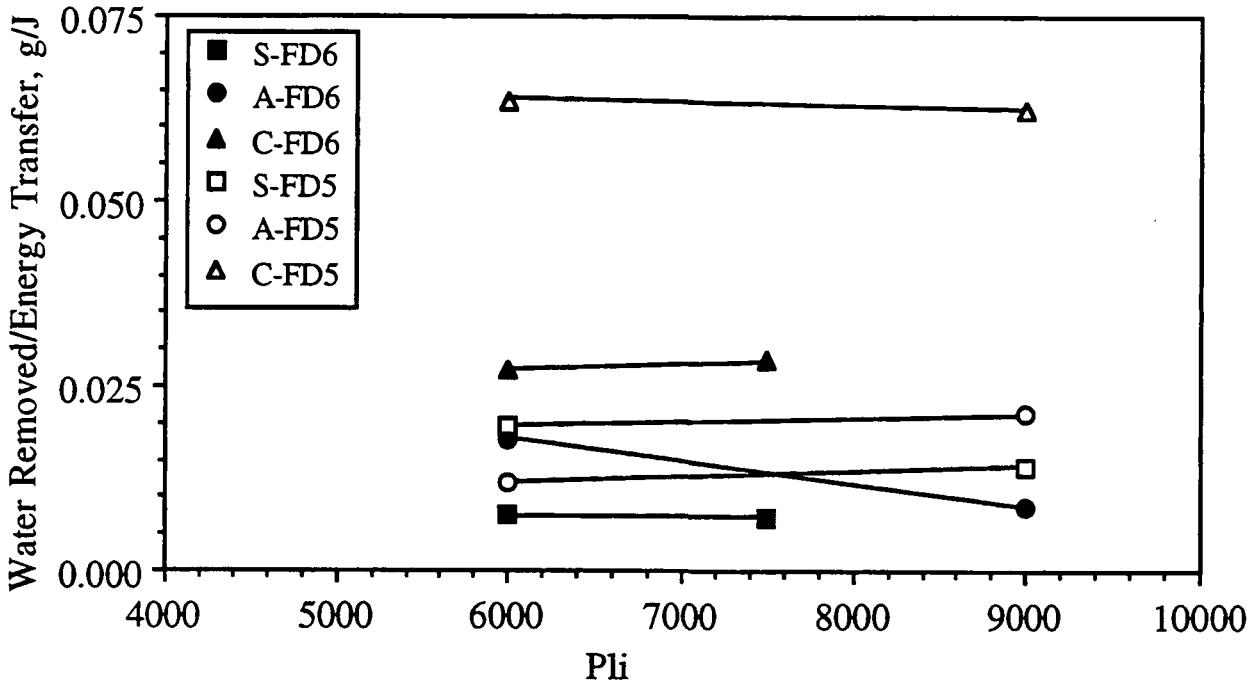

Figure 22. The Ratio Of Water Removed To Energy Transferred As A Function Of Pli

Heat And Mass Transfer To A Sheet During Steam Box Operation

Previous experiments strongly indicate that impulse drying performance is maximized when the sheet has been preheated as close to 100°C as possible. To ensure optimum performance of impulse drying, as well as conventional pressing, steam boxes may be used to preheat paper webs. Review of the literature suggests that there are no published heat and mass transfer correlations that would allow the accurate sizing of steam boxes. In addition, there appears to be some disagreement as to the relative benefits of various commercial designs and operating conditions. In addition, there is little data available to help in predicting the performance of steam boxes when sheet structures (permeability) are modified.

To help address these needs, two student projects have been initiated. Mr. Mark Strand will

develop instrumentation to measure temperature profiles, while Ms. Donna Cansler will develop instrumentation to measure moisture profiles, through sheets traversing under pilot steam boxes at commercial speeds. The apparatus to accelerate and decelerate an instrumented paper web under an instrumented pilot steam box is shown in Figures 23 and 24.

At the writing of this report, the apparatus has been designed and is in the process of being constructed.

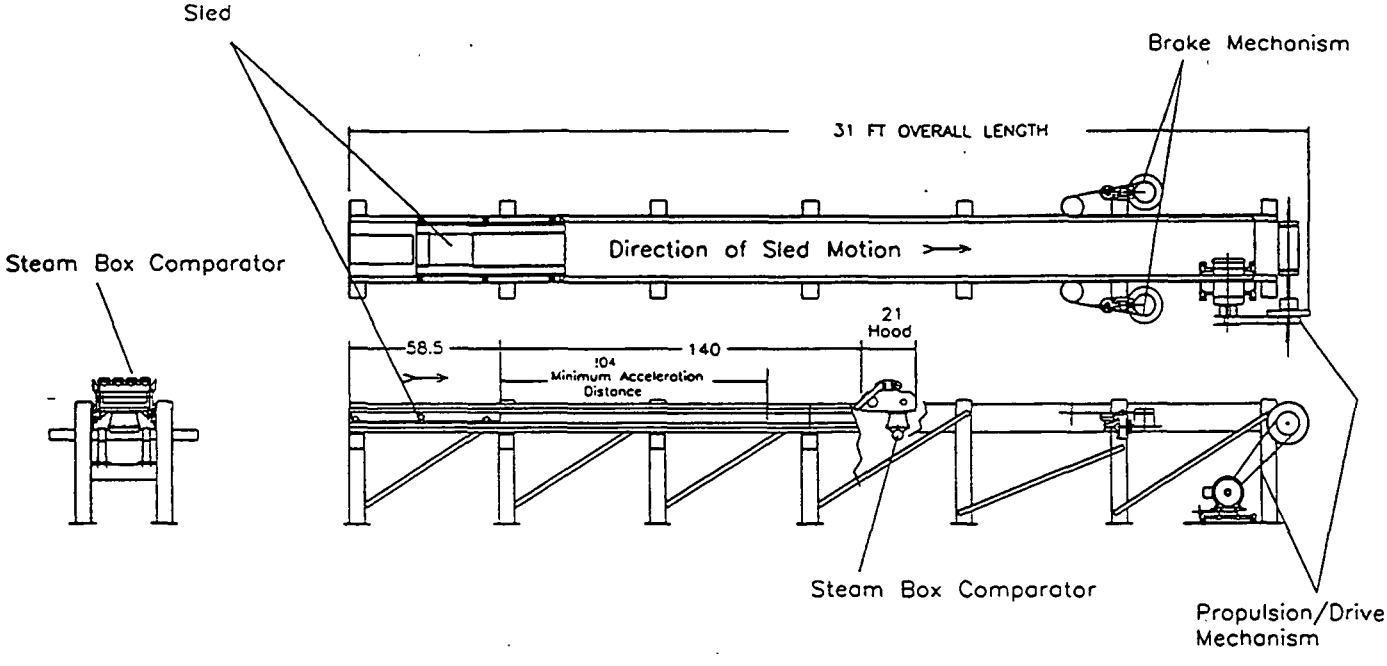

Figure 23. The IPST steam box comparator - "rocket sled"

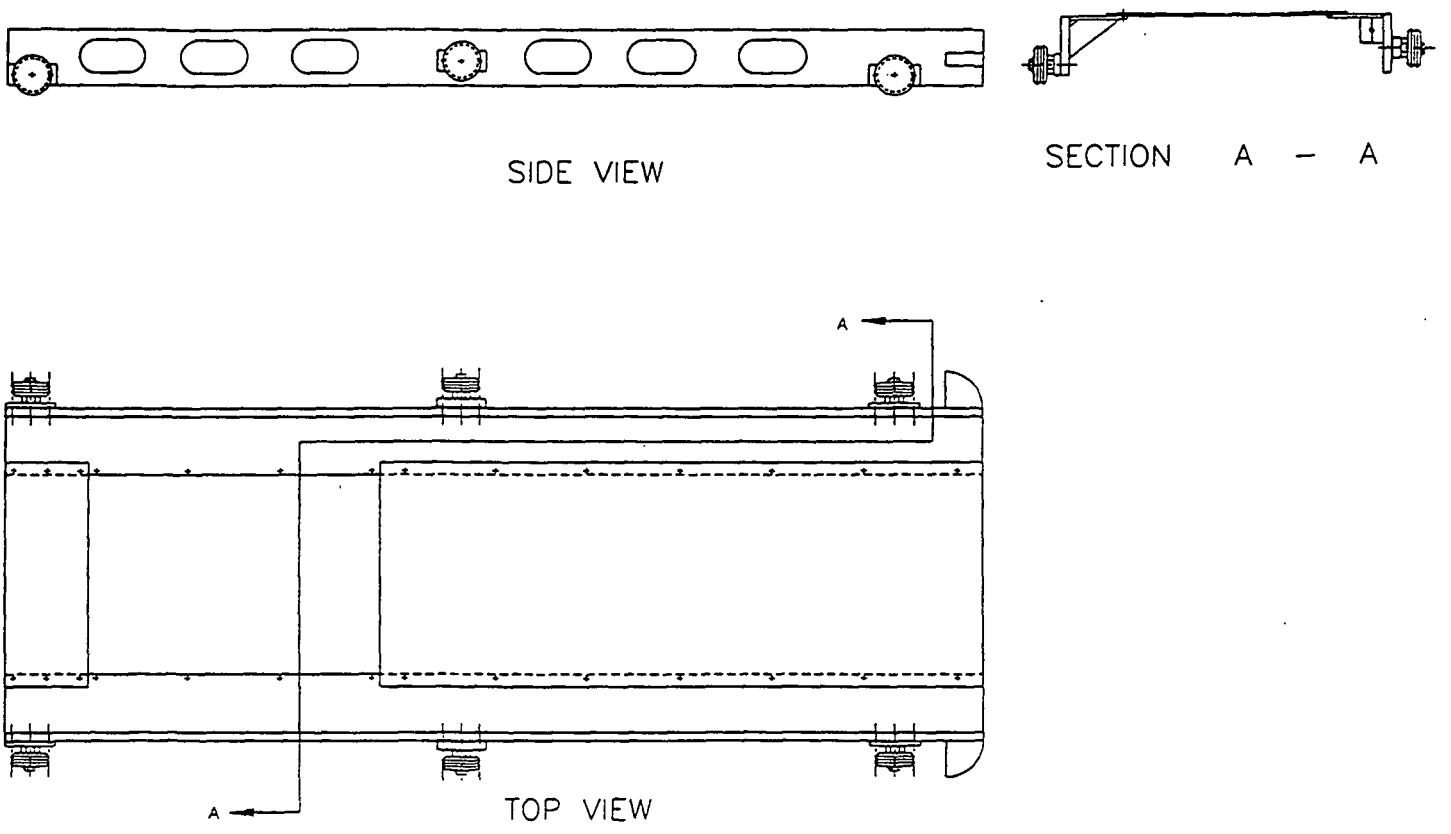

Figure 24. The sled used to hold instrumented handsheets

he Effect Of Nip Opening Pressure On Flash Evaporation And Sheet Delamination.

Previous work has suggested that sheet delamination occurs when sub cooled water (at high pressure and at temperature above the ambient boiling point, in the sheet flashes to vapor when the nip opens to ambient pressure. To rigorously test this hypothesis, a student project has been initiated to impulse dry sheets at "ambient" pressures well above atmospheric pressure. Mr. Andy Krause will conduct these experiments. Figures 25 and 26 show the experimental apparatus that Mr. Krause will use.

The device consists of four main elements; the pressure piston, the pressure cylinder, the pressure chamber cap, and the mounting plate/radiator. The mounting plate and pressure chamber cap are

bolted to the pressure chamber. The cap has an o-ring to maintain the pressure inside the cylinder. The mounting plate has additional bolt holes so it may be attached to the piston of the MTS electro-hydraulic press. When mounted on the MTS the mounting plate, pressure cylinder cap, and pressure cylinder (pressure cylinder assembly) have the orientation of an upside down cup. The pressure piston is bolted in a position directly below the MTS press piston. When the press piston with attached pressure cylinder assembly is lowered, the assembly slides over the pressure piston forming a closed chamber.

The primary function of the mounting plate/radiator is to provide the means to attach the pressure cylinder assembly to the MTS. However, a modified plate which incorporates cooling fluid channels and connectors can also be used. The purpose of the modified plate is to make it possible to rapidly cool the heated platen. This capability makes it possible to investigate the cooling of paper after it is impulse dried, reducing or eliminating the requirement for the pressure cylinder. This type of investigation would be pursued after the delamination mechanism is proven correct or incorrect.

The heated platen used for impulse drying is mounted on the under surface of the pressure chamber cap. Since the cap is removable, the platen can easily be changed. This allows the use of different platen materials and the possibility of pursuing investigations which are more in depth than the basic initial experiment.

Mounted at the base of the pressure cylinder is a steaming ring. It performs the same function as a steam box on a roll press. The pressure cylinder also houses two heat shields. The shields are moved using pneumatic cylinders mounted externally to the pressure cylinder. O-rings on the

pneumatic cylinder shaft maintains the chamber pressure. The purpose of the heat shields is to block the radiant heat of the heated platen after the impulse drying is complete, but before the chamber pressure is reduced to ambient pressure.

In operation, the pressure cylinder assembly is first positioned so that the steaming ring is at the same height as the lower platen. At this time the heat shields are positioned to cover the cylinder opening and the paper is steamed. The pressure cylinder is then positioned so that the lower platen is directly below the heat shields. In this position the chamber is sealed. Using an external high pressure nitrogen tank the chamber pressure is brought to the desired level. This requires an extremely short time period as the volume is so small. The heat shields are then retracted and the two platens brought into contact to begin impulse drying. When impulse drying is complete, the cylinder assembly is immediately positioned so that the lower platen is below the heat shields which are then moved over the cylinder opening. When the internal paper temperature is low enough the cylinder assembly is completely raised and the paper sample removed.

Note that the pressure piston has an o-ring to maintain the chamber pressure. The pressure piston also has an electrical connector allowing the use of paper samples containing thermocouples and other sensors.

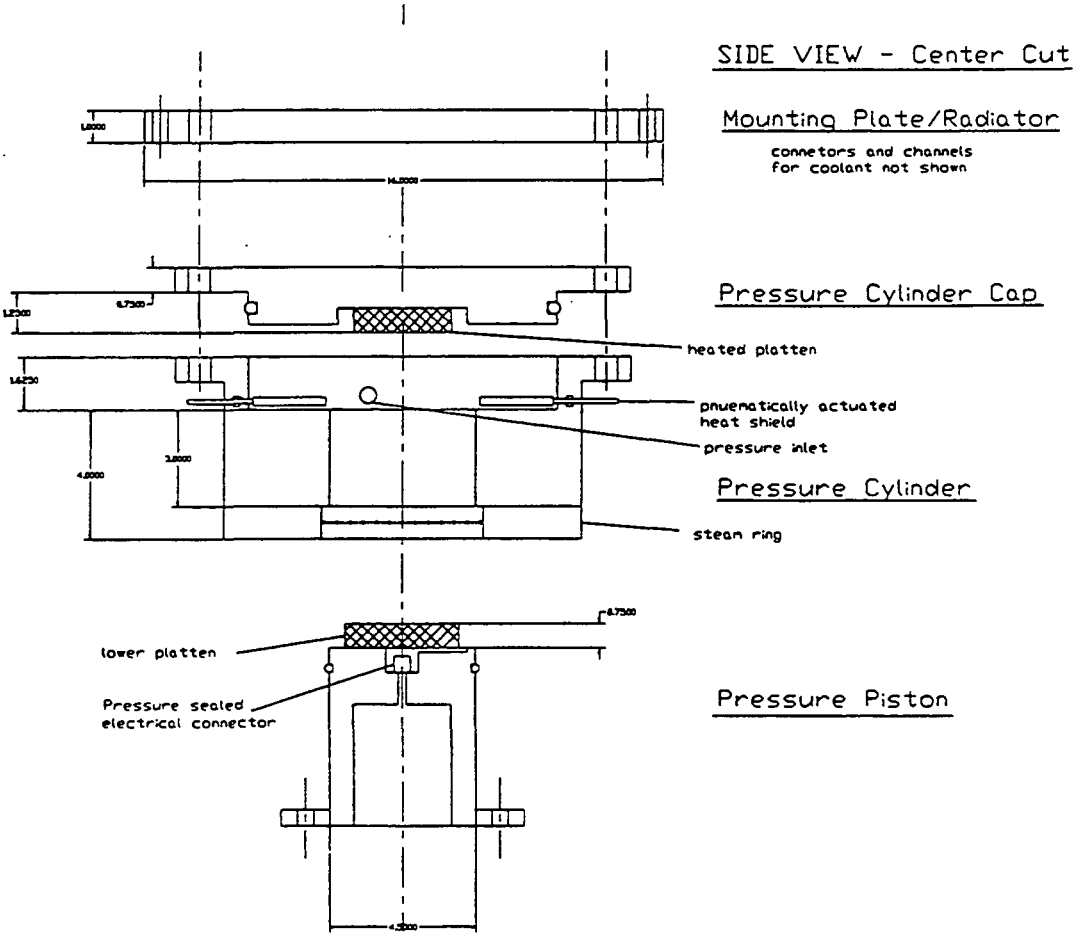

Figure 25. A side view of an apparatus to determine the effect of ambient pressure on sheet delamination during impulse drying.

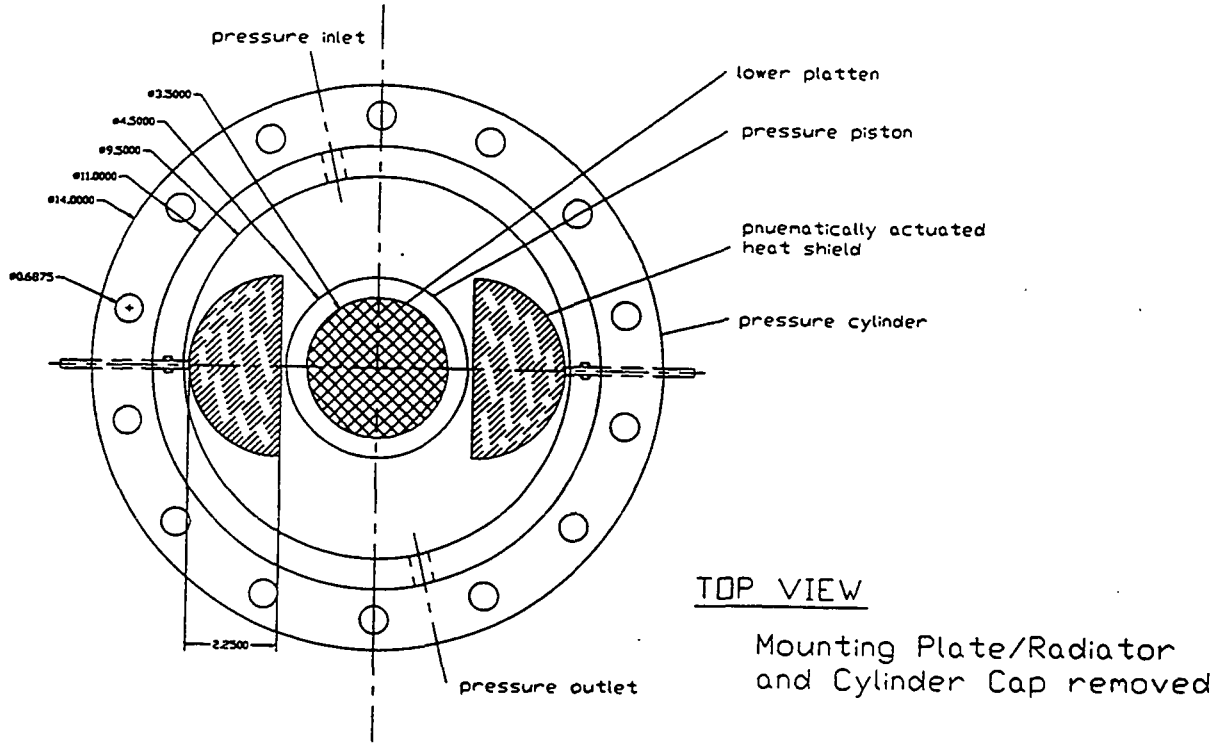

Figure 26. A top view of an apparatus to determine the effect of ambient pressure on sheet delamination during impulse drying.

GOALS FOR FY: 1994-1995

The ultimate objective of the impulse drying program is the commercialization of the technology for heavy weight grades of paper, such as linerboard. To accomplish that objective the Institute will complete the formation of the joint venture to commercialize impulse drying. Once formed, and funded by DOE, the Institutes dues' funded impulse drying work will concentrate aspects which will expand the usefulness of impulse drying technology to grades outside the scope of the joint venture agreement.

Work planned for FY'94-95 will focus on these major objectives.

Complete the numerical model of a proposed controlled-crown impulse drying press roll to explore design parameters that optimize energy utilization and to predict stress and temperature within the impulse drying press roll during typical operation.

Construct and use the high speed test stand to document the long term durability of impulse drying press roll coatings.

Complete student work to determine the interdependency of the "thermal mass" of the heated press roll surface and press impulse on impulse drying performance.

Complete student work to measure heat and mass transfer to a sheet during steam box operation.

Complete student work to investigate ways of opening the operating window of impulse drying.

REFERENCES

1) Orloff, D. I., and Phelan, P.M., "A Comparison of Impulse Drying To Double-Felted Pressing On A Pilot-Scale Shoe Press, " IPST Member Report 7, (December 1993).

2) Orloff, D.I., "Impulse Drying Of Recycled Multi-Ply Linerboard: Laboratory-Scale Studies," *Tappi Journal*. 77(2):169 (1994).

3) NIH *Image* 1.49 is a public domain image processing and analysis program for the Macintosh it may be obtained NTIS (National Technical Information Service), 5285 Port Royal Road, Springfield, VA 22161, phone 703-487-4650, order number PB90-500687 ($100 check, VISA, or Mastercard).

4) Bloom, F., Hojjatie, B., and Orloff, D.I., "Modeling Of Fluid Flow And Heat Transfer In A Crown Compensated Impulse Drying Press Roll, I: The Lubrication Problem," IPST Member Report 8, (December 1993).